ON NON-UNIFORM PUMPING EFFECTS IN SEMICONDUCTOR LASERS

By

JAMES SWOGER, B. ENG., M. ENG.

A Thesis

Submitted to the School of Graduate Studies

in Partial Fulfilment of the Requirements

for the Degree

Doctor of Philosophy

McMaster University

© Copyright by James Swoger, January 1997

ON NON-UNIFORM PUMPING EFFECTS IN SEMICONDUCTOR LASERS

DOCTOR OF PHILOSOPHY (1997)

McMaster University

(Engineering Physics)

Hamilton, Ontario

TITLE: On Non-uniform Pumping Effects in Semiconductor Lasers

AUTHOR: James Swoger, B. Eng., M. Eng. (McMaster University)

SUPERVISORS: Dr. J.G. Simmons and Dr. D.A. Thompson

NUMBER OF PAGES: ix, 178

ABSTRACT

We present a study of non-uniform pumping effects in semiconductor lasers. The first portion of this work is a theoretical undertaking, in which a physical model of a split-electrode, ridge-waveguide, InGaAsP/InP laser is developed. This model is based on the time-dependent solution of the carrier and photon rate equations, and is capable of describing such device features as multiple electrical contacts, illumination of the facets via an external light source, multiple optical cavity modes, and continuous variations in the carrier and photon concentrations. The simulations generated from this model demonstrate: 1) output power vs. bias characteristics that include threshold control, discontinuities, and bistability, 2) wavelength tuning via gain peak shifts and varying refractive index, 3) self-sustained pulsations caused by repetitive Q-switching, 4) external injection effects such as injection locking, all-optical switching, and optical self-pulsation control, and 5) current modulation characteristics. The effects of varying the device bias and geometric parameters on these phenomena are presented.

The second part of the thesis consists of an experimental investigation of a series of multi-quantum well InGaAsP/InP split-contact lasers. By varying the bias currents and contact lengths, we have studied their effects on the output power and spectra of these devices. The experimental results we present are in good agreement with the simulations based on our theoretical model.

ACKNOWLEDGMENTS

There are a number of persons whose assistance and encouragement I would like to acknowledge at this point, as this thesis could never have reached completion without their efforts. First of all I would like to thank my supervisors, Drs. John Simmons and Dave Thompson, for their continued intellectual and financial support over the course of my Ph.D. studies. Without their wisdom and guidance I certainly would have gone (even further) astray years ago.

I have also received invaluable help from other members of the Engineering Physics department the course of my years as a graduate student. My extended sojourn at McMaster has allowed me to interact with hundreds of staff and students here, all of whom have influenced my career in one way or another. In particular, I would like to thank Drs. Steve Kovacic and Jugnu Ojha, who helped guide me during the early portion of my work here, John Hazel and Greg Letal, with whom I have had many helpful discussions in more recent years, and, of course, Eugene Tan, who has been an invaluable colleague for my entire time at McMaster.

In addition to these people at the university, I would also like to extend my gratitude to Nortel Technologies, and in particular to Dr. Jack Evans, for supplying the majority of the devices investigated over the course of my studies. The financial support of both the NSERC and OGS programs has also been essential to the completion of this thesis.

Finally, I must thank my family and friends for their continued moral support over the years. Their constant encouragement has turned what could have been a purgatorial undertaking into a thoroughly enjoyable experience. Thank you all.

Jim Swoger
Nov. 3, 1996

TABLE OF CONTENTS

ABSTRACT iii

ACKNOWLEDGMENTS iv

TABLE OF CONTENTS v

LIST OF FIGURES AND TABLES viii

CHAPTER 1: INTRODUCTION 1

1.1: GENERAL INTRODUCTION 1
1.1.1: Preamble *1*
1.1.2: Historical Context *1*
1.1.3: Semiconductor Laser Outline *4*
1.2: SEMICONDUCTOR LASERS AND SATURABLE ABSORPTION 5
1.2.1: Semiconductor Laser Principles *5*
1.2.2: Spontaneous & Stimulated Emission and Absorption *7*
1.2.3: Device Structure and the Resulting Saturable Absorption *9*
1.3: NON-UNIFORM PUMPING: ADVANTAGES AND APPLICATIONS 15
1.3.1: The Extra Degree of Biasing Freedom *16*
1.3.2: Absorber Effects *19*
1.3.3: Optical Pumping *20*
1.4: THESIS MOTIVATION AND OUTLINE 21
1.4.1: Previous Modelling Work *21*
1.4.2: Thesis Goals *23*
1.4.3: Outline of Thesis *24*

CHAPTER 2: LASER THEORY 30

2.1: INTRODUCTION 30
2.2: CARRIER RATE EQUATION 35
2.3: THE CARRIER RECOMBINATION RATE 36
2.3.1: The Non-Stimulated Carrier Recombination Rate, R_r *36*
2.3.2: The Spontaneous Recombination Rate, R_{sp} *37*
2.3.3: The Equilibrium Absorption Coefficient, α_o *40*
2.3.4: Summary of Radiative Recombination *41*
2.4: THE OPTICAL GAIN COEFFICIENT 44
2.4.1: An Expression for the Optical Gain, G_m *44*
2.4.2: The Fermi Level as a Function of Carrier Concentration, $E_{Fc/v}$ *45*
2.4.3: Summary of the Optical Gain *46*
2.5: PHOTON RATE EQUATIONS 49
2.5.1: Introduction *49*
2.5.2: Time Invariant Photon Equations *50*
2.5.3: Time Variant Photon Equations *53*

2.5.4: The Spontaneous Emission Term, Q_m *56*

CHAPTER 3: LASER SIMULATIONS **61**

3.1: INTRODUCTION 61
3.2: THE NUMERICAL METHOD 61
3.2.1: The Solution Algorithm *61*
3.2.2: Some Computational Considerations *63*
3.3: A UNIFORMLY PUMPED LASER SIMULATION 66
3.3.1: Motivation *66*
3.3.2: The Time-Dependent Simulation *66*
3.3.3: The Steady-state Characteristics *70*
3.3.4: The Spectral Characteristics *71*
3.3.5: The Effects of the Longitudinal Carrier Distribution *74*
3.4: NON-UNIFORM ELECTRICAL PUMPING: DC SIMULATIONS 77
3.4.1: The Device Parameters *77*
3.4.2: Varying Bias for a Fixed Geometry *77*
3.4.3: Different Contact Geometries *88*
3.4.4: High Reflectivity Facets *92*
3.5: SELF-SUSTAINED PULSATIONS 94
3.5.1: Detailed Self-Pulsing Examples *94*
3.5.2: General Pulse Characterization *99*
3.6: MODULATED CURRENT SIMULATIONS 104
3.6.1: Detailed Modulation Examples *104*
3.6.2: General Modulation Characterizations *106*
3.7: NON-UNIFORM OPTICALLY PUMPED LASER SIMULATIONS 109
3.7.1: Introduction *109*
3.7.2: Operation in the Unistable Regime *110*
3.7.3: Operation in the Bistable Regime *114*
3.7.4: Operation in the Self-Pulsing Regime *119*
3.8: TUNING DUE TO REFRACTIVE INDEX CHANGES 121

CHAPTER 4: EXPERIMENTAL RESULTS **129**

4.1: INTRODUCTION 129
4.2: DEVICE GROWTH & FABRICATION 130
4.3: EXPERIMENTAL APPARATUS AND TECHNICAL CONSIDERATIONS 134
4.3.1: Optical Power Measurements *134*
4.3.2: Spectral Measurements *136*
4.3.3: Comparing Experimental and Simulated Results *137*
4.4: EXAMPLES OF OPTICAL POWER VS. BIAS CURRENT 138
4.4.1: L-I Curves Demonstrating Typical Device Operation *139*
4.4.2: L-I Curves Demonstrating Superluminescence *141*
4.4.3: L-I Curves Demonstrating Bistability *143*
4.5: OUTPUT POWER DEPENDENCIES 145
4.5.1: L-I_F-I_B Contours *145*
4.5.2: Device Geometry Effects, Varying L_T *147*
4.5.3: Device Geometry Effects, Varying L_F *150*
4.6: RESULTS OF SPECTRAL MEASUREMENTS 151
4.6.1: Examples of Superluminescent Spectra *152*
4.6.2: Examples of Lasing Spectra *153*
4.6.3: A Split-Contact Laser Spectral Map *157*

CHAPTER 5: CONCLUSIONS 161

5.1: INTRODUCTION..161
5.2: SUMMARY OF ACHIEVEMENTS AND RESULTS..161
5.2.1: Theoretical Accomplishments..*161*
5.2.2: Experimental Accomplishments..*163*
5.3: SUGGESTIONS FOR FUTURE WORK..164
5.3.1: Possible Theoretical Improvements..*164*
5.3.2: Possible Experimental Improvements..*165*

APPENDIX A: APPROXIMATION FOR THE FERMI FUNCTION 168

APPENDIX B: CALCULATING THE REFRACTIVE INDEX..171

B.1: THE KRAMER-KRONIG RELATION..171
B.2: THE NUMERICAL SOLUTION 172

APPENDIX C: SIMULATED LASER STRUCTURES 174

APPENDIX D: GLOSSARY..175

LIST OF FIGURES AND TABLES

FIGURE 1.1.1: SEMICONDUCTOR LASER STRUCTURE....4
FIGURE 1.2.1: LASER ENERGY BAND DIAGRAM....6
FIGURE 1.2.2: *E-k* DIAGRAMS UNDER LOW AND HIGH BIAS....8
FIGURE 1.2.3: SPLIT-CONTACT RIDGE-WAVEGUIDE LASER SCHEMATIC....10
FIGURE 1.2.4: POSSIBLE RELATIONSHIPS BETWEEN ABSORBER SATURATION AND THRESHOLD....13
FIGURE 2.1.1: SCHEMATIC OF THE NON-UNIFORMLY PUMPED LASER....32
FIGURE 2.3.1: RADIATIVE RECOMBINATION RATE VS. WAVELENGTH....42
FIGURE 2.3.2: RADIATIVE RECOMBINATION RATE VS. CARRIER CONCENTRATION....44
FIGURE 2.4.1: OPTICAL GAIN VS. WAVELENGTH....47
FIGURE 2.4.2: OPTICAL GAIN VS. CARRIER CONCENTRATION....48
FIGURE 2.5.1: SURFACE AREAS FOR THE COUPLING FACTOR, β_m....58
FIGURE 3.2.1: LASER MODE STRUCTURE....65
TABLE 3.3.1: GEOMETRIC TERMS FOR THE DEVICE SIMULATION....66
FIGURE 3.3.1: CURRENT AND OPTICAL OUTPUT VS. TIME....67
FIGURE 3.3.2: OPTICAL RESPONSE TO A CHANGE IN BIAS CURRENT....69
FIGURE 3.3.3: STEADY-STATE UNIFORMLY BIASED LASER CHARACTERISTICS....71
FIGURE 3.3.4: STEADY-STATE UNIFORMLY BIASED LASER SPECTRA....72
FIGURE 3.3.5: CARRIER CONCENTRATION VS. POSITION IN THE LASER CAVITY....75
FIGURE 3.3.6: SPECTRA USING VARYING AND CONSTANT CARRIER PROFILES....76
FIGURE 3.4.1: *L-I* SIMULATIONS WITH I_2 FIXED....78
FIGURE 3.4.2: SPECTRAL SIMULATIONS WITH I_2 FIXED....80
FIGURE 3.4.3: CARRIER PROFILES AT AND ABOVE THRESHOLD....82
FIGURE 3.4.4: *L-I* CURVES WITH EITHER CONTACT OPEN CIRCUITED....84
FIGURE 3.4.5: CARRIER PROFILES IN THE HYSTERESIS LOOP....85
FIGURE 3.4.6: OPTICAL OUTPUT POWER CONTOURS....87
FIGURE 3.4.7: *L-I* OF TWO-CONTACT LASERS WITH THE SAME TOTAL LENGTH....89
FIGURE 3.4.8: *L-I* CHARACTERISTICS OF A 1000 μm SPLIT-CONTACT LASER....91
FIGURE 3.4.9: *L-I* CURVES WITH DIFFERENT FACET REFLECTIVITIES....93
FIGURE 3.5.1: SIMULATED SELF-SUSTAINING PULSE TRAINS....95

FIGURE 3.5.2: SIMULATED CARRIER DENSITY PROFILES DURING SELF-PULSATIONS........................... 98
FIGURE 3.5.3: SELF-PULSATION FREQUENCY VS. BIAS CURRENT..100
FIGURE 3.5.4: EXTREMA OF THE OUTPUT POWER DURING SELF-PULSATIONS.................................102
FIGURE 3.6.1: TEMPORAL RESPONSE TO BIAS CURRENT MODULATION...105
FIGURE 3.6.2: SIMULATED MODULATION EFFICIENCY VS. FREQUENCY 107
FIGURE 3.7.1: TEMPORAL RESPONSE TO AN INCIDENT OPTICAL PULSE 111
FIGURE 3.7.2: LASER SPECTRA, VARYING INCIDENT OPTICAL POWER...112
FIGURE 3.7.3: LASER SPECTRA, VARYING INCIDENT OPTICAL MODE..113
FIGURE 3.7.4: L-I SHOWING BISTABLE REGION...115
FIGURE 3.7.5: ALL-OPTICAL SWITCHING IN THE HYSTERESIS LOOP 116
FIGURE 3.7.6: LASER OUTPUT VS. INCIDENT PULSE POWER 117
FIGURE 3.7.7: L-I SHOWING SELF-PULSING REGION 120
FIGURE 3.7.8: OPTICAL PUMPING WITH SELF-PULSATIONS 121
FIGURE 3.8.1: THE COMPLEX INDEX OF REFRACTION...123
FIGURE 3.8.2: CARRIER DENSITY & WAVELENGTH VARIATIONS VS. OUTPUT POWER.........................125
TABLE 4.2.1: NOMINAL LASER WAFER STRUCTURE 131
FIGURE 4.2.1: SCHEMATIC OF THE MOUNTED LASER STRUCTURE...132
TABLE 4.2.2: LASER CONTACT LENGTHS...133
FIGURE 4.3.1: SCHEMATIC OF L-I MEASUREMENT APPARATUS..135
FIGURE 4.3.2: SCHEMATIC OF SPECTRAL MEASUREMENT APPARATUS 136
FIGURE 4.4.1: L-I CURVES, ILLUSTRATING VARYING THRESHOLD & DISCONTINUITY.........................139
FIGURE 4.4.2: L-I CURVES, ILLUSTRATING SUPERLUMINESCENT BEHAVIOUR..................................142
FIGURE 4.4.3: L-I CURVES ILLUSTRATING OPTICAL BISTABILITY...143
FIGURE 4.5.1: CONTOUR PLOT OF THE OUTPUT POWER IN THE I_F-I_B PLANE.....................................146
FIGURE 4.5.2: THRESHOLD CONTOUR PLOTS, VARYING L_T..149
FIGURE 4.5.3: THRESHOLD CONTOUR PLOTS, VARYING L_F..151
FIGURE 4.6.1: SPECTRA IN THE SUPERLUMINESCENT REGIME..152
FIGURE 4.6.2: TUNING OF AN INDIVIDUAL CAVITY MODE...154
FIGURE 4.6.3: LASER SPECTRA AT INCREASING VALUES OF I_F 155
FIGURE 4.6.4: PEAK WAVELENGTH MAP IN THE BIAS CURRENT PLANE 158
FIGURE A.1: FERMI LEVEL VS. CARRIER CONCENTRATION..170

CHAPTER 1: INTRODUCTION

Πάντες ἄνθρωποι τοῦ εἰδέναι ὀρέγονται φύσει.

Aristotle, *Metaphysics* I.i.1[1]

1.1: General Introduction

1.1.1: Preamble

The words with which Aristotle began his treatise on the nature of reality over twenty-two centuries ago still express one of the fundamental truths of mankind: the desire for knowledge is a basic driving force behind human culture. This search for enlightenment is the central impetus behind any philosophical undertaking, whether it comes under the heading of Abstract Philosophy, or the more "practical" Arts, Sciences, or Engineering fields. Although a few gifted individuals such as Aristotle, DaVinci and Newton have been able to make valuable contributions to many or all of these areas of knowledge, the majority of people find it more productive to limit themselves to a more specific realm of expertise. For example, a person attempting to complete a Doctor of Philosophy degree in an Engineering Physics department might well find themselves working almost exclusively in the field of solid-state lasers, investigating and utilizing the interactions between electromagnetic energy and semiconductor crystals.

1.1.2: Historical Context

The interplay between light and matter has been a subject of scientific investigation for millennia, probably beginning with the simple question "What is the nature of sight?" Aristotle himself claimed that "light is the colour of the transparent":[2] an interesting

concept, perhaps, but somewhat ambiguous from a modern physicist's point of view. Since that time understanding has progressed, and this rather antiquated approach to the problem has given way to a more systematic method. Early pioneers in the scientific research of optics include Claudius Ptolemy (who, in the second century A.D., investigated the refraction of light at the interface between air and water),[3] Alhazen (active around the end of the first millennium, his work included estimating the height of the atmosphere from scattering measurements, formulating Alhazen's law of reflection,[a] and research into human vision),[4] and others. By the time of Newton's death in 1726, optics had progressed from a collection of empirical observations to a logical, if not entirely accurate, scientific theory. While it was able to describe phenomena such as dispersion, refraction, and reflection quite well, there was still considerable uncertainty as to exactly how light interacted with matter on a microscopic scale. Although the weight of Newton's established opinions may have hampered further modifications to optical theory to some extent, it continued to develop as the observations of such men as Thomas Young and Augustin Jean Fresnel were found to be incompatible with a simple, corpuscular model of light. Then, in the third quarter of the nineteenth century, James Clerk Maxwell synthesized the work of the previous decades into a series of equations that describe light in terms of electromagnetic waves, a model that is still used today to describe may aspects of radiation.

While the development of modern optics has been a relatively long process spanning a series of centuries, most of the progress in our understanding of the structure of matter has occurred in the last hundred years. It was not possible to generate an accurate model of the interaction of light and matter on a microscopic scale before it was determined that atoms are not indivisible structures, but consist of a small, positive nucleus surrounded

---

[a] This law states that the incident and reflected beams both lie in the same plane as a line drawn normal to the reflecting plane.

by a "cloud" of electrons. This was not definitively established until Ernest Rutherford's work in 1911. Even so, the development of quantum mechanics in the 1910's and 20's was necessary before a theoretical framework capable of describing the detailed interaction of light and matter on an atomic or molecular level was achieved. Although work has, of course, progressed during the intervening years, it is essentially a combination of quantum mechanics and electromagnetic theory that we use today to describe the physics of the interactions of light and matter in many situations.

Although mankind has been aware of the phenomena of optical absorption and emission from matter throughout history, it was Albert Einstein who formulated expressions describing the mechanisms by which these effects occur.[a] The concepts of spontaneous emission and absorption had been in use for some time, but it was Einstein who proposed another possible radiative transition: stimulated emission. Although many light sources, such as incandescent and fluorescent light bulbs and light-emitting diodes function due to spontaneous emission alone, stimulated emission is necessary for a material to amplify electromagnetic energy.

It was the combination of work done in all of the areas of physics that we have referred to here that allowed scientists in the 1950's to create the *maser*, a device for ***m**icrowave **a**mplification by the **s**timulated **e**mission of **r**adiation*. Shortly thereafter, in 1960, the same principles were applied by Theodore H. Maiman to produce the first optical version of this device, the laser.[5] Since that first success, for which the amplification medium was a synthetic ruby crystal, lasers have been made from a variety of materials, from combinations of noble gases to liquid organic dyes to doped semiconductor crystals.

---

[a] The expressions describe the rate of radiative transitions between two electronic states, and are governed by Einstein's A and B coefficients.

The combination of the small size, versatility, reliability, and relatively low cost has made the later group an important component in our modern telecommunications industry.

1.1.3: Semiconductor Laser Outline

In semiconductor lasers, the energy needed to produce light is generally supplied by electrical pumping: a bias current injects electrons and holes into p-n junction,[6] where the radiative recombination of these carriers can result in both spontaneous and stimulated emission. A rough sketch of the laser structure is shown in Fig. 1.1.1: we see that current is injected vertically into the active region of the laser (the p-n junction) through the metal contacts. The light generated in the laser is emitted through the cleaved facets at the ends of the laser; these facets are partially reflecting, so that a portion of the light is coupled out to the external environment, and part is reflected back into the laser where it can undergo further amplification.

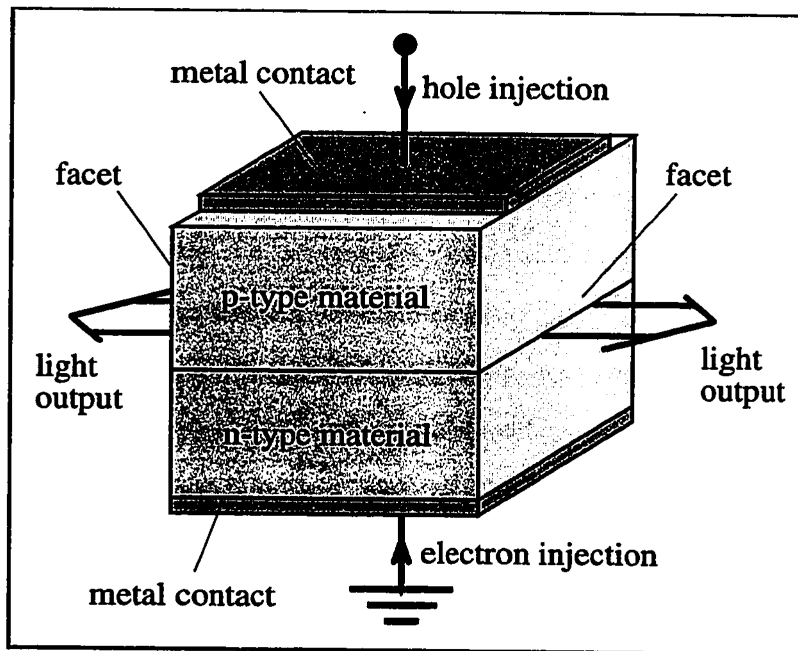

Figure 1.1.1: Semiconductor Laser Structure
A sketch of the basic regions of a semiconductor laser is shown.

As shown in Fig. 1.1.1, it is common in semiconductor lasers for the electrical contacts to extend continuously from one facet of the device to the other. This allows the carriers to be

injected uniformly into the active region. Lasers that are pumped uniformly in this manner have been studied thoroughly over the past few decades, and although our understanding of them is not perfect, it can be considered mature. It is, however, possible to reconfigure the metallization of the laser contacts so that it does not cover the length of the laser evenly. This type of non-uniform pumping of the laser has distinct advantages for some applications, as will be discussed in Section 1.3, but the amount of research that has been done in this area is relatively small. It is for this reason that we have chosen to investigate the non-uniform pumping of semiconductor lasers in this work.*

1.2: SEMICONDUCTOR LASERS AND SATURABLE ABSORPTION

1.2.1: Semiconductor Laser Principles

Before we commence with an account of the effects and applications of these devices, it would seem instructive to give a brief description of the physics of semiconductor lasers, and how non-uniform excitation differs from more traditional, continuous pumping. To give a very basic description of a semiconductor laser, one might say it is similar to a light-emitting diode (LED) with the addition of some optical feedback mechanism. In Fig. 1.1.1 we showed what is perhaps the simplest practical structure, in which the feedback is supplied by reflections from the cleaved facets. More complicated devices such as distributed Bragg reflectors (DBR) or distributed feedback (DFB) are sometimes used when the criteria on the output spectra are stringent, but in any case the principle is to allow some of the light to exit the laser into the external environment while feeding a portion back into the active region for further amplification.

---

* It is possible to pump other types of lasers non-uniformly, and much of the theory developed here could be applied to them also, but in this thesis we limit ourselves to semiconductor devices.

Figure 1.2.1 depicts the electron energy diagram for a simple semiconductor laser, showing the basic process that occur during laser operation. The essential structure is a p-n semiconductor diode, where electrons are injected into the n-region and holes into the p-material through the metal contacts. These carriers traverse the bulk sections of the device until they either recombine (a processes which is minimized in a good laser) or reach the active region. Because of the large concentration of both electrons and holes in this part of the device a large recombination current occurs in the active region, leaving only a small amount of leakage current to escape in the form of minority carrier flow. The radiative component of this active region recombination current contributes both to spontaneous

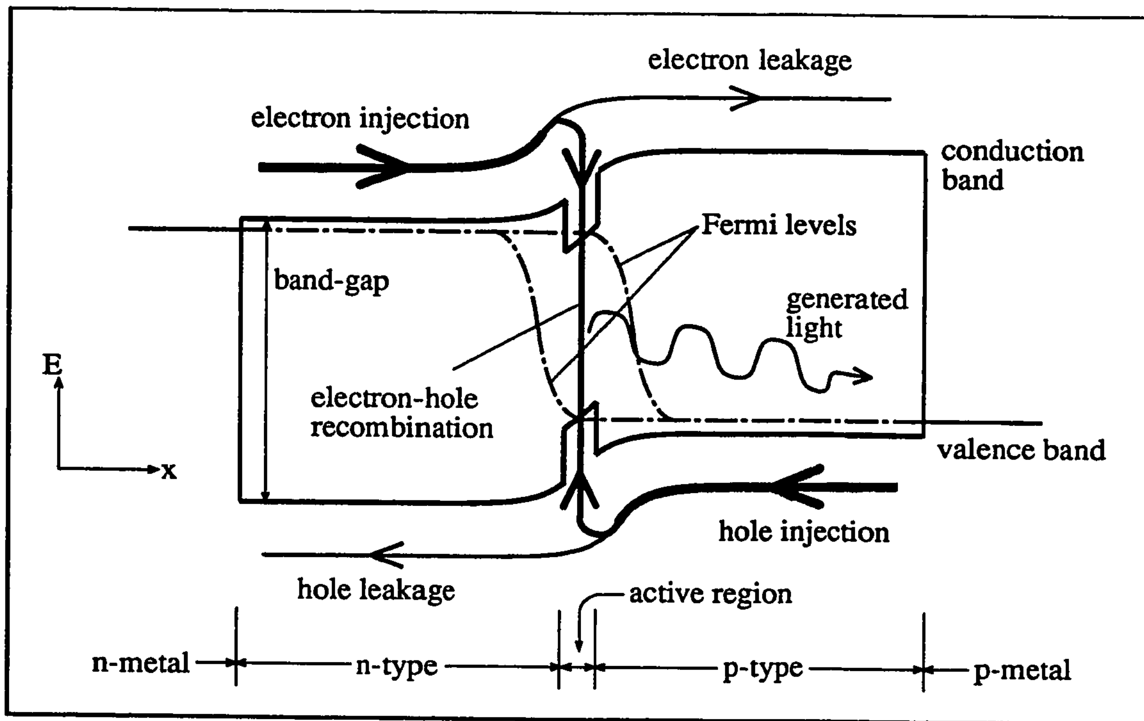

Figure 1.2.1: Laser Energy Band Diagram
A simplified sketch of the electron energy bands as a function of position is shown for a p-n junction semiconductor laser. The electron and hole currents are indicated by large arrows, and the dash-dotted lines represent the Fermi levels.

emission and, at biases above transparency, the optical gain of the laser.

In Fig. 1.2.1 we have depicted the active region as having a slightly narrower band-gap than the rest of the device. This is generally the case for modern laser designs, for three reasons. First, it serves to confine the carriers that are injected into the active region from leaking out, which increases the carrier density in this region and, consequently, enhances the radiative recombination rate. Since the refractive index of the semiconductor decreases as the separation of the conduction and valence bands increases, the second advantage of a narrow band-gap active region is that it acts as a waveguide to confine the optical energy in the region where the carrier density is the greatest. The third reason for including a different band-gap in the active region is because it allows us to customize the laser spectrum: the lasing wavelength is closely correlated with the band-gap energy.

Although we have shown the variations in the bands as simple, abrupt discontinuities in Fig. 1.2.1, this is not necessarily the case. Lasers are often designed with graded band-gaps, possibly including low-dimensional structures such as quantum wells or wires as well.[7] In general these variations are combined to optimize the laser band profile in terms of one or more of the advantages listed above.

1.2.2: Spontaneous & Stimulated Emission and Absorption

At low levels of current injection a typical semiconductor laser behaves in a manner similar to an LED. The bias current supplies carriers that can recombine radiatively in the active region (the spontaneous emission rate varies approximately as the product np, where n and p are the concentrations of electrons in the conduction band and holes in the valence band, respectively). However, for low carrier densities the active region material is absorbing, so that the amount of light coupled out to the external environment is small.

The E-k band diagram for this situation is depicted in Fig. 1.2.2a, for which the Fermi levels lie inside the semiconductor band-gap. These Fermi levels represent the energies at which 50% of the available states are occupied: there are very few electrons more than a few tens of meV above E_{Fc}, and few unoccupied states below E_{Fv}. Consequently there are not many free carriers available to participate in radiative, band-to-band recombination. Also, since the absorption varies with the product of the number of holes in the conduction band and electrons in the valence band, light that is generated is generally absorbed within a short distance of its point of origin.

As the laser bias current is increased the carrier density in the active region rises, and eventually the situation shown in Fig. 1.2.2b is reached. The rate of carrier injection

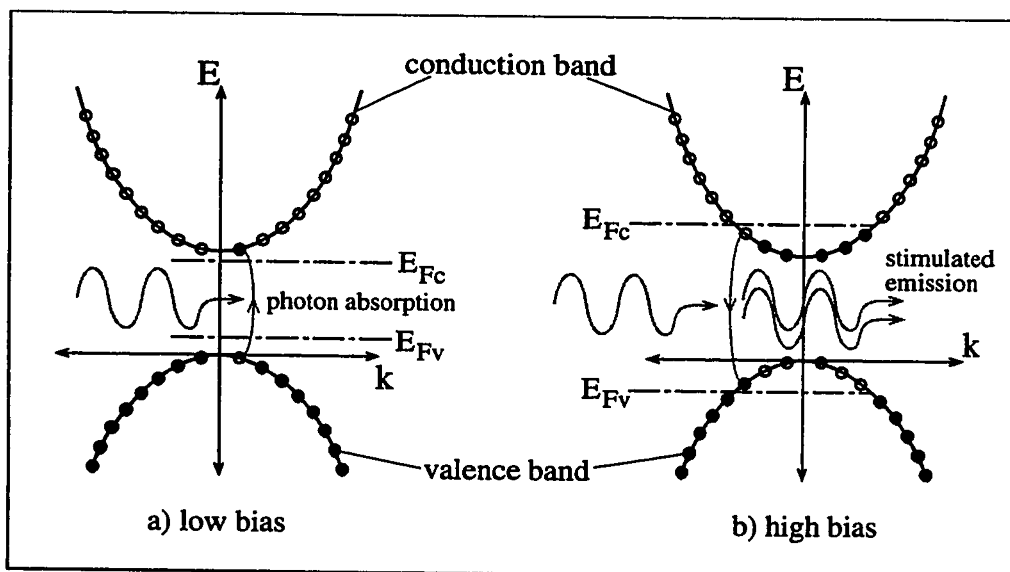

Figure 1.2.2: *E-k* Diagrams Under Low and High Bias

The energy (E) vs. wavenumber (k) diagrams for electrons in the semiconductor active region is shown, under a) low and b) high biases. Occupied states (electrons) are represented by filled circles, and unoccupied states (holes) by open circles. The conduction band Fermi energy is denoted by E_{Fc}, that for the valence band by E_{Fv}.

is now sufficient to shift the Fermi levels into their respective bands, so that the bottom of the conduction band is filled with electrons and the top of the valence band with holes. This type of carrier distribution is known as population inversion, and results in both an increase in the spontaneous and stimulated emission rates (both n and p are large) and a decrease in the absorption (there are few empty states in the conduction band to which electrons can be promoted). In fact, at sufficiently large carrier densities the absorption coefficient of the material becomes negative, and light passing through the active region experiences gain instead of loss.

This gain, which is due to stimulated emission of photons by the inverted carrier population, makes it possible for lasing to occur in the device. The photon flux generated by spontaneous emission is amplified as it travels through the material, and exits the surface of the device with increased power. Although amplification of the spontaneous emission occurs irrespective of the direction in which the light travels, for most orientations the photons exit the active region before experiencing a large amount of gain. Light which travels along the long axis of the device, however, is partially reflected at each facet of the laser so that it traverses the amplifying region many times. Both optical feedback and (positive) gain are necessary conditions for lasing to occur in the device.

1.2.3: Device Structure and the Resulting Saturable Absorption

We have now given a brief outline of the functioning of a semiconductor laser, and mechanisms coupling the carrier and photon concentrations in the cavity. In this section we proceed to describe the specific structure of the split-contact laser, and how it can lead to saturable absorption. A three-dimensional schematic of a ridge-waveguide, split-electrode semiconductor laser is shown in Fig. 1.2.3. In this type of laser optical and carrier confinement in the lateral direction are provided by the ridge structure. Other laser formats,

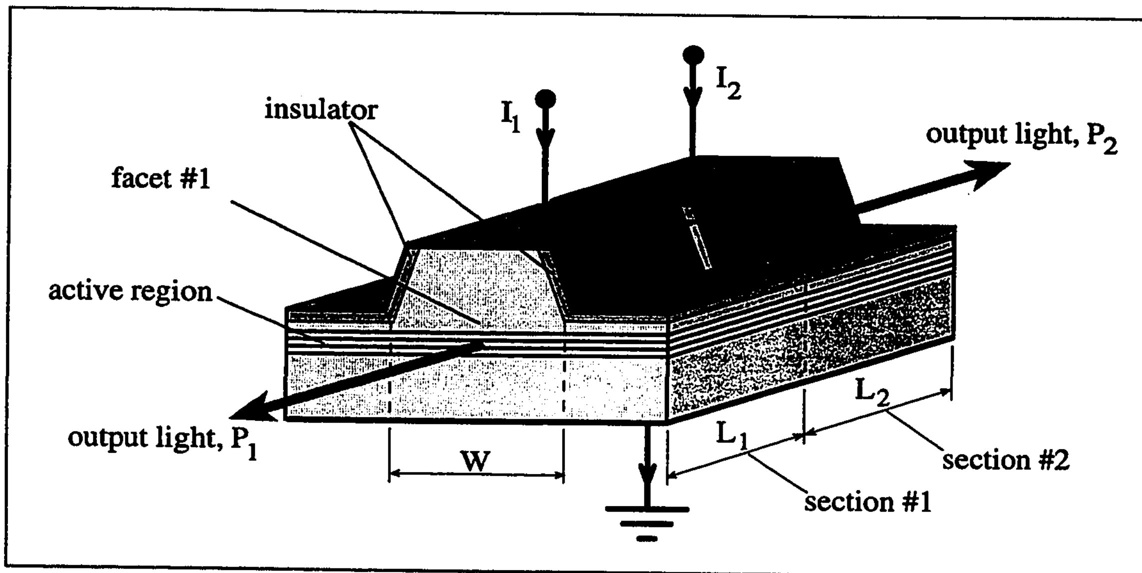

Figure 1.2.3: Split-Contact Ridge-Waveguide Laser Schematic
The basic structure of a split-contact ridge-waveguide semiconductor laser is shown.

such as broad-area and buried-heterostructure lasers, are also employed for some applications, but the same general principles apply to all of these structure. For simplicity we restrict ourselves a discussion of ridge-waveguide devices for the remainder of this work, as this is the preferred structure for our applications.

For practical reasons the bottom layer of the laser is usually n-type, with a nominally undoped active region covered by a p-type top section. The bottom metallization is continuous over the back surface, providing a common electrical ground for the entire device. The top metal is separated from the semiconductor by a thin insulating layer (typically SiN or SiO_2) everywhere except on the top of the ridge. This confines the carrier injection laterally, so that the majority of the carriers are injected into the portion of the active region under the ridge. In addition, the top contact is also discontinuous along the optical axis, separating the laser into two sections which can be independently biased by the currents I_1 and I_2. The trench that separates these two sections does not reach the active

region of the device (to avoid disrupting the optical field in the cavity), but is etched into the upper layer of the semiconductor to a level sufficient to electrically separate the sections.

If we first consider the situation where the two top contacts in Fig. 1.2.3 are electrically shorted together, we have the situation of uniform pumping. In this case the carrier injection into the active region is constant along the length of the device length, with a current density of $J = \dfrac{I_1 + I_2}{W(L_1 + L_2)}$. As we would expect, this leads to an approximately uniform carrier concentration in the active region of the laser,[a] and hence the parameters such as the spontaneous emission rate and the absorption/gain are roughly constant along the device length. Uniformly biased lasers, therefore, generally produce a continuous, stable optical output as a function of bias current. For low bias levels the output power is low, and the photons are produced primarily by spontaneous emission. At some threshold current the gain becomes approximately equal to the optical losses in the cavity (due to emission through the facets, scattering, etc.), and the device begins to lase. Above this threshold stimulated emission is the dominant photon generation mechanism, and the light output increases approximately linearly with the current drive.

The situation can be substantially different in a split-electrode configuration where the bias currents are controlled independently. Consider the case where we set the current I_2 in Fig. 1.2.3 to zero, and apply a small positive bias I_1 to the other section. Some of the carriers injected into the active region of section #1 recombine radiatively, so that the light output P_1 begins to rise. Since there is no carrier injection into section #2, the absorption in this region is strong, and very little of the light from section #1 will reach facet #2.

---

[a] Our simulations in Section 3.3 indicate that above threshold there are small longitudinal variations in the carrier density due to its coupling with the large photon concentration. These deviations are small, however, when compared to non-uniform current injection simulations.

However, this photon absorption does generate electron-hole pairs which supplement the carrier concentration in section #2, so that effectively this region is optically pumped by the light from section #1.

Now as the bias I_1 is increased the photon generation rate in section #1 also rises, so that more and more carriers are produced in section #2 by photon absorption. This causes a decrease in the absorption coefficient (the number of photons absorbed per unit length) in section #2, allowing a greater fraction of the incident light to pass through the region. This process continues as P_1 rises until eventually region #2 approaches a condition of transparency. Further increases in I_1 do not result in an increase in the amount of light absorbed under contact #2, and we say that the absorption has saturated. Once this happens it is possible for the device to begin lasing: some fixed amount of the light entering section #2 is lost to maintain the absorption saturation, but the remainder can reach the back facet and be reflected back into the amplifying portion of the laser. The device thus achieves the gain and optical feedback conditions necessary for lasing.

Although absorption saturation must occur before threshold can be reached, there are several possible scenarios that describe the relationship between these two phenomena. In the first, the optical losses associated with the saturation of the absorbing region are small compared to the other loss mechanisms in the device. This is most likely to be the case when the absorbing section is short, so that the volume of material that must be saturated is small, or when the absorber is slightly forward biased.* In these cases the absorber saturates at a bias significantly below the lasing threshold, and the more dramatic

---

* In this discussion, we assume that the current supplied to the absorbing section is held at a constant, relatively low level, while the current to the other section (the gain region) is varied.

effects that can occur when absorption saturation accompanies threshold are not observed. A typical *L-I* curve illustrating this situation is sketched in Fig. 1.2.4a.

The second case of note takes place when the decrease in loss accompanying the saturation of the absorber drives the laser above the threshold condition. Since the amount of light a laser produces when lasing is generally quite large compared to the output below threshold, the saturation of the absorber can be accompanied by an abrupt rise in the laser's output power. This discontinuous mode of operation is encountered when the losses associated with the unsaturated absorber are quite high, so that when they are removed the laser suddenly switches to a condition substantially above threshold (see Fig. 1.2.4b).

When the split-contact laser is biased in a configuration that produces this type of discontinuity at threshold, the initial state of the device can also be important. With an absorber that saturates relatively easily (either because it is short or because a small positive bias is applied to it), threshold occurs at the same current regardless of whether the bias is

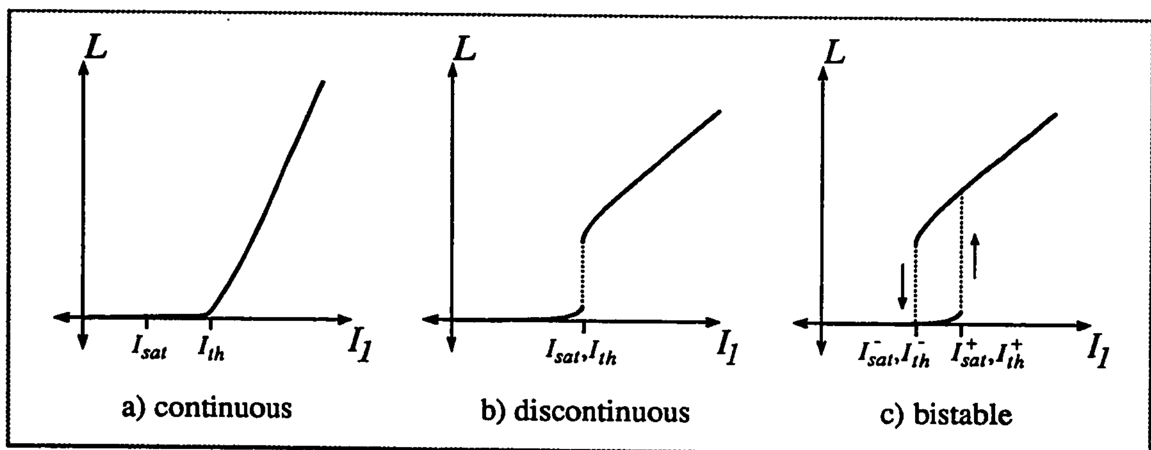

Figure 1.2.4: Possible Relationships Between Absorber Saturation and Threshold

Three light vs. current curves are sketched for a split-electrode laser, showing the cases where absorber saturation occurs below threshold (a) and at threshold (b and c). In all cases, the bias current I_1 is swept, while I_2 is held constant (see Fig. 1.2.3).

increased or decreased. The transition between the saturated and non-saturated absorption is independent of the previous device condition.

If the effect of the absorber is stronger the threshold may "split", becoming dependent on the direction of the current sweep. As the gain section bias is increased from a low value, at some current I_{th}^+ the absorption in the unbiased region saturates and lasing commences. Since in this case the unsaturated absorber losses are large, after saturation the device jumps to a low-loss state with high optical power. The photon concentration in the cavity can be sufficient to maintain the saturation of the absorbing section when the current is decreased below I_{th}^+: lasing continues until an abrupt shut-off at $I_{th}^- < I_{th}^+$. The result is a hysteresis in the optical output of the laser, in which there are two possible, steady-state output levels (one lasing and one non-lasing) for biases between I_{th}^- and I_{th}^+ (see Fig. 1.2.4c).

The final case of interest occurs when the carrier density in the gain section of the laser builds up to a high level before the absorber saturates. If the amount of light needed to saturate the absorbing section is large, a high carrier concentration in the gain section is needed to generate the required photon flux. When the absorber finally does saturate the net gain in the cavity is greater than the lasing condition requires, and the photon density rapidly builds up to a level much greater than can be sustained indefinitely. Since the gain is a result of stimulated recombination of electron-hole pairs, this large transient is accompanied by a drop in the number of carriers in the cavity. Under the right conditions an oscillating feedback is set up between the photon and carrier concentrations: an initially large carrier density is depopulated by an increasing photon flux, which must then drop as a result of the reduced gain. This low light level allows the saturated absorber to recover, so that the carrier density in the gain section begins to build up again until the whole

process is repeated. Although these self-sustained pulsations are induced by a d.c. electrical bias, they can reach frequencies into the gigahertz range.

In addition to this method, known as repetitive Q-switching, self-pulsations can also be generated in a non-uniformly pumped laser via the mechanism of mode-locking. When this occurs the electric fields in a number of different cavity modes add in a phasor manner to produce a series of optical pulses with a spacing equal to the round trip time of the laser cavity. For this mechanism to operate, the phases of the different modes must be locked together: this is commonly done by incorporating an absorbing section inside the cavity that can modulate the laser gain. The absorption of this section can be externally controlled to achieve a match with the round trip time of the cavity (active mode locking), or designed to operate as a saturable absorber (passive mode locking). In this case the initial portion of the optical pulse bleaches the absorber; once it has passed, the absorber recovers, so that the phase of the light is effectively locked to the front edge of the optical pulse.

1.3: Non-Uniform Pumping: Advantages and Applications

Thus far we have given a brief, qualitative description of the operation of a semiconductor laser, and the different types of behaviour we can expect when the device is fabricated with a split-electrode structure. In order to justify our expenditure of time and energy on studying this subject, our next task is to explain why these lasers are of interest. For a general overview of the function and applications of two-section lasers, see Kawaguchi:[8] we have provided more specific references for different aspects of the device behaviour in the remainder of this section.

1.3.1: The Extra Degree of Biasing Freedom

The first reason for investigating non-uniformly pumped semiconductor lasers is the extra degree of biasing freedom that is available when we implement a split-electrode structure in the device. In a more traditional laser configuration, where the top and bottom contacts are continuous along the length of the laser, we have only one bias current, I_{tot}, that can be varied. Selecting a bias to produce a given output power from the device also determines the spectral output, unless we chose to vary the device temperature or its material or geometric parameters. With a split-electrode device, we have two (or more, depending the number of sections into which the contact is divided) degrees of freedom when choosing the laser bias. Instead of a single current, I_{tot}, that results in the desired output power, there will generally be a set of currents (I_1, I_2) that produce the same power level. Since the output wavelength is also dependent on the bias currents, in principle we can select the bias point (I_1, I_2) that results in both the required power and wavelength.

This property of the split-electrode laser is of interest to those involved in tunable wavelength sources. There are numerous applications for which the spectral components of the laser output are of prime importance. For wavelength division multiplexing (WDM) of digital fibre optic signals, it is necessary to have a series of emitters with a tightly controlled wavelength spacing on the order of a few Angstroms.[9,10] In a variety of applications, such as mechanical strain-sensing systems employing integrated Bragg reflectors in optical fibres,[11] it is desirable to have as large a range of continuous wavelength tunability as possible. In general, any coherent detection system will require fine control over the output spectra of the laser.

A variety of reports in the literature indicate that split-contact lasers are potential candidates to fill the role of tunable wavelength sources, at least for some applications. Although Fabry-Perot lasers are generally limited in their tuning range by the spectral

properties of the cavity, the introduction of even relatively simple DFB structures[a] has been shown to allow a continuous wavelength tuning range of up to 7.2 nm.[12] Vertical cavity surface-emitting lasers (VCSELs), which are of interest for low-threshold, high spatial density applications, have been demonstrated with continuous tuning ranges of up to 18 Å by utilizing a third contact to control the DBR bias.[13] In general, greater wavelength tunability has been achieved by separating the gain (active region) and tuning (DBR) sections of the laser, and adding a small phase-control section. A wavelength variation of 8.5 nm has been observed with this type of structure,[14] and with the possibility of utilizing heating effects[15] a continuous range of 13 nm has been reported.[16]

One application related to the tunability of split-contact lasers occurs in the field of high-speed modulation. Currently, the simplest technique used to achieve optical modulation in the communications industry is to have a semiconductor laser source with a separate, external modulator. Although this configuration can provide faster modulation[17] with reduced chirp,[18] it necessitates the use of a greater number of discrete components and the accompanying reliability and packaging complexity. Direct current modulation of the laser source can reduce the system complexity, but when a uniformly pumped laser is used, the speed and chirp issues remain.

In terms of speed and efficiency, there are two advantages that split-contact lasers have over simpler structures. When parasitic reactances are a limiting factor, with a split-electrode laser the bias applied to a small section of the device can be modulated. This effectively reduces the capacitance of the circuit, allowing greater speeds to be reached. Under suitable bias conditions, the gain-lever effect can also be employed in a multi-electrode laser to enhance the modulation efficiency.[19]

---

[a] i.e. one without a $\lambda/4$ phase shift or a separate DBR region.

One of the principal benefits of employing a split-contact laser for modulation applications is the possibility of operating with reduced chirp. Because of the coupling of the index of refraction and the carrier concentration in the active region, any direct intensity modulation of the laser is accompanied by a corresponding wavelength (and, hence, frequency) modulation.[20] This can result in a degradation in system performance in fibre optic systems where a narrow, well-controlled linewidth is imperative. The use of a push-pull modulation scheme, in which two of the laser contacts are modulated 180° out of phase so that the total current is kept approximately constant, effectively reduces chirp because the variations in the mean carrier density are minimized. With the proper implementation this technique can reduce the laser linewidth by a factor of more than seven, to approximately the Fourier transform limit.[21]

An additional use for split-contact lasers that is a result of the extra degree of biasing freedom comes from the ability to tailor the light vs. bias current characteristic (*L-I*) of the device. As will be shown both through simulations (Chapter 3) and experimental measurements (Chapter 4), it is possible to adjust the position of the lasing threshold, the structure of the *L-I* characteristic above threshold, and the amount of subthreshold, superluminescent output. The first two of these capabilities are important in applications where fine control and/or linearity of the output power is required.[a] When operated in the superluminescent regime, the split-electrode laser acts as a high power,[b] incoherent light source that can be used in applications such as optical interferometry where the low coherence length can reduce the noise levels.[22]

---

[a] A specific application of this is in the fiber communications industry, where it is sometimes desirable to be able to gradually increment the laser output power from low levels without encountering a sharp increase when threshold is reached. Optimizing the split-contact laser for this use was the original motivation for the project that eventually led to this thesis.

[b] These devices generally do not generate light as efficiently as a laser, but are considerably brighter than a comparable LED.

1.3.2: Absorber Effects

The second effect of interest in split-contact semiconductor lasers results from the weakly biased, absorbing section of the laser. In Section 1.2.3 we described how the saturable absorber effect functions, and some of the implications for the device output. One commercially intriguing application of the saturable absorber is its use in the generation of optical bistablity (and, in some cases, tristability).[23] These devices are of interest for optical memory and switching operations, as they produce both strongly and weakly emitting states that can be switched either electrically[24-26] or optically.[27,28] As little as 5.5 μW of input power has been demonstrated capable of switching the laser on,[29] while 570 μW is able to turn the device off.[30]

Another phenomenon caused by the saturable absorber effect in split-contact lasers is the generation of self-sustained pulsations. These pulsations are the result of repetitive, self-sustained Q-switching, and can be generated at frequencies from a few hundreds of MHz to greater than 11 GHz.[31] The frequency can be tuned continuously over this range with pulse widths that are typically on the order of tens of picoseconds, by varying the bias current to the laser.[32] These devices have found uses in the compact disk industry because of their relatively low sensitivity to back-reflections,[a] and as tunable microwave oscillators.[33] When employed as optical clock regenerators in communications systems,[34-36] the oscillation frequency can be locked to incident optical signal powers as low as a few μW.[37]

Under some conditions, self-sustained pulsations can also be generated in a non-uniformly pumped laser by mode-locking. In this type of self-pulsation the power per pulse is generally not as great as with Q-switching, but narrow pulses with a high repetition

---

[a] This insensitivity is due to the relatively short coherence length of the output light, compared to self-pulsations generated by other techniques.

rate are possible. Since in this case the oscillation frequency is determined by the length of the optical cavity,[38] for semiconductor lasers with typical lengths of a few hundred microns this results in frequencies on the order of 100 GHz. Quantum well devices with pulse widths of a few hundreds of femtoseconds have been demonstrated.[39] Although the coherent origin of these self-pulsations makes mode locking behaviour quite sensitive to external reflections, they are of interest for their ability to operate at higher frequencies than can be achieved by the Q-switching technique. It should be noted that both of these mechanisms for self-sustained pulse generation can operate in the same device, and in some cases their operating bias ranges may overlap.[40]

1.3.3: Optical Pumping

The third area in which non-uniform pumping effects in semiconductor lasers can be important is where the device is optically pumped. We wish to consider here the cases where photons are injected into the cavity through the laser facets: the resulting carrier generation is longitudinally non-uniform. Optical injection of this sort can be applied to devices with continuous electrical contacts, so that non-uniformities in the pumping are purely a result of the optical input, or to split-contact lasers.

The first and most obvious application of optical injection is where the laser is used as an optical amplifier or modulator. A considerable amount of work has gone into the investigation of these devices,[41,42] which find applications in fibre optic signal regeneration. Additionally, the output of an unmodulated laser is sometimes used to injection lock a second, modulated laser, in order to reduce chirp.[43,44]

There is also some interest in optical injection effects with split-electrode geometries. When operated in the unistable regime, the devices have been demonstrated as tunable optical filters for such applications as wavelength division multiplexing.[45] Optically

bistable lasers are of interest in terms of their optical switching properties: the devices have high- and low-emitting states which can be optically switched to create optical memory elements or latches. Investigations have been carried out to optimize the contact lengths and biases,[46,47] and input powers and wavelengths[48] of such structures. Operation in the self-pulsing regime has been shown to be an effective means of optical clock extraction in optical transmission systems.[49]

1.4: Thesis Motivation and Outline

1.4.1: Previous Modelling Work

From the above it should be evident that non-uniformly pumped lasers are of interest from both academic and commercial standpoints. However, there is at least one area in which the study of these devices appears to be less than comprehensive: previous models of the devices have often tended to be lacking to some extent. Because of the complexity of the processes occurring in semiconductor lasers under non-uniform pumping conditions, many researchers have chosen to make various approximations in their models. This is not to say that they are ineffective at predicting specific aspects of the device behaviour, but the result is that models capable of describing the physics of these lasers over a broad range of conditions are few.

One approximation that previous theoreticians[50-63] have made when modelling split-contact lasers is to assume that the carrier concentration is piecewise constant. Although they allow the carrier density to vary from one section of the device to another, it is usually assumed to be uniform under each contact. The results of our simulations, in which the carrier density is allowed to vary continuously along the device length, indicate that there can be significant variations over a uniformly pumped section. Even in the extreme case of

a uniformly biased laser, simulations show that these fluctuations can have a large effect on the device output.

Another approximation that is often made when non-uniformly pumped lasers are modelled is to simplify the spectral characteristics of the device. Some authors assume single mode operation,[64-76] or consider only a small number of optical wavelengths,[77,78] or oversimplify the spectral distributions of spontaneous and stimulated emission.[79,80] These approximations reduce the required number of calculations involved in the simulations, while still allowing predictions of the total optical output power. However, in many situations it is desirable to generate more detailed information about the spectral properties of the lasers, especially for applications where wavelength sensitivity is crucial.

In order to avoid the complicated mathematical analysis, several groups in the past have restricted the level of time-domain analysis that they perform. By solving the device equations under steady-state[81-95] or small-signal[96,97] conditions, it is possible to reduce the complexity of the problem. This limits the applicability of the model under some conditions, however, particularly in situations where self-sustained pulsations (which are generally large-signal phenomena) occur, or when switching times between bistable states are of interest.

A final deficiency with some previous models of non-uniform laser pumping is that their results are often presented in terms of unmeasurable (or very difficult to measure) device parameters.[98-108] Concepts such as photon and carrier lifetimes, parabolic gain/absorption coefficients, and transparency carrier densities can be useful when one is trying to mathematically describe the causes of observed phenomena. However, they are generally approximations that may incorporate the effects of several different physical processes, and are often not easily extracted from a real device. In our work we have attempted, as far as possible, to characterize the structures in terms of physically

measurable parameters: the device dimensions and material, bias currents, and injected light wavelengths and powers.

1.4.2: Thesis Goals

In Section 1.4.1 we outlined a number of shortcomings in previous split-electrode laser modelling. This is not to imply that these works are incorrect or of little use in themselves; we merely seek to demonstrate that there is room for further development in the field. The first goal of the present work is therefore to construct a physical model of non-uniformly pumped semiconductor lasers, while trying as far as possible to avoid the limitations discussed above.

By doing this we hope to achieve two aims: first, from an academic point of view we hope to be able to describe the underlying physics that governs the behaviour of these devices, to facilitate a better understanding of them. This aim requires that we minimize the use of empirical, parameter-fitting techniques in our development. The second, more practical reason for formulating our model is to serve as an aid in future design: hopefully the number of expensive and time-consuming experimental iterations needed to optimize a device can be reduced by performing numerical simulations. Although such simulations could, in principle, be performed using a simpler, empirical model, this would leave us with little insight into the fundamental device physics.

The second goal of this thesis is to perform an experimental study of non-uniformly pumped lasers. As with the modelling, we again have two related motivations for undertaking this research. The first aim is to provide experimental data that can confirm (or refute) the results of our numerical modelling, since the simulations are only of practical value to the extent that they describe a real system. The second reason for this investigation is to collect empirical data pertaining to the devices. We may find that the approximations

of our theory limit its applicability in some situations, or simply that the experiments can be carried out more easily than a proper theoretical treatment. In either case, a body of experimental data can expedite the optimization of future device designs.

1.4.3: Outline of Thesis

In order to record and communicate the results of our investigation of non-uniform pumping effects in semiconductor lasers, we have prepared this written work. The structure of the remainder of the text is as follows: in Chapter 2 we develop the equations that are used to model the devices, and attempt to justify their form in terms of the physical phenomena involved. The result is a time-domain description of the photon and carrier distributions in the active region of the laser. A number of numerical simulations that are generated from these equations are presented in Chapter 3. These include simulations of both uniform and non-uniform electrically biased devices, as well as the use of optical pumping. Our experimental techniques and observations are outlined in Chapter 4: these are comprised of the output power and spectral characteristics of a series of multiple-contact, ridge-waveguide, InGaAsP/InP lasers. Finally, in Chapter 5 we summarize the results of our work, including both the contributions that we have feel we have made and areas where future work would be beneficial.

Chapter 1: References

[1] Aristotle, Metaphysics, Cambridge, Massachusetts: Harvard University Press, 1989, p. 2
[2] Aristotle, On The Soul, Cambridge, Massachusetts: Harvard University Press, 1986, p. 105
[3] Iizuka, Keigo, Engineering Optics, Heidelberg, Germany: Springer-Verlag, 1985, p. 6
[4] ibid, p. 7
[5] ibid, p. 25

[6] For a good overview of semiconductor structures and devices, see: Yang, Edward S., Microelectronic Devices, Toronto, Ont.: McGraw-Hill, Inc., 1988

[7] Zory, Peter S. ed., Quantum Well Lasers, San Diego, CA: Academic Press, Inc., 1993

[8] Kawaguchi, H., "Progress in optical functional devices using two-section laser diodes/amplifiers", *IEE Proceedings-J*, vol. 140, pp. 3-15, 1993

[9] Staring, A.A.M., Van Roijen, R., Binsma, J.J.M., Jansen, E.J., Sander-Jochem, M.J.H., Thijs, P.J.A., and Van Dongen, T., "Monolithically integrated tunable optical filter, amplifier and detector for HDWDM applications", *Electron. Lett.*, vol. 32, pp. 586-588, 1996

[10] Tang, X.-Y. and Chin, M.-K., "Optimal channel spacing of wavelength divisioin multiplexing optical soliton communications systems", *Optics Comm.*, vol. 119, pp. 41-45, 1995

[11] Udd, E., Fiber Optic Smart Structures, Toront, Ont.: John Wiley & Sons, Inc., 1995, Chapter 8 gives a good general overview of fiber optic strain sensing.

[12] Eddolls, D.V., Vass, S.J., Ash, R.M., and Park, C.A., "Two-segment multiquantum well lasers with 7 nm tuning range and narrow linewidth", *Electron. Lett.*, vol. 28, pp. 1057-1058, 1992

[13] Chang-Hasnain, C.J., Harbison, J.P., Zah, C.E., Florez, L.T., and Andreadakis, N.C., "Two-electrode vertical cavity surface emitting lasers", *Electron. Lett.*, vol. 27, pp. 1002-1003, 1991

[14] Zhang, L., and Cartledge, J.C., "Fast wavelength switching of three-section DBR lasers", *IEEE J. Quantum. Electron.*, vol. 31, pp. 75-81, 1995

[15] Kameda, T., Mori, H., Onuki, S., Kikugawa, T., Takahashi, Y., Tsuchiya, F., and Nagai, H., "A DBR laser employing passive-section heaters, with 10.8 nm tunng range and 1.6 MHz linewidth", *IEEE Photon. Technol. Lett.*, vol. 5, pp. 608-610, 1993

[16] Hervé, D., Mainguet, B., Pinel, S., Coquille, R., Poudoulec, A., and Delorme, F., "Narrow-band WDM spectrum analyser without mechanical tuning", *Electron. Lett.*, vol. 32, pp. 838-839, 1996

[17] Petermann, K., Laser Diode Modulation and Noise, Norwell, MA: Kluwer Academic Publishers, 1991, p. 304

[18] Nowell, M.C., Zhang, L.M., Carroll, J.E., and Fice, M.J., "Chirp reduction using push-pull moduation of three-contact lasers", *IEEE Photon. Technol. Lett.*, vol. 5, pp. 1365-1371, 1993

[19] Zory, P.S., op. cit., p. 252

[20] Petermann, K., op. cit., p. 125

[21] Lourtioz, J.-M., Chusseau, L., Brun, E., Hamaide, J.-P., Lesterlin, D., and Leblond, F., "Fourier-transform-limited pulses from gain-switched distributed-Bragg-reflector lasers using simultaneous modulation of gain and phase sections", *Electron. Lett.*, vol. 28, pp. 4499-4500, 1992

[22] Petermann, K., op. cit., p. 224

[23] Ikeda, M., Oku, S., and Ogasawara, M., "Optical tristability in two-section laser diode", *Electron. Lett.*, vol. 25, pp. 1701-1702, 1989

[24] Uenohara, H., Iwamura, H., and Naganuma, M., "Switching characteristics of InGaAs/InP multiquantum well voltage-controlled bistable laser diodes", *Jpn. J. Appl. Phys.*, vol. 29, pp. L2442-L2444, 1990

[25] Hui, R., "Static and dynamical properties of dispersive optical bistablity in semiconductor lasers", *J. Lightwave Technol.*, vol. 13, pp. 42-48, 1995

[26] Uenohara, H., Kawamra, Y., Iwamura, H., "Long-wavelength multiple-quantum-well voltage-controlled bistable laser diodes", *IEEE J. Quantum Electron.*, vol. 31, pp. 2142-2147, 1995

[27] Li, J., and Wang, Q., "A common-cavity two-section InGaAsP/InP bistable laser with a low optical switching power", *Opt. Commun.*, vol. 83, pp. 71-75, 1991

[28] Zhou, J., Cada, M., Li, G.P., and Makino, T., "Bistable characteristics and all-optical set-reset operations of 1.55-μm two-segment strained multiquantum-well DFB lasers", *IEEE Phot. Technol. Lett.*, vol. 7, pp. 1125-1127, 1995

[29] Hörer, J., Weich, K., Möhrle, M., and Sartorius, B., "Optimization of the optical switching characteristics of two-section Fabry-Perot lasers", *IEEE Phot. Technol. Lett.*, vol. 5, pp. 1273-1276, 1993

[30] Uenohara, H., Kawamura, Y., Iwamura, H., Nonaka, K., Tsuda, H., and Kurokawa, T., "Side-light-injection MQW bistable laser using saturable absorption and gain quenching", *Electron. Lett.*, vol. 28, pp. 1973-1975, 1992

[31] Marcenac, D.D. and Carroll, J.E., "Distinction between multimoded and singlemoded self-pulsations in DFB lasers", *Electron. Lett.*, vol. 30, pp. 1137-1138, 1994

[32] Simler, Y., Gamelin, J., and Wang, S., "Pulsation stablilization and enhancement in self-pulsing laser diodes", *IEEE Photon. Technol. Lett.*, vol. 4, pp. 329-332, 1992

[33] ibid.

[34] Barnsley, P. and Wickes, H., "All optical clock recovery from 2.5 GBit/s NRZ data using a self pulsating 1.56 μm laser diode", *Electron. Lett.*, vol. 28, pp. 4-5, 1992

[35] Farrell, G., Phelan, P., Hegarty, J., and Shields, J., "All-optical timing extraction with frequency division using a twin-section laser diode", *IEEE Photon. Technol. Lett.*, vol. 5, pp., 718-721, 1993

[36] Phelan, P., McDonald, D., Egan, A., Hegarty, J., O'Dowd, R., Farrell, G., and Lindgren, S., "Comparison of self-pulsation in multisection lasers with distributed feedback and intracavity saturable absorbers", *IEE Proc.-Optoelectron.*, vol. 141, pp. 114-118, 1994

[37] Barnsley, P., "All-optical clock extraction using two-contact devices", *IEE Proc. J*, vol. 140, pp. 325-336, 1993

[38] Verdeyen, Joseph Thomas, Laser Electronics, Second Edition, Englewood Cliffs, New Jersey: Prentice Hall, 1989, Section 9.4

[39] Schell, M., Tsuchiya, M., and Kamiya, T., "Chirp and stability of mode-locked semiconductor lasers", *IEEE J. Quantum Electron.*, vol. 32, pp. 1180-1190, 1996

[40] Zory, P.S. op. cit., p. 267

[41] Zhu, B., White, I.H., Williams, K.A., Laughton, F.R., and Penty, R.V, "High-peak-power picosecond optical pulse generation from Q-switched bow-tie laser with a tapered traveling wave amplifier", *IEEE Photon. Technol. Lett.*, vol. 8, pp. 503-505, 1996

[42] Koren, U., Miller, B.I., Young, M.G., Chien, M., Raybon, G., Brenner, T., Ben-Michael, R., Dreyer, K., and Capik, R.J., "Polarisation insensitive semiconductor optical amplifier with integrated electroabsorption modulators", *Electron. Lett.*, vol. 32, pp. 111-112, 1996

[43] Petermann, K., op. cit., p. 46

[44] Lang, R., "Injection locking properties of a semiconductor laser", *IEEE J. Quantum Electron.*, vol. QE-18, pp. 976-983, 1982

[45] Numai, T., "1.5 μm optical filter using a two-section Fabry-Perot laser diode with wide tuning ragne and high constant gain", *IEEE Photonics Technol. Lett.*, vol. 2, pp. 401-403, 1990

[46] Li, J. et al., 1991, op. cit.

[47] Hörer, J. et al., 1993, op. cit.

[48] Okada, M., Kikuchi, H., Takizawa, K., and Fujikake, H., "The effects of a detuned optical input on bistable laser diodes with inhomogeneous current injection", *IEEE J. Quantum Electron.*, vol. 29, pp. 109-120, 1993

[49] Barnsley, P., 1993, op. cit.

[50] Lasher, G.J., "Analysis of a proposed bistable injection laser", *Solid-St. Electron.*, vol. 7, pp. 707-716, 1964

[51] Baoxun, D., "A theory on stability of double-section semiconductor lasers", *IEEE J. Quantum Electron.*, vol. 25, pp. 847-849, 1989

[52] Paradisi, A. and Montrosset, I., "Numerical modeling of bistable laser diodes with saturable absorbers", *IEEE J. Quantum Electron.*, vol. 27, pp. 817-823, 1991

[53] Le Bihan, J., Goujon, J.-M., Auffret, R., and Chawki, M.J., "Theoretical characteristics of a tunable two-electrode Fabry-Perot (TEFP) laser diode", *J. Lightwave Technol.*, vol. 10, pp. 1931-1934, 1992

[54] Lee, C.-H., Shin, S.-Y., and Kang, S.-G., "Perturbation solution of self-pulsing in semiconductor lasers with a saturable absorber", *IEEE J. Quantum Electron.*, vol. 30, pp. 1396-1404, 1994

[55] Chen, J., Wu, Z., Xia, G., and Lu, Y., "Simple equations used to study the wavelengths of two-segment bistable laser diodes", *Opt. Lett.*, vol. 20, pp. 1298-1300, 1995

[56] Duan, G.-H., Landis, P., and Jacquet, J., "Modeling and measurement of bistable semiconductor lasers", *IEEE J. Quantum Electron.*, vol. 30, pp. 2507-2515, 1994

[57] Ozeki, Y. and Tang, C.L., "New two-mode bistability in an asymmetric absorptive multisection laser diode: theoretical analysis", *IEEE J. Quantum Electron.*, vol. 27, pp. 1160-1170, 1991

[58] Bandelow, U., Wünsche, H.J., and Wenzel, H., "Theory of selfpulsations in two-section DFB lasers", *IEEE Photon. Technol. Lett.*, vol. 5, pp. 1176-1179, 1993

[59] Griffel, G., Lang, R.J., and Yariv, A., "Two-section gain-levered tunable distributed feedback laser with active tuning section", *IEEE J. Quantum Electron.*, vol. 30, pp. 15-18, 1994

[60] Paschos, V., Sphicopoulos, T., Syvridis, D., and Caroubalos, C., "Influence of thermal efects on the tunability of three-electrode DFB lasers", *IEEE J. Quantum Electron.*, vol. 30, pp. 660-667, 1994

[61] Ottolenghi, P., Benedetto, S., and Montrosset, I., "Switching and optical modulation of three-section DBR lasers", *IEEE J. Quantum Electron.*, vol. 30, pp. 1381-1388, 1994

[62] Nugent, D.G.H., Plumb, R.G.S., Fisher, M.A., and Davies, D.A.O., "Self-pulsations in vertical-cavity surface-emitting lasers", *Electron. Lett.*, vol. 31, pp. 43-44, 1995

[63] Zhang, L. et al., 1995, op. cit.

[64] Agrawal, G.P., "Chirp minimization and optimum biasing for current-modulated coupled-cavity semiconductor lasers", *Opt. Lett.*, vol. 10, pp. 10-12, 1985

[65] Ueno, M. and Lang, R., "Conditions for self-sustained pulsation and bistability in semiconductor lasers", *J. Appl. Phys.*, vol. 58, pp. 1689-1692, 1985

[66] Baoxun, D., 1989, op. cit.

[67] Adams, M.J., "Theory of two-section laser amplifiers", *Opt. Quantum Electron.*, vol. 21, pp. S15-S31, 1989

[68] Okada, M., Takizawa, K., Kikuchi, H., and Fujikake, H., "Undershooting and set-reset operation in bistable laser diodes with inhomogeneous excitation", *IEEE J. Quantum Electron.*, vol. 26, pp. 850-857, 1990

[69] Adams, M.J., Barnsley, P.E., and Chen., J., "Effects of spontaneous emission on hysteresis loops in bistable laser diodes", *Electron. Lett.*, vol. 28, pp. 395-396, 1992

[70] Szczepanski, P., Kujawski, A., and Wosinska, L., "Nonlinear operation of lasers with a saturable absorber", *J. Mod. Optics*, vol. 40, pp. 1107-1122, 1993

[71] Hui, R., Benedetto, S., and Montrosset, I., "Optical bistability in diode-laser amplifiers and injection-locked laser diodes", *Optics Lett.*, vol. 18, pp. 287-289, 1993

[72] Thedrez, B. and Lee, C.H., "Effect of the spatial gain and intensity variations on a two-section Fabry-Perot semiconductor laser: an analytical study", *IEEE J. Quantum Electron.*, vol. 29, pp. 864-876, 1993

[73] Mitchell, N.F., O'Gorman, J., and Hegarty, J., "Optical bistability in asymetric Fabry-Perot laser-diode amplifiers", *Optics Lett.*, vol. 19, pp. 269-271, 1994

[74] Lee, C.-H. et al., 1994, op. cit.

[75] Duan, G.-H. et al., 1994, op. cit.

[76] Uenohara, H., Takahashi, R., Kawamura, Y., and Iwamura, H., "Static and dynamic response of multiple-quantum-well voltage-controlled bistable laser diodes", *IEEE J. Quantum Electron.*, vol. 32, pp. 873-883, 1996

[77] Li, L., "Static and dynamic properties of injection-locked semiconductor lasers", *IEEE J. Quantum Electron.*, vol. 30, pp. 1701-1707, 1994

[78] Lin, C.-F. and Ku, P.-C., "Analysis of stability in two-mode laser systems", *IEEE J. Quantum Electron.*, vol. 32, pp. 1377-1382, 1996

[79] Le Bihan et al., 1992, op. cit.

[80] Zhang, L. et al., 1995, op. cit.

[81] Kikuchi, K. and Tomofuji, H., "Analysis of oscillation characteristics of separated-electrode DFB laser diodes", *IEEE J. Quantum Electron.*, vol. 26, pp. 1717-1727, 1990

[82] Paradisi, A. and Montrosset, I., "Analysis of wavelength conversion using a multisection DBR laser with a saturable absorber", *IEEE J. Quantum Electron.*, vol. 29, pp. 1285-1294, 1993

[83] Griffel, G. et al., 1994, op. cit.

[84] Lasher, G.J., 1964, op. cit.

[85] Ueno, M. et al., 1985, op. cit.

[86] O'Dowd, R.F. and Davis, M.G., "Theoretical study of a two-section single-cavity semiconductor laser for use as a wavelength-tunable source", *Opt. Quantum Electron.*, vol. 20, pp. 383-393, 1988

[87] Paradisi, A. et al., 1991, op. cit.

[88] Middlemast, I., Sarma, J., Shore, K.A., Kurcharska, A.I., Fletcher, E.D., and Blood, P., "Absorptive bistability in inhomogeneously pumped quantum well laser diodes", *IEE Proc.-J*, vol. 138, pp. 301-308, 1991

[89] Le Bihan, et al., 1992, op. cit.

[90] Adams, M.J. et al., 1992, op. cit.

[91] Thedrez, B. et al., 1993, op. cit.

[92] Szczepanski, P. et al., 1993, op. cit.

[93] Mitchell, N.F. et al., 1994, op. cit.

[94] Chen, J. et al., 1995, op. cit.

[95] Lin, C.-F. et al., 1996, op. cit.

[96] Agrawal, G.P., 1985, op. cit.

[97] Li, L., 1994, op. cit.

[98] Ueno, M. et al., 1985, op. cit.

[99] Lin, C.-F. et al., 1996, op. cit.

[100] Chen, J.C., Haus, H.A., and Ippen, E.P., "Stability of lasers mode locked by two saturable absorbers", IEEE J. Quantum Electron., vol. 29, pp. 1228-1232, 1993

[101] Adams, M.J., 1989, op. cit.

[102] Okada, M. et al., 1990, op. cit.

[103] Lee, C.-H. et al., 1994, op. cit.

[104] Thedrez, B. et al., 1993, op. cit.

[105] Szczepanski, P. et al., 1993, op. cit.

[106] Mitchell, N.F.et al., 1994, op. cit.

[107] Ozeki, Y. et al., 1991, op. cit.

[108] Bandelow, U. et al., 1993, op. cit.

CHAPTER 2: LASER THEORY

In any subject which has principles, causes, and elements, scientific knowledge and understanding stems from a grasp of these, for we think we know a thing only when we have grasped its first causes and principles and have traced it back to its elements.

Aristotle, *Physics* I.i.184^a10[1]

2.1: INTRODUCTION

The fundamental goal of this thesis is to contribute to our understanding of non-uniformly pumped semiconductor lasers, with the ultimate goal of improving device performance and versatility. It seems that the best approach to this problem would be to begin with the principles of optics and semiconductor physics, and attempt to understand how the interplay of these factors causes the laser to operate as it does. Proceeding along these lines, in this chapter we therefore derive a model of a Fabry-Perot cavity semiconductor laser that is capable of describing non-uniform pumping effects. It can be applied to either a split-electrode geometry, in which case the bias is electrical, or to optical pumping of the cavity through the laser facets, or to a combination of these. Under such conditions several interesting effects can be observed, including hysteresis in the optical output of the laser,[2-7] self-sustained optical pulse generation,[8-12] and wavelength tuning.[13-15]

Previous non-uniformly pumped laser models have succeeded in predicting these effects to various degrees, but each has had its limitations. For example some researchers[16-21] have solved a set of steady-state equations for the device output, which allowed them to predict hysteresis in the laser's optical characteristics. However, the fact that these models must set all time derivatives to zero means that they cannot predict temporal variations such as self-pulsation. Other workers[22-29] have made the assumption that the carrier concentration is uniform in each section of a multiple-contact laser.

Simulations based on our model show that this is not the case under all circumstances, and that the assumption can significantly affect the predicted device behaviour. In some cases[30,31] the treatment of the wavelength dependence of the optical gain and spontaneous emission rates is somewhat simplified. We have attempted a more detailed analysis of the interaction of the optical energy in the cavity with the active region material, which leads to a more realistic simulation of the spectral properties of the devices.

Figure 2.1.1 illustrates schematically the structure of the lasers we consider in this chapter. The device consists of a narrow band-gap active region sandwiched between two wider band-gap layers that serve to confine both the carriers and light in the active region. Electrical connection is made through a ground contact that covers the bottom of the device uniformly, and a split top contact that divides the laser into two (or more) sections that can be biased independently. The optical feedback necessary for lasing action is provided by reflections at the facets, so that the active region constitutes a Fabry-Perot cavity.

The parameters in Fig. 2.1.1 that we wish to model are the carrier concentration, $n(x)$, and the optical energy in the cavity, represented by the photon concentrations, $S_m^+(x)$ and $S_m^-(x)$. In our notation, the superscripts (+) and (-) indicate the direction in which the light propagates, relative to the x-axis. The subscript (m) denotes a particular optical mode of the laser. We allow significant photon concentrations to exist in multiple cavity modes, each population interacting with the active region material according its wavelength and the local carrier concentration.

In the theory developed here we have attempted to make improvements over the previous models mentioned above, although some accuracy must be sacrificed to allow solutions to be found in a reasonable amount of time. For instance, we do not attempt to

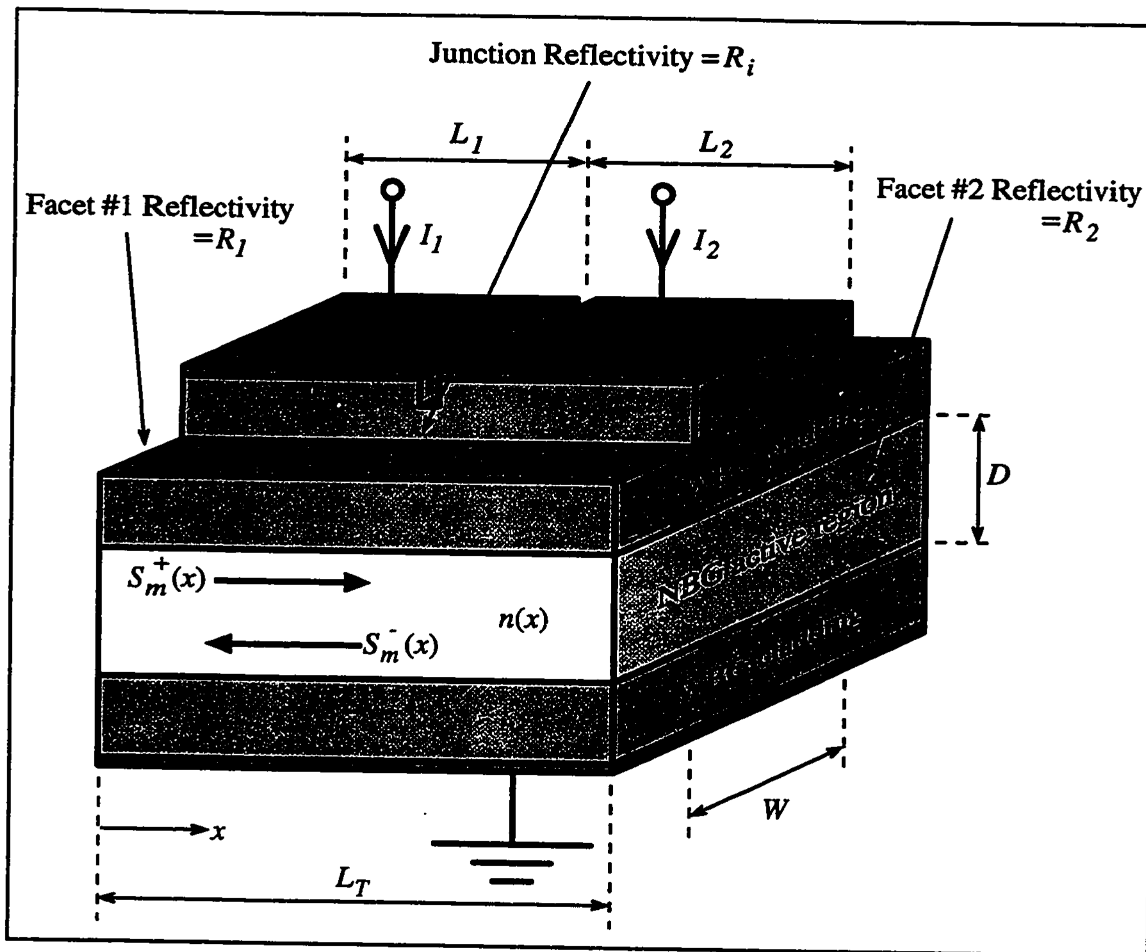

Figure 2.1.1: Schematic of the Non-uniformly Pumped Laser
The relevant dimensions are indicated on the figure, as are the bias currents and reflectivities considered. S_m^+ and S_m^- indicate light moving in the positive and negative directions, respectively, while n is the carrier density. The subscript m denotes the different cavity modes of the laser.

model the contacts or cladding regions shown in Fig. 2.1.1 in any great detail. We assume that carriers are injected through resistanceless contacts directly into the active region of the laser. This approach simplifies the model by allowing us to neglect carrier drift, diffusion and recombination in the cladding, but we consequently lose the ability predict the voltage drop for a given current bias. However, since these processes occur

outside the active region, they are not expected to have a strong influence on the optical output of the laser.[a] Because of this simplified view of the cladding region, we have not attempted to model carrier leakage out of the active region. This may cause us to underestimate the bias currents needed to achieve a particular simulation condition, but should not otherwise affect the predictions of the model to a great extent.

Another simplification that we have made is to use a one-dimensional model to approximate the laser active region. This means that we account only for longitudinal variations in the carrier and photon concentrations. The diffusion of carriers from under the ridge that defines the width of the active region in Fig. 2.1.1, and the shape of lateral optical modes in the cavity are not considered. These assumptions may influence the data calculated using the model, but it should be remembered that the factors that make a non-uniformly pumped device different from a normal semiconductor laser are *longitudinal* differences (in either carrier or photon injection). We therefore assume that if the simulations for the case of uniform injection are sound, we can trust the model to the same extent when it comes to the non-uniformly pumped cases.[b]

In order to produce a practical set of equations, the third approximation we have made is that the optical energy in the device can be modelled in terms of the photon concentration at each point. This means that we formulate our expressions in terms of optical *power*, and not the corresponding *electric field*. The problem with this method is that we lose any information involving the phase of the field in the cavity. For this reason, effects such as spatial hole burning and shifts in the cavity modes due to varying index of refraction cannot be extracted directly from the model.[c] Although these issues can be of

---

[a] See, for example, Section 4.2, in which we discuss the implications of the measured resistance between the top contacts.

[b] Both uniformly and non-uniformly pumped simulations are presented in Chapter 3.

[c] Variations in the refractive index are simulated to a limited extent in Section 3.8.

importance in a real laser, we neglect them here primarily for practical reasons. By working with photon concentrations instead of electric fields we simplify the equations considerably, and reduce the required amount of numerical computation by at least an order of magnitude.

Finally, we make the assumption of simple, isotropic, parabolic energy bands in the active region of our semiconductor laser. This gives a reasonably accurate description of the density of states for an ordinary double-heterostructure laser, but does not represent a quantum well device correctly. We make this assumption for two reasons. Firstly, the resulting equations are less complicated than those for the quantum well case, which significantly decreases the computational time required to find a solution. Secondly, although the material absorption parameters used in Section 2.3.3 to find $\alpha_o(\nu)$ are reasonably well established for bulk quaternary material, the values that would be needed to accurately describe a quantum structure are considerably less well known.[a] In order to avoid using a number of fitting parameters to match to each individual quantum well structure, it was decided that it would be more practical just to consider the bulk case.

Now that we have outlined the goal of our model and some of the constraints that have been imposed on it, we can begin analyzing the physics involved in non-uniformly pumped lasers. In Section 2.2 we introduce the rate equation that is the basis for our description of the behaviour of the carrier concentration in the active region. Sections 2.3 and 2.4 describe the expressions needed to determine the carrier recombination rate and the optical gain coefficient. The photon rate equations, which must be solved simultaneously with the carrier rate equation, are developed in Section 2.5.

---

[a] In fact, the absorption coefficient will be different for TE and TM polarizations, so some sort of "effective" value would have to be used.

2.2: Carrier Rate Equation

In order to model the carrier concentration in the active region we employ the following equation:

$$\frac{dn(t,x)}{dt} = \frac{J(t,x)}{qD} - \frac{kT\mu}{q}\frac{\partial^2 n}{\partial x^2} - R_r(n) - \sum_{m=0}^{M} G_m(n)\left[S_m^+(t,x) + S_m^-(t,x)\right]\frac{v_m}{DW} \qquad (2.2.1)$$

In this expression, the term to the left of the equal sign describes the time evolution of the carrier concentration along the cavity length. The first term on the right side represents the rate at which carriers are introduced to the active region by current injection through the contacts. q and D represent the charge of an electron and thickness of the active region, respectively. $J(t,x)$, the current density flowing into the cavity, is the independent variable for the calculations that follow; the function chosen for this determines the laser bias as a function of time. The fact that J can vary with x allows carriers to be injected into different sections of the laser at different rates.

The second term on the right side of eq. (2.2.1) accounts for the diffusion of carriers longitudinally in the active region of the laser; k, T, and μ are, respectively, Boltzmann's constant, the absolute temperature, and the carrier mobility.

The carrier recombination rate associated with spontaneous emission and all non-radiative mechanisms is represented by the third term. An explicit expression for $R_r(n)$ is described in Section 2.3, where we assume that unimolecular and Auger are the dominant non-radiative mechanisms.

The final term on the right side of eq. (2.2.1) accounts for the coupling of the carriers in the active region with the photon flux. The factor G_m represents either the gain of the mth cavity mode, when $G_m > 0$, or the absorption, for $G_m < 0$, and is described in Section 2.4. S_m^+ is the number of photons per unit of cavity length in mode m travelling in

the +x direction, and S_m^- similarly defined for the -x direction; expressions for these terms are derived in Section 2.5. v_m is the photon speed, and W is the active region width. In this final term in eq. (2.2.1), it is necessary to sum over the total number of optical modes in the cavity, M, to account for variations in gain/absorption and photon density at the various wavelengths present in the active region.

2.3: THE CARRIER RECOMBINATION RATE

2.3.1: The Non-Stimulated Carrier Recombination Rate, R_r

The non-stimulated carrier recombination rate is assumed to include all mechanisms that are not functions of the photon concentration: the three terms we consider are a unimolecular term, a spontaneous* radiative bimolecular term, and an Auger recombination term. For simplicity, because they are non-radiative processes, we take the unimolecular and Auger components to be simply proportional to the excess carrier concentration and its cube, respectively. However, because we intend to model the optical output of the device in some detail, we introduce the spontaneous recombination term $R_{sp}(n,\lambda)$ which is dependent on the wavelength of the emitted light. A derivation of the expression for $R_{sp}(n,\lambda)$ is given in Section 2.3.2, below.

Utilizing these approximations, the non-stimulated recombination rate can be written as

$$R_r(n) = A(n-n_o) + \int_0^{\infty} R_{sp}(n,\lambda)d\lambda + C(n-n_o)^3 \qquad (2.3.1)$$

* Recombination involving stimulated emission is discussed in Section 2.4.1.

Values for the unimolecular (A) and Auger (C) coefficients are given in the Glossary in Appendix D.

2.3.2: The Spontaneous Recombination Rate, R_{sp}

The method for determining $R_{sp}(n,\lambda)$ in this subsection follows that outlined in Verdeyen[32]. In order to arrive at an expression for $R_{sp}(n,\lambda)$, we begin by considering an arbitrary volume of homogeneous material in thermal equilibrium with its surroundings. Given this condition, we know that the spectral distribution of the light emitted by the material must correspond to blackbody radiation at the ambient temperature:[33]

$$\rho(\nu) = \frac{8\pi n_r^3 \nu^2}{c^3} \frac{h\nu}{e^{h\nu/kT} - 1} \tag{2.3.2}$$

where $\rho(\nu)$ is the power density of the blackbody spectrum.

Also, in equilibrium there must be no net flow of energy through any arbitrary surface we might choose to construct in the material. This means that any optical energy generated in the material at a given wavelength must be balanced by re-absorption at the same wavelength. We therefore equate the radiative recombination rate with the rate of photon absorption:

$$R_o(\nu) = \alpha_o(\nu) \frac{c}{n_r} \frac{\rho(\nu)}{h\nu} \tag{2.3.3}$$

where R_o and α_o are, respectively, the radiative recombination rate and the absorption per unit length of the material under equilibrium conditions. Combining eqs. (2.3.2) and (2.3.3) and re-arranging, we get

$$R_o(\nu) = 8\pi\left(\frac{n_r \nu}{c}\right)^2 \alpha_o(\nu) e^{-h\nu/kT} \quad (2.3.4)$$

where we have made use of the approximation that $\frac{h\nu}{kT} >> 1$.

Now, eq. (2.3.4) has been derived for the particular case of equilibrium. However, in general we know that the radiative recombination rate is proportional to the probability of the transition states being occupied. For a general transition between two states, the rate is proportional to the number of states available for the transition (ρ_{red}), the occupancy of the states (f_c and f_v), and the strength of the coupling between the states (B_r). Expressing this mathematically, we have

$$R_{sp}(n,\nu) = B_r(E)\rho_{red}(E) f_c(E_u)[1 - f_v(E_l)] \quad (2.3.5)$$

where $E = h\nu$ is the photon energy, $B_r(E)$ represents the strength of the coupling between the states, and $f_c(E)$ and $f_v(E)$ are the electron occupancy functions in the conduction and valence bands, respectively. The reduced density of states, ρ_{red}, is given by[34]

$$\rho_{red}(E) = \frac{1}{4\pi^2}\left[\frac{2}{\hbar^2}\left(\frac{m_e m_h}{m_e + m_h}\right)\right]^{1.5} \sqrt{E - E_g}.$$

In eq. (2.3.5), E_u and E_l are, respectively, the upper and lower energy levels of the transition, and are given by[35]

$$E_u = \frac{m_h}{m_e + m_h}(E - E_g) + E_c \quad \text{and} \quad E_l = E_v - \frac{m_e}{m_e + m_h}(E - E_g).$$

Although eq. (2.3.5) is applicable to both equilibrium and non-equilibrium conditions, we can write it specifically for the former case as

$$R_o(\nu) = B_r(E)\rho_{red}(E)f_o(E_u)[1 - f_o(E_l)] \tag{2.3.6}$$

where $f_o(E)$ is the equilibrium carrier occupancy function. We assume that the functions $B_r(E)$ and $\rho_{red}(E)$ are the same for equilibrium and non-equilibrium conditions; that is, the density of states and the coupling between states are not a function of the carrier concentration or distribution. Changes in the recombination rate with carrier concentration are therefore due solely to changes in the occupancy functions.

Equating eqs. (2.3.4) and (2.3.6), solving for $B_r(E)$ in terms of $R_o(E)$, and substituting the resulting expression into eq. (2.3.5) yields

$$R_{sp}(n,\nu) = \frac{R_o(\nu)f_c(E_u)[1 - f_v(E_l)]}{f_o(E_u)[1 - f_o(E_l)]} \tag{2.3.7}$$

Converting $R_{sp}(n,\nu)$ into a function of wavelength yields

$$\begin{aligned} R_{sp}(n,\lambda) &= \frac{d\nu}{d\lambda}R_{sp}(n,\nu) \\ &= \frac{cR_o(\nu)f_c(E_u)[1 - f_v(E_l)]}{\lambda^2 f_o(E_u)[1 - f_o(E_l)]} \end{aligned} \tag{2.3.8}$$

Note that in taking $\frac{d\nu}{d\lambda} = \frac{c}{\lambda^2}$ we have dropped a negative sign to simplify the notation; this is, strictly speaking, incorrect, but as long as we choose the limits of integration appropriately, as indicated in eq. (2.3.1), it does not pose a problem.

In eq. (2.3.8) we have an explicit expression for the rate of spontaneous recombination that produces photons at wavelength λ. The occupancy functions can be modelled by the appropriate Fermi functions,

$$f_{c/v}(E) = \frac{1}{1+e^{(E-E_{F,c/v})/kT}} \tag{2.3.9}$$

and the expression for $R_o(\nu)$ is given by eq. (2.3.4). To completely describe the spontaneous recombination rate, we must now determine an expression for $\alpha_o(\nu)$.

2.3.3: The Equilibrium Absorption Coefficient, α_o

Although the equilibrium absorption coefficient can be evaluated theoretically using quantum mechanics, this approach is quite complicated, and would require a detailed knowledge of the actual band structure of the material used for the laser active region. The scope of this work does not warrant such an in-depth approach, so a few simplifying assumptions have been made. In general, α_o is proportional to the reduced density of states.[a] Under the approximation of simple, isotropic, parabolic bands, we can therefore express it as[36]

$$\alpha_o(\nu) = K\sqrt{h\nu - E_g} \tag{2.3.10}$$

The specific value of K used in this work was derived from "Properties of Indium Phosphide",[37] which tabulates the absorption of lattice-matched InGaAsP as a function of photon energy. We have interpolated the data in the above reference for a band-gap energy corresponding to a wavelength of 1.3 μm; this value of K is given in the Glossary, in Appendix D.

---

[a] Note that we consider only conduction-to-valence band absorption here. Effects such as impurity, intra-band, and intersubband absorption are not considered.

2.3.4: Summary of Spontaneous Recombination

The model developed in Section 2.3 allows us to calculate the radiative recombination rate, R_{sp}, as a function of carrier density, n. This method not only gives the total spontaneous recombination rate, which could have been described quite simply by an expression of the form

$$R_{sp,total} = B(n - n_o)^2$$

but also describes the recombination as a function of the wavelength of the emitted light. The primary equation is (2.3.8), into which are substituted eqs. (2.3.4) and (2.3.10). Fermi functions are used to model the occupancy functions, f_c, f_v, and f_o; the method of determining the relevant quasi-Fermi levels for a given carrier density is described in Section 2.4.2. Given solutions to eq. (2.3.8), the total radiative recombination rate can be found by integrating $R_{sp}(n,\lambda)$ over wavelength, as indicated in eq. (2.3.1).

The preceding development of our expression for $R_{sp}(n,\lambda)$ has been somewhat lengthy, so at this point it would seem worthwhile to demonstrate that it does, in fact, produce results that are physically realistic. Figure 2.3.1 illustrates the function $R_{sp}(\lambda)$, as defined by eq. (2.3.8), for several values of the carrier concentration, n. The plots have been normalized to the height of the $n = 10^{18}$ cm^{-3} curve, by the factors indicated in the figure. These curves portray the trends that we expect for spontaneous emission: the peak is at a wavelength slightly less than the band edge (1.3 μm), and varies in position and magnitude with carrier concentration. For example, at $n = 10^{18}$ cm^{-3} as λ decreases we see that $R_{sp}(\lambda)$ rises from zero at 1.3 μm, peaks at $\lambda = 1.24$ μm, and then drops

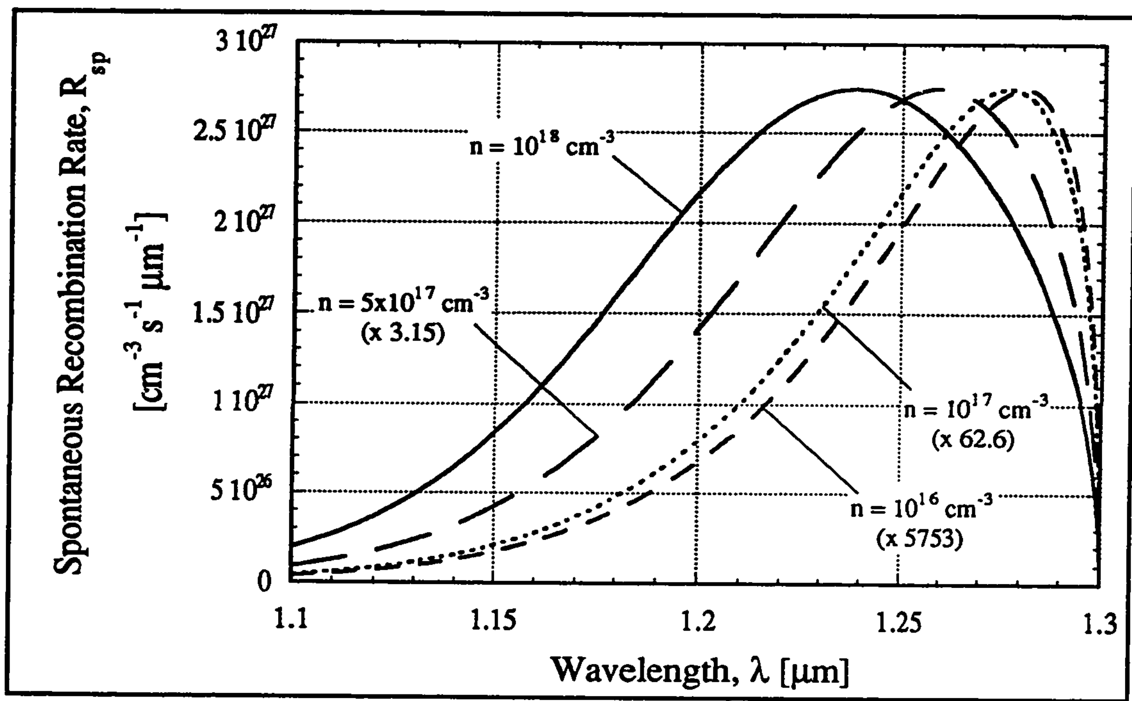

Figure 2.3.1: Spontaneous Recombination Rate vs. Wavelength

$R_{sp}(\lambda)$, the spontaneous recombination rate is plotted as a function of wavelength. The curves are generated from eq. (2.3.8), with the carrier concentrations indicated. They have been normalized to the same height, using the scaling factors given in the figure.

asymptotically to zero. For other values of n the curves retain the same form, but the peak shifts toward the band edge as the carrier concentration decreases.

It is also instructive to examine how the spontaneous recombination rate varies as a function of carrier concentration. From basic carrier statistics we expect the *total* spontaneous recombination rate, given by

$$R_{sp,total}(n) = \int_0^\infty R_{sp}(n,\lambda)d\lambda \qquad (2.3.11)$$

to be proportional to the square of n; this does not apply to the rate that photons of a fixed wavelength are generated, however. To illustrate this, we consider the following case: once the carrier concentration reaches degeneracy, the occupancy of energy levels close to the band edge becomes fixed at unity. Since the rate of photon generation is dependent on the number of carriers available ***in the appropriate energy levels***,[*] further increases in n do not affect the generation rate for wavelengths involving near-band-edge transitions. To demonstrate that these variations from $R_{sp}(n,\lambda) \propto n^2$ are inherent in eq. (2.3.8), we have plotted $R_{sp}(n,\lambda)/n^2$ vs. n in Fig. 2.3.2.

Examining Fig. 2.3.2, we see that for n less than approximately 10^{17} cm^{-3} the spontaneous recombination rate is proportional to the square of the carrier concentration at all wavelengths (i.e. the curves are horizontal lines). For the reasons described in the previous paragraph, the wavelengths closest to the band-gap (1.3 μm) begin to saturate as the carrier concentration increases beyond $n \sim 10^{17}$ cm^{-3}. Because $R_{sp,total}$ must remain proportional to n^2 for all values of n, $R_{sp}(n)$ at higher wavelengths increases more quickly than n^2. The solid line in Fig. 2.3.2 shows that $R_{sp,total}$ is indeed proportional to n^2; the slight variations from the straight, horizontal line we expect are due to the numerical technique used in the integration. Figure 2.3.2 illustrates the importance of this detailed modelling of the recombination rate; although $R_{sp,total}$ is proportional to n^2, if we had assumed this for the $R_{sp}(n,\lambda)$ relationship the resulting spontaneous emission spectra of our laser simulations would have been in error by up to an order of magnitude, for carrier concentrations near 10^{18} cm^{-3}.

---

[*] These levels are indicated by E_u and E_l in eq. 2.3.8.

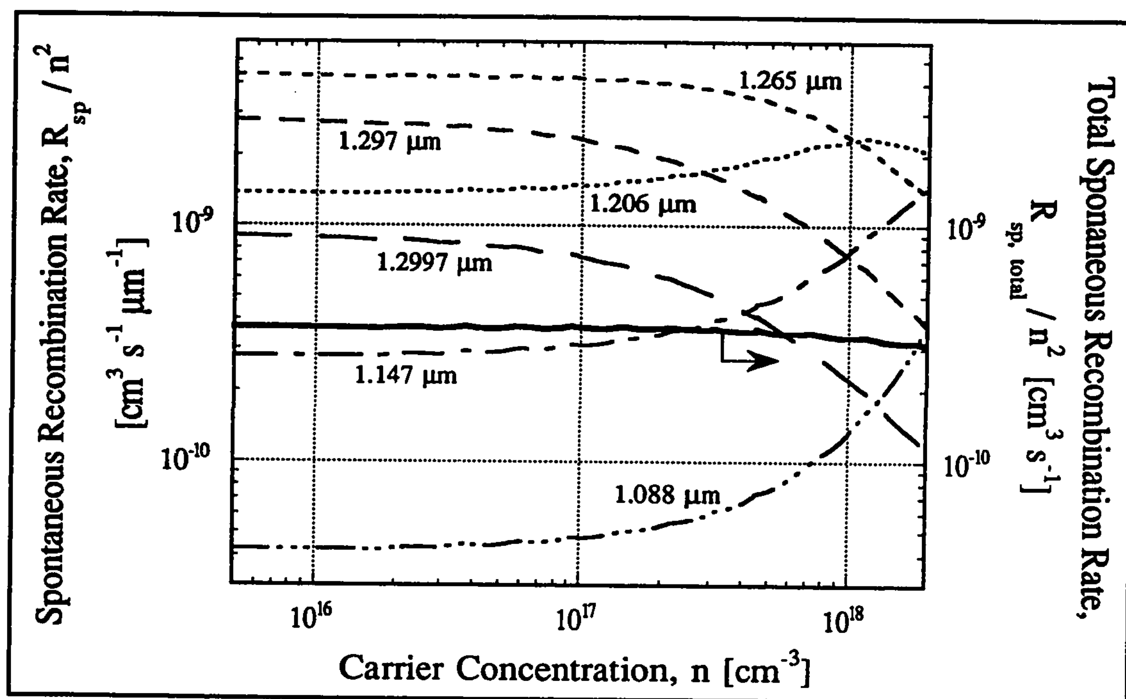

Figure 2.3.2: Spontaneous Recombination Rate vs. Carrier Concentration

The ratio $R_{sp}(n)/n^2$ is plotted vs. n, for the wavelengths indicated. The spontaneous recombination rate is divided by n^2 to make deviations from the simplistic model more apparent. In addition to the values of $R_{sp}(n)$ at specific wavelengths, the total radiative recombination rate (solid line) is also plotted. This curve has been determined by solving eq. (2.3.11) numerically.

2.4: The Optical Gain Coefficient

2.4.1: An Expression for the Optical Gain, G_m

The next term that we need to investigate in order to be able to solve eq. (2.2.1) is the optical gain coefficient, $G_m(n)$. The subscript m used here refers to the mth optical cavity mode of the laser. $G_m(n)$ represents the gain (or loss) that the optical energy in the mode experiences per unit length it travels. It should be noted that this is a material

property only, and does not include interface effects such as mirror losses or scattering effects. To model $G_m(n)$, we employ eq. (11.4.15b) from Verdeyen,[38] expressed as

$$G_m(n) = \Gamma_m \alpha_o(\lambda_m)[f_c(E_u) - f_v(E_l)] \tag{2.4.1}$$

where Γ_m is the optical confinement factor of the mth cavity mode, f_c and f_v are the electron occupancy functions in the conduction and valence bands, E_u and E_l are the upper and lower energy levels of the transition, and $\alpha_o(\lambda_m)$ is the absorption coefficient of the unbiased material at wavelength λ_m. $\alpha_o(\lambda_m)$ is described in Section 2.3.3, and expressions for E_u and E_l are given in Section 2.3.2.

2.4.2: The Fermi Level as a Function of Carrier Concentration, $E_{Fc/v}$

In order to calculate both the optical gain, $G_m(n)$, and the radiative recombination rate, $R_{sp}(n, \lambda)$, we assume the carrier distributions are described by Fermi statistics. It is therefore necessary to formulate an expression for the Fermi level as a function of carrier concentration. We can express the inverse of this function as[39]

$$n(E_{Fc}) = \frac{2N_c}{\sqrt{\pi}} \int_0^\infty \frac{\sqrt{E}\,dE}{1+e^{E-\Delta E_c}} \tag{2.4.2}$$

where N_c is the effective density of states in the conduction band,

$$N_c = 2\left(\frac{2\pi m_e kT}{h^2}\right)^{1.5},$$

and ΔE_c is the normallized energy difference between the Fermi level and the band edge,

$$\Delta E_c = \frac{E_{Fc} - E_c}{kT}.$$

In principle, eq. (2.4.2) defines the relationship between the carrier concentration, n, and the Fermi level, E_{Fc}; a similar expression can be written for p and E_{Fv} in the valence band. The function $n(E_{Fc})$ is defined explicitly by eq. (2.4.2), although the integration may have to be done numerically. However, the inverse function, $E_{Fc}(n)$, is transcendental, and cannot be written analytically. The details of the numerical technique used to solve for $E_{Fc}(n)$ are given in Appendix A.

2.4.3: Summary of the Optical Gain

Equation (2.4.1), together with the $E_{Fc}(n)$ relationship obtained from eq. (2.4.2), allows us to determine the gain coefficient needed to solve eq. (2.2.1). In order to better visualize the physical implications of this optical gain model, we next present two plots that illustrate how G_m varies with wavelength and carrier concentration.

Figure 2.4.1 depicts the gain as a function of the emitted photon wavelength, for several values of the carrier concentration, n. This figure shows that the active region cannot amplify light by stimulated emission until the carrier concentration has exceeded 9×10^{17} cm^{-3}, as the material[*] is absorbing for all wavelengths below this level. Above 9×10^{17} cm^{-3} light experiences gain for a range of wavelengths near the band-gap, and the wavelength at which the gain peak occurs shifts to shorter wavelengths as n increases. In a uniformly pumped laser, the peak wavelength is determined by the minimum carrier concentration for which G_m exceeds the cavity losses: lasing occurs at or near the peak of

---

[*] The active region is assumed to consist of InGaAsP lattice matched to InP, with a band-gap energy corresponding to 1.3 μm, throughout this work.

this curve. For a non-uniformly pumped laser the carrier concentration varies along the cavity length, and the lasing wavelength cannot be extracted from Fig 2.4.1 directly.

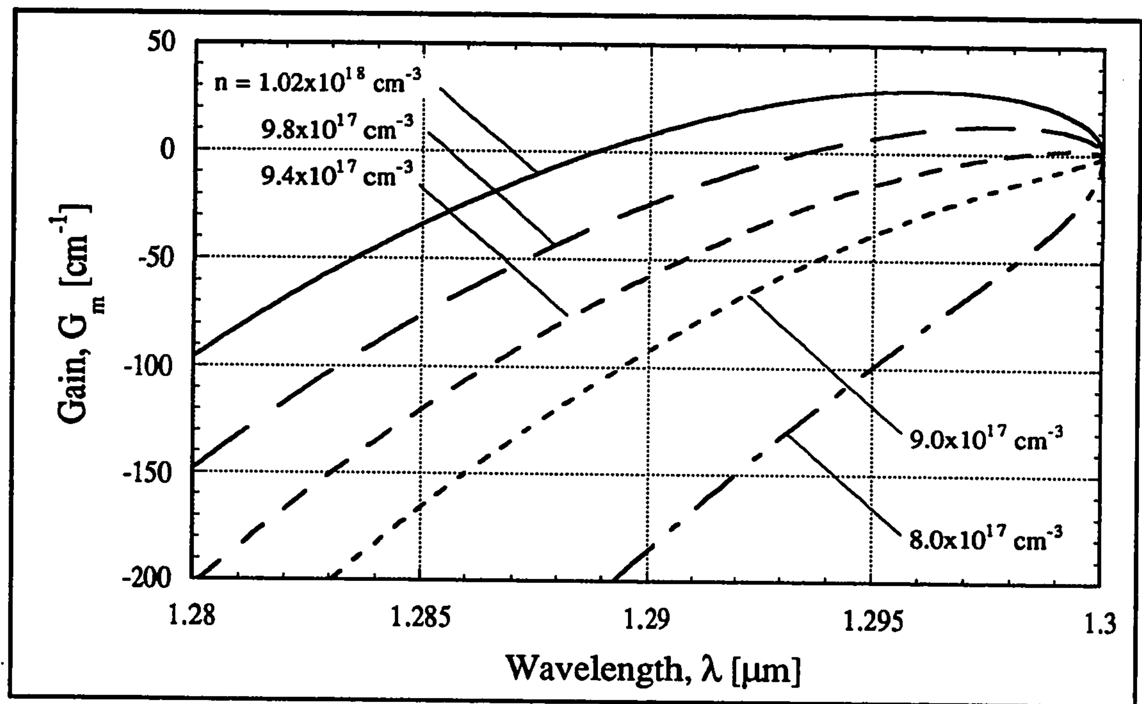

Figure 2.4.1: Optical Gain vs. Wavelength

The calculated gain, G_m, is plotted as a function of the wavelength, for InGaAsP material with a band-gap energy corresponding to 1.3 μm. Values of $G_m > 0$ indicate the light experiences gain, at $G_m = 0$ the material is transparent, and for $G_m < 0$ absorption occurs.

In Fig. 2.4.2 we have plotted G_m as a function of the carrier density in the material, for a variety of wavelengths. These wavelengths are given in terms of cavity modes, denoted by the mode number, m. Mode 0 is the cavity mode closest to the band-gap (at a wavelength $\lambda = \lambda_{bandgap}$ - 2.9 Å), mode 1 has the next smaller wavelength, and so on. Since we have assumed simple, parabolic bands for this work, $G_m = 0$ for all transitions at energies less than the band-gap.

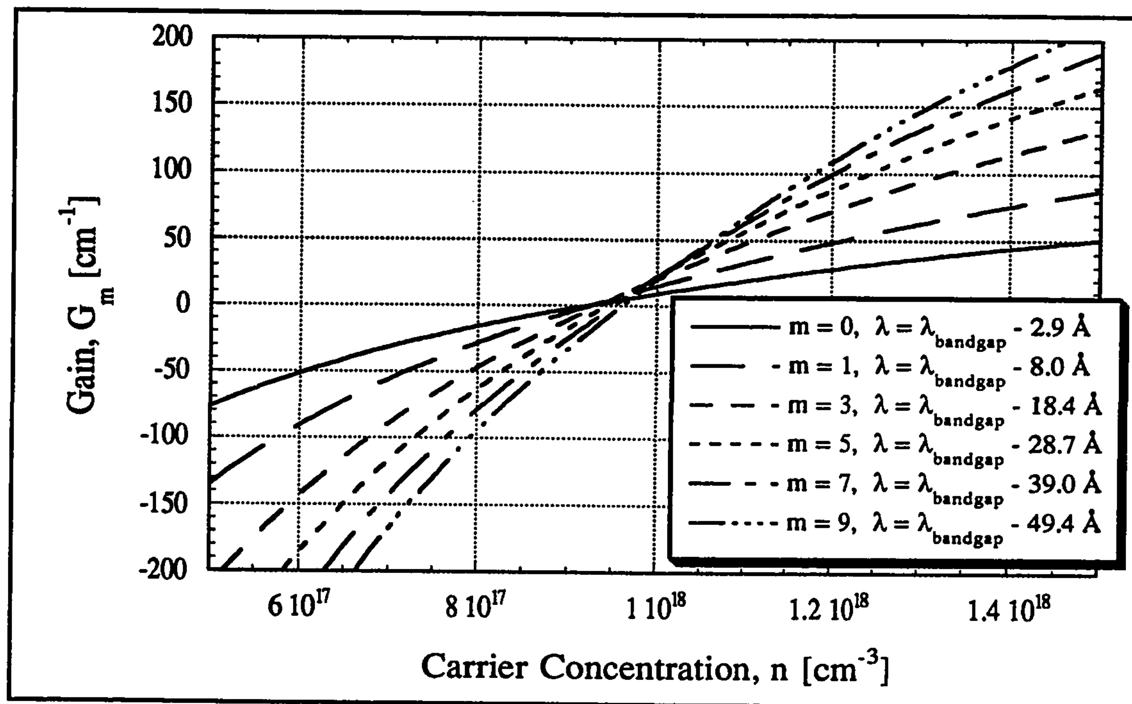

Figure 2.4.2: Optical Gain vs. Carrier Concentration

The gain calculated using eq. (2.4.1) is plotted as a function of the carrier concentration in the material. The wavelength corresponding to each curve is denoted by the mode number; the wavelength separation of the mode from the band edge is also given. Not all cavity modes are shown. Values of $G_m < 0$ indicate absorption, $G_m > 0$ denotes gain.

As Fig. 2.4.2 indicates, variations in G_m are not linear in n, and the slope of the curves is greater for the higher mode numbers (at the wavelengths farthest removed from the band edge). The carrier concentration corresponding to transparency (i.e. $G_m = 0$) also increases slightly with the mode number. It is the complicated dependence of G_m on n and λ that determines which mode(s) in a non-uniformly pumped laser actually lase. For instance, if one section of the cavity is strongly pumped (so that n is large) and the other weakly pumped (so that it is below transparency), light in the cavity experiences both gain and absorption as it passes through the device. The net, round trip gain must be determined by integrating over the entire device. This allows us, at least in principle, to

tune the lasing wavelength by adjusting the bias so that only the desired mode experiences a round trip gain sufficient to overcome the cavity losses. We demonstrate tuning of the laser wavelength based on this model in the simulations in Section 3.4.

2.5: Photon Rate Equations

2.5.1: Introduction

At this point we have determined expressions for all of the parameters needed to solve eq. (2.2.1), except for the photon concentrations, $S_m^+(t,x)$ and $S_m^-(t,x)$. However, these pose by far the most complicated problem, for several reasons. Firstly, the nature of the processes under investigation dictates that the relationship $S_m(n)$ is a differential one, instead of a "simple" algebraic one, as is the case for $G_m(n)$ and $R_{sp}(n)$. Secondly, the intriguing properties that are observed in split-contact lasers are a direct consequence of the highly non-linear coupling between the optical energy in the cavity and the carrier concentration. Thus, we must be careful when making any simplifying assumptions to ensure that our model retains the capacity to predict the behaviour that these devices are known to exhibit.

For these reasons we proceed as follows: in Section 2.5.2 we develop a set of time-independent equations, which, although they may be useful in some specific instances, are not ultimately applicable to the general problem of non-uniformly pumped lasers. After this, in Section 2.5.3 we generalize the model to properly include temporal variations, building on the results of Section 2.5.2. The resulting expressions are suitable for modelling semiconductor lasers with non-uniform pumping, at least to the extent that the simulations given in Chapter 3 agree with the experimental data in Chapter 4, as well as the work of others in the field.

2.5.2: Time Invariant Photon Equations

We begin by assuming that the time it takes a photon to travel through a round trip of the laser cavity is short compared to the time scales of other processes that affect the speed of the laser. This is justified, at least to some extent, in a uniformly pumped laser where the speed of the biasing circuitry generally limits the device's temporal response. In this case, we can write, for photons travelling in the $+x$ direction

$$\frac{dS_m^+}{dx} = G_m(x)S_m^+(x) + Q_m(x) \tag{2.5.1}$$

where $G_m(x)$ is the optical gain or loss per unit cavity length, as described in Section 2.4,[a] and $Q_m(x)$ accounts for spontaneous emission. For the moment we leave $Q_m(x)$ as an unknown function, for which an expression will be derived in Section 2.5.4.[b] Basically, eq. (2.5.1) states that the rate of change of the photon concentration at any given point is the sum of the contributions from stimulated emission or absorption (the gain, G_m times the photon concentration, S_m^+) and spontaneous emission (Q_m). Note that eq. (2.5.1) does not attempt to take into account any photon scattering processes, or coupling between the energy in different optical modes of the laser.

Equation (2.5.1) is a first order, nonhomogeneous differential equation for S_m^+ in x. Using the integrating factor method,[40] the solution can be shown to be

$$S_m^+(x) = S_m^+(x_o)e^{\int_{x_o}^{x} G_m(x')dx'} + \int_{x_o}^{x} Q_m(x')e^{\int_{x'}^{x} G_m(x'')dx''}dx' \tag{2.5.2}$$

---

[a] Section 2.4 describes the function $G_m(n)$, but since any given point x has a single value of n associated with it, it is merely a matter of notation to write $G_m(n(x))$ as $G_m(x)$.

[b] Section 2.5.4 describes the function $Q_m(n)$, but, as explained for $G_m(x)$ above, it is equivalent to write $Q_m(n(x))$ as $Q_m(x)$.

where x' and x'' are dummy variables of integration. Equation (2.5.2) describes the photon concentration at x in terms of the photon concentration at some initial point x_o. The terms can be interpreted as follows: the first term on the right hand side contains the contribution of the initial photon concentration (moving in the $+x$ direction) at x_o, $S_m^+(x_o)$. This is multiplied by the gain integrated along the path the photon travels, from x_o to x. In a uniformly pumped laser, where the gain is usually assumed to be a constant, this term would simply be $S_m^+(x_o)e^{G_m L}$, where $L = x - x_o$. The second term on the right hand side of eq. (2.5.2) describes the contribution of spontaneous emission to $S_m^+(x)$: we integrate from x_o to x to account for all the spontaneous emission that occurs in this range. This integral includes the amount of light generated at each point, $Q_m(x')$, as well as the gain it experiences as it travels to point x. If we again consider the case of a uniformly pumped laser, this term simplifies to $LQ_m e^{G_m L}$.

Equation (2.5.2) is an explicit expression for $S_m^+(x)$, and could be evaluated if the value of the initial condition, $S_m^+(x_o)$, were known. In practice, in order to solve for the photon concentration we must do two things. First, we write an equation similar to eq. (2.5.2), for light travelling down the cavity in the $-x$ direction:

$$S_m^-(x) = S_m^-(x_o)e^{\int_x^{x_o} G_m(x')dx'} + \int_x^{x_o} Q_m(x')e^{\int_x^{x'} G_m(x'')dx''} dx' \qquad (2.5.3)$$

Second, we need to determine the boundary conditions that allow us to solve for $S_m^+(x_o)$ and $S_m^-(x_o)$. By considering reflections at the cavity facets we see that the appropriate boundary conditions for eqs. (2.5.2) and (2.5.3) are

$$S_m^+(0) = R_1 S_m^-(0) + S_{me}^+ \tag{2.5.4a}$$

and

$$S_m^-(L_T) = R_2 S_m^+(L_T) + S_{me}^- \tag{2.5.4b}$$

where 0 and L_T are the positions of the cavity facets, and R_1 and R_2 are the reflectivities at 0 and L_T, respectively. The terms S_{me}^+ and S_{me}^- represent the photon concentration injected into the active region of the laser through facets 1 and 2, respectively, in the mth cavity mode. The introduction of these terms allows us to simulate pumping of the laser optically as well as electrically.

Because in a real device there is the possibility of a partial reflection at the point where the guiding layer is etched away to electrically isolate the top contacts, we add the conditions

$$S_m^+(L_1) = R_i S_m^-(L_1) + T_i S_m^+(L_1) \tag{2.5.5a}$$

and

$$S_m^-(L_1) = R_i S_m^+(L_1) + T_i S_m^-(L_1) \tag{2.5.5b}$$

where L_1, R_i , and T_i are the interface position, reflectivity, and transmittivity. Similar conditions could be added for any other reflections that might occur along the length of the cavity.

In principle, the combination of eqs. (2.5.2), (2.5.3), (2.5.4), and (2.5.5) allows us to solve for $S_m^+(x)$ and $S_m^-(x)$, although this would have to be done numerically in most cases. This means that, given the carrier distribution in the active region, we can calculate the photon distribution both spatially and in terms of wavelength (denoted by the cavity mode number, m).

Before we waste too much time and effort going through the tedious mathematics to determine these solutions, however, there is a problem that should be faced. At the beginning of Section 2.5.1 we assumed that the propagation of light in the laser cavity was much faster than anything else that occurs in the device. This is normally true in the case of uniform pumping, where the carrier concentration is generally held to be a constant over the cavity length. In this case, absorption and emission of photons at a particular point in the cavity do not affect the local carrier concentration. For the case of non-uniform pumping, however, the distribution of the carriers in the active region is almost certainly non-uniform. Since the carrier concentration is strongly coupled to the photon concentration,[a] variations in $n(x)$ can occur in time intervals comparable to those for the changes in $S_m^+(x)$ and $S_m^-(x)$. It is these changes in $n(x)$ that cause the hysteresis and self-pulsations observed in split-contact lasers, so it is evident that, although mathematically correct, the expressions we have developed in Section 2.5.2 cannot accurately model the more interesting phenomena that can occur in a non-uniformly pumped laser. Since these are the very effects that we hope to simulate in this work, in Section 2.5.3 we extend our photon equations to include the effects of the finite speed of light in the cavity.

2.5.3: Time Variant Photon Equations

To extend the photon equations to properly include the time evolution of the photon distribution, we first rewrite eq. (2.5.2), for the case where $x - x_o = \Delta x$ is infinitesimally small:

---

[a] For every photon generated (absorbed) at a particular point in the cavity, the carrier concentration must decrease (increase) as electrons and holes are annihilated (generated). Mathematically, the coupling is represented by the last term in eq. (2.2.1) for dn/dt, which contains the photon concentrations, and by the presence of G_m and Q_m in eqs. (2.5.2) and (2.5.3) for the photon concentration.

$$S_m^+(x) = S_m^+(x-\Delta x)e^{\Delta x G_m(x-\Delta x)} + \Delta x Q_m(x) \tag{2.5.6}$$

Now, it is implicit in the notation of this equation that it takes no time for the light to travel from point $x - \Delta x$ to x. We can make this point explicit by rewriting eq. (2.5.6) as

$$S_m^+(t,x) = S_m^+(t,x-\Delta x)e^{\Delta x G_m(t,x-\Delta x)} + \Delta x Q_m(t,x) \tag{2.5.7}$$

The problem introduced by the finite speed of light can be seen in this formulation. If the photons in mode m are travelling with velocity v_m, then it must take an amount of time $\Delta t = \Delta x / v_m$ for the light to travel from $x - \Delta x$ to x. Obviously, eq. (2.5.7) must be changed to

$$S_m^+(t,x) = S_m^+(t-\Delta t,x-\Delta x)e^{\Delta x G_m(t-\Delta t,x-\Delta x)} + \Delta x Q_m(t,x) \tag{2.5.8}$$

to correct this inconsistency.

Although the change from eq. (2.5.7) to (2.5.8) may seem like a trivial one, it is of central importance. On a purely arithmetic level, we worked from eq. (2.5.2) to (2.5.7) by simplifying the integral and changing the notation slightly; nevertheless, we could always reverse the steps and work backward to regain eq. (2.5.2). Equation (2.5.8), however, has made the fundamental change from an equation in one variable (x) to two (t and x). We can no longer work backward and return eq. (2.5.8) to the integral form of eq. (2.5.2). In addition, it was only necessary to have a single value, $S_m^+(x_o)$, as an initial condition to solve eq. (2.5.2) for the function $S_m^+(x)$. With eq. (2.5.8), however, we see that in order to calculate $S_m^+(t, x)$ we need to know the values of $S_m^+(t - \Delta t, x)$ at all x as an initial condition. This adds a new level of complexity to the problem.

Now that we have resolved to working with our photon equations in this discrete form, we find it expedient to rewrite eq. (2.5.8) as

$$S_m^+(t,k\Delta x) = S_m^+(t-\Delta t,(k-1)\Delta x)e^{\Delta x G_m(t-\Delta t,(k-1)\Delta x)} + \Delta x Q_m(t,k\Delta x) \qquad (2.5.9)$$

where $x = k\,\Delta x$, and k is a positive integer.

Now, eq. (2.5.9) describes the propagation of light in the bulk portion of the cavity, but does not take into account reflections at the facets or contact interfaces. In Section 2.5.2 we accounted for these reflections by applying the appropriate boundary conditions to the solution of our differential equation. The discrete form of eq. (2.5.9) means that, instead of using boundary conditions such as eqs. (2.5.4) and (2.5.5), we can model reflections by explicitly putting them into the equation for $S_m^+(t,\,k\,\Delta x)$:

$$\begin{aligned} S_m^+(t,k\Delta x) &= R_1 S_m^-(t-\Delta t,\Delta x)e^{\Delta x G_m(t-\Delta t,\Delta x)} + \Delta x Q_m(t,0) + S_{me}^+(t) \qquad &, k = 0 \\ &= R_i S_m^-(t-\Delta t,(N_i+1)\Delta x)e^{\Delta x G_m(t-\Delta t,(N_i+1)\Delta x)} &, k = N_i \\ &\quad + T_i S_m^+(t-\Delta t,(N_i-1)\Delta x)e^{\Delta x G_m(t-\Delta t,(N_i-1)\Delta x)} + \Delta x Q_m(t,N_i\Delta x) & \\ &= S_m^+(t-\Delta t,(k-1)\Delta x)e^{\Delta x G_m(t-\Delta t,(k-1)\Delta x)} + \Delta x Q_m(t,k\Delta x) &, \text{for all other } k \end{aligned} \qquad (2.5.10)$$

where $N_i = L_l / \Delta x$ is the position of the interface between the top contacts. The first line of this equation takes care of the reflection at the first facet, the second covers the junction between the contacts, and the third, which is identical to eq. (2.5.9), describes the remainder of the active region where light propagates without reflections.

To model the light propagating in the opposite direction, we can similarly show that

$$S_m^-(t,k\Delta x) = R_2 S_m^+(t-\Delta t,(N_T-1)\Delta x)e^{\Delta x G_m(t-\Delta t,(N_T-1)\Delta x)} + \Delta x Q_m(t,N_T\Delta x) + S_{me}^-(t) \quad , k=0$$

$$= R_i S_m^+(t-\Delta t,(N_i-1)\Delta x)e^{\Delta x G_m(t-\Delta t,(N_i-1)\Delta x)} + T_i S_m^-(t-\Delta t,(N_i+1)\Delta x)e^{\Delta x G_m(t-\Delta t,(N_i+1)\Delta x)} + \Delta x Q_m(t,N_i\Delta x) \quad , k=N_i$$

$$= S_m^-(t-\Delta t,(k+1)\Delta x)e^{\Delta x G_m(t-\Delta t,(k+1)\Delta x)} + \Delta x Q_m(t,k\Delta x) \quad , \text{for all other } k$$

(2.5.11)

where $N_T = L_T/\Delta x$.

Equations (2.5.10) and (2.5.11) now allow us to calculate the photon concentrations in the cavity at time $t+\Delta t$, if we know $S_m^+(t, x)$, $S_m^-(t, x)$, $n(t, x)$, and $n(t+\Delta t, x)$. The numerical method used to combine these equations into a functional model, along with some results of the simulations resulting therefrom, are described in Chapter 3. However, before we proceed with the simulations, we must determine an expression for $Q_m(n)$, which is the only remaining unknown component of the photon equations.

2.5.4: The Spontaneous Emission Term, Q_m

Since we have already developed an expression for the radiative recombination rate contributing to spontaneous emission, $R_{sp}(n,\lambda)$, in Section 2.3.2, it is straightforward to convert this into the parameter Q_m used in eqs. (2.5.10) and (2.5.11). Q_m represents the number of spontaneously emitted photons coupled into the mth cavity mode per second per unit length, so that we can write

$$Q_m = \frac{\text{(total spon. em. rate into } m^{\text{th}} \text{ mode) (coupling factor) (active region area)}}{\text{(speed of light in the active region)}}$$

In terms of the parameters we have been working with, this can be rewritten as

$$Q_m(n) = \frac{\beta_m DW}{v_m} \int_{\lambda_m - \Delta\lambda_m/2}^{\lambda_m + \Delta\lambda_m/2} R_{sp}(n,\lambda)d\lambda \tag{2.5.12}$$

where λ_m is the wavelength at the centre of the cavity mode, $\Delta\lambda_m$ is the mode width, and β_m is the fraction of the spontaneous emission coupled into the mode.

We determine the factor β_m by considering the sphere of unity radius shown in Fig. 2.5.1. It is evident that a spontaneous emission event that occurs at the centre of the sphere has the same probability of travelling in any direction. We can therefore calculate the amount of light that is emitted within an angle θ of the x-axis by determining the enclosed surface area, A. The differential area dA is given by the expression $dA = 2\pi \sin\theta d\theta$, so that the area $A(\theta)$ is

$$A(\theta) = \int_0^\theta 2\pi \sin\theta d\theta = 2\pi(1-\cos\theta) \tag{2.5.13}$$

Geometrically, we see that the coupling factor is given by

$$\beta_m = \frac{A(\theta_c)}{A(\pi)} = \frac{1-\cos\theta_c}{2} \tag{2.5.14}$$

where θ_c is the critical angle for light totally internally reflected in the laser active region. Treating this waveguide as an idealized, two-dimensional, structure allows us to write[41] $\theta_c = \sin^{-1}(n_{i,c}/n_{i,a})$, where $n_{i,c}$ and $n_{i,a}$ are, respectively, the cladding and active region

indices of refraction. Although this is a simplistic approach that avoids many of the complicated geometrical and material properties of the laser structure, we have found it sufficient for the purposes of this work.

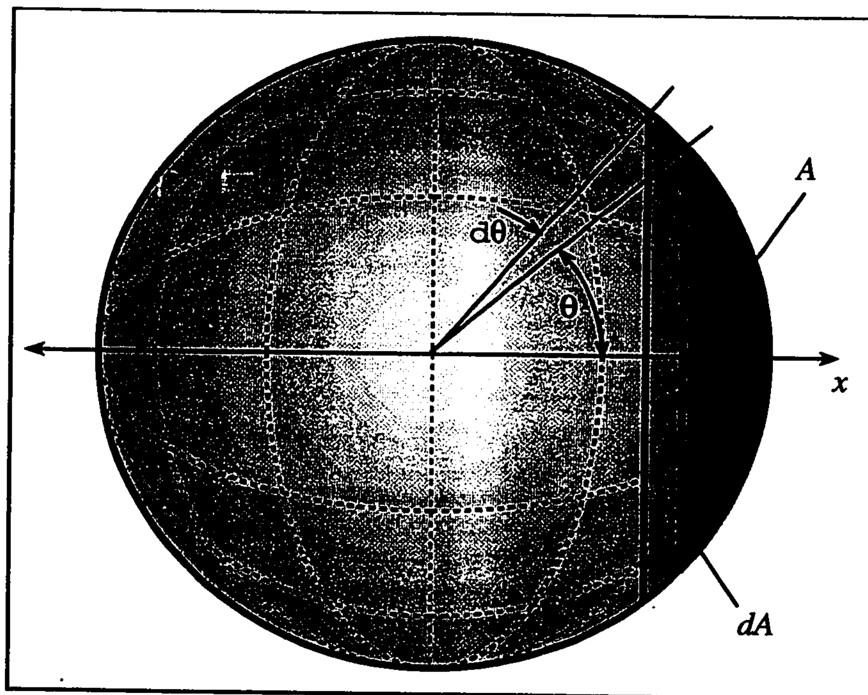

Figure 2.5.1: Surface Areas for the Coupling Factor, β_m
A sphere of unity radius in the active region of the laser. The probability of a photon generated by spontaneous emission at the centre of the sphere being emitted within an angle θ of the x-axis is given by the ratio of the area A to the total surface area of the sphere.

CHAPTER 2: REFERENCES

[1] Aristotle, Physics, Oxford, New York: Oxford University Press, 1996, p. 9

[2] Uenohara, H., Kawamra, Y., Iwamura, H., "Long-wavelength multiple-quantum-well voltage-controlled bistable laser diodes", *IEEE J. Quantum Electron.*, vol. 31, pp. 2142-2147, 1995

[3] Hui, R., "Static and dynamical properties of dispersive optical bistablity in semiconductor lasers", *J. Lightwave Technol.*, vol. 13, pp. 42-48, 1995

[4] Zhou, J., Cada, M., Li, G.P., and Makino, T., "Bistable characteristics and all-optical set-reset operations of 1.55-μm two-segment strained multiquantum-well DFB lasers", *IEEE Phot. Technol. Lett.*, vol. 7, pp. 1125-1127, 1995

[5] Hörer, J., Weich, K., Möhrle, M., and Sartorius, B., "Optimization of the optical switching characteristics of two-section Fabry-Perot lasers", *IEEE Phot. Technol. Lett.*, vol. 5, pp. 1273-1276, 1993

[6] Li, J., and Wang, Q., "A common-cavity two-section InGaAsP/InP bistable laser with a low optical switching power", *Opt. Commun.*, vol. 83, pp. 71-75, 1991

[7] Uenohara, H., Iwamura, H., and Naganuma, M., "Switching characteristics of InGaAs/InP multiquantum well voltage-controlled bistable laser diodes", *Jpn. J. Appl. Phys.*, vol. 29, pp. L2442-L2444, 1990

[8] Phelan, P., McDonald, D., Egan, A., Hegarty, J., O'Dowd, R., Farrell, G., and Lindgren, S., "Comparison of self-pulsation in multisection lasers with distributed feedback and intracavity saturable absorbers", *IEE Proc.-Optoelectron.*, vol. 141, pp. 114-118, 1994

[9] Marcenac, D.D. and Carroll, J.E., "Distinction between multimoded and singlemoded self-pulsations in DFB lasers", *Electron. Lett.*, vol. 30, pp. 1137-1138, 1994

[10] Barnsley, P., "All-optical clock extraction using two-contact devices", *IEE Proc. J*, vol. 140, pp. 325-336, 1993

[11] Farrell, G., Phelan, P., Hegarty, J., and Shields, J., "All-optical timing extraction with frequency division using a twin-section laser diode", *IEEE Photon. Technol. Lett.*, vol. 5, pp., 718-721, 1993

[12] Simler, Y., Gamelin, J., and Wang, S., "Pulsation stablilization and enhancement in self-pulsing laser diodes", *IEEE Photon. Technol. Lett.*, vol. 4, pp. 329-332, 1992

[13] Zhang, L., and Cartledge, J.C., "Fast wavelength switching of three-section DBR lasers", *IEEE J. Quantum. Electron.*, vol. 31, pp. 75-81, 1995

[14] Eddolls, D.V., Vass, S.J., Ash, R.M., and Park, C.A., "Two-segment multiquantum well lasers with 7 nm tuning range and narrow linewidth", *Electron. Lett.*, vol. 28, pp. 1057-1058, 1992

[15] Chang-Hasnain, C.J., Harbison, J.P., Zah, C.E., Florez, L.T., and Andreadakis, N.C., "Two-electrode vertical cavity surface emitting lasers", *Electron. Lett.*, vol. 27, pp. 1002-1003, 1991

[16] Chen, J., Wu, Z., Xia, G., and Lu, Y., "Simple equations used to study the wavelengths of two-segment bistable laser diodes", *Opt. Lett.*, vol. 20, pp. 1298-1300, 1995

[17] Griffel, G., Lang, R.J., and Yariv, A., "Two-section gain-levered tunable distributed feedback laser with active tuning section", *IEEE J. Quantum Electron.*, vol. 30, pp. 15-18, 1994

[18] Mitchell, N.F., O'Gorman, J., and Hegarty, J., "Optical bistability in asymetric Fabry-Perot laser-diode amplifiers", *Optics Lett.*, vol. 19, pp. 269-271, 1994

[19] Paradisi, A. and Montrosset, I., "Analysis of wavelength conversion using a multisection DBR laser with a saturable absorber", *IEEE J. Quantum Electron.*, vol. 29, pp. 1285-1294, 1993

[20] Middlemast, I., Sarma, J., Shore, K.A., Kurcharska, A.I., Fletcher, E.D., and Blood, P., "Absorptive bistability in inhomogeneously pumped quantum well laser diodes", *IEE Proc.-J*, vol. 138, pp. 301-308, 1991

[21] O'Dowd, R.F. and Davis, M.G., "Theoretical study of a two-section single-cavity semiconductor laser for use as a wavelength-tunable source", *Opt. Quantum Electron.*, vol. 20, pp. 383-393, 1988

[22] Chen, J., et al., 1995, op. cit.

[23] Duan, G.-H., Landis, P., and Jacquet, J., "Modeling and measurement of bistable semiconductor lasers", *IEEE J. Quantum Electron.*, vol. 30, pp. 2507-2515, 1994

[24] Ottolenghi, P., Benedetto, S., and Montrosset, I., "Switching and optical modulation of three-section DBR lasers", *IEEE J. Quantum Electron.*, vol. 30, pp. 1381-1388, 1994

[25] Lee, C.-H., Shin, S.-Y., and Kang, S.-G., "Perturbation solution of self-pulsing in semiconductor lasers with a saturable absorber", *IEEE J. Quantum Electron.*, vol. 30, pp. 1396-1404, 1994

[26] Bandelow, U., Wünsche, H.J., and Wenzel, H., "Theory of selfpulsations in two-section DFB lasers", *IEEE Photon. Technol. Lett.*, vol. 5, pp. 1176-1179, 1993

[27] Paradisi, A. and Montrosset, I., "Numerical modeling of bistable laser diodes with saturable absorbers", *IEEE J. Quantum Electron.*, vol. 27, pp. 817-823, 1991

[28] Baoxun, D., "A theory on stability of double-section semiconductor lasers", *IEEE J. Quantum Electron.*, vol. 25, pp. 847-849, 1989

[29] Lasher, G.J., "Analysis of a proposed bistable injection laser", *Solid-St. Electron.*, vol. 7, pp. 707-716, 1964

[30] Zhang, L., et al., 1995, op. cit.

[31] Kikuchi, K. and Tomofuji, H., "Analysis of oscillation characteristics of separated-electrode DFB laser diodes", *IEEE J. Quantum Electron.*, vol. 26, pp. 1717-1727, 1990

[32] Verdeyen, Joseph Thomas, Laser Electronics, Second Edition, Englewood Cliffs, New Jersey: Prentice Hall, 1989, Section 11.4.2

[33] ibid, p. 155, eq. (7.2.10)

[34] ibid, p. 377, eq. (11.4.12a)

[35] ibid, p. 376, eq. (11.4.5)

[36] ibid, p. 379, eqs. (11.4.15b) and (11.4.15c).

[37] Properties of Indium Phosphide, INSPEC, The Institute of Electrical Engineers, London & New York, 1991, pp. 425R2-426R2

[38] Verdeyen, J.T., op. cit., page 379

[39] Yang, Edward S., Microelectronic Devices, Toronto, Ont.: McGraw-Hill Inc., 1988, pp. 17-19

[40] O'Neil, Peter V., Advanced Engineering Mathematics, Belmont, California: Wadsworth Publishing Co., 1983, Section 1.5

[41] Hecht, Eugene, Optics, Second Edition, Don Mills, Ont.: Addison-Wesley Publishing Company, Inc., 1987, p. 104, eq. (4.69)

CHAPTER 3: LASER SIMULATIONS

That which agrees with the formal conditions (intuition and conception) of experience, is *possible.*

Immanuel Kant, *Critique of Pure Reason*[1]

3.1: INTRODUCTION

In Chapter 2 we developed the model we use to describe split-contact semiconductor lasers with non-uniform pumping. Within the limits of our approximations the model appears to be conceptually accurate, but as it stands it consists merely of a set of abstract, mathematical equations. Although some might find these informative as they stand, it is clearly also important to actually *solve* the equations under specific conditions, to determine what types of laser behaviour the theory predicts to be possible. In this chapter we therefore present a series of laser simulations generated by numerical solution of the equations developed in the previous chapter. However, before plunging directly into the simulation results, it would seem worthwhile to say a few words about the manner in which they have been generated.

3.2: THE NUMERICAL METHOD

3.2.1: The Solution Algorithm

The general goal of these computations is to be able to determine the carrier and photon concentrations, $n(t,x)$, $S_m^+(t,x)$ and $S_m^-(t,x)$, under the bias conditions of interest. Equations (2.2.1), (2.5.10), and (2.5.11) constitute three coupled equations that can be solved simultaneously for these three variables. In order to remain consistent with the

notation of Section 2.5.3, in which we expressed the differential photon equations in a discretized form, we now reformulate eq. (2.2.1) in a similar manner:[a]

$$n(t,k\Delta x) = n(t-\Delta t,k\Delta x) + \left\{ \begin{array}{l} \dfrac{J(t-\Delta t,k\Delta x)}{qD} - R_r(n(t-\Delta t,x)) \\ -\sum_{m=1}^{M} G_m(n(t-\Delta t,k\Delta x))\left[S_m^+(t-\Delta t,k\Delta x)+S_m^-(t-\Delta t,k\Delta x)\right]\dfrac{v_m}{DW} \end{array} \right\} \Delta t \tag{3.2.1}$$

The numerical technique used to solve eqs. (3.2.1), (2.5.10), and (2.5.11) is the Euler method. That is, given some known initial solution to the equations, $n(t_o,x)$, $S_m^+(t_o,x)$ and $S_m^-(t_o,x)$, we use eq. (3.2.1) to calculate $n(t_o+\Delta t,x)$, the carrier concentration at a slightly later time. Once this function has been determined, it can be used in eqs. (2.5.10) and (2.5.11) to solve for $S_m^+(t_o+\Delta t,x)$ and $S_m^-(t_o+\Delta t,x)$. Given the conditions at t_o, we are thus able to characterize the laser at $t_o+\Delta t$, and, by repeating the process iteratively, at any later time t.

Of course, before this process can be begun, we need to somehow determine the initial condition $n(t_o,x)$.[b] This is achieved by considering the "trivial" solution that occurs when the device is in equilibrium. When the laser is unbiased there is no mechanism for excess carrier generation, and the carrier concentration is simply equal to its equilibrium value. Basic carrier statistics show that this is given by[2]

---

[a] Note that in going from eq. (2.2.1) to (3.2.1) we have dropped the longitudinal carrier diffusion term. Although this term may be significant under some conditions, it tends to cause difficulties in the numerical solution of the equations, and has therefore been omitted in the simulations presented here.

[b] Given $n(t_o,x)$ we can calculate $S_m^+(t_o,x)$ and $S_m^-(t_o,x)$ from eqs. (2.5.10) and (2.5.11), so in practice we only need to find the carrier concentration profile to define our intital condition.

$$n_o = \sqrt{N_c N_v} e^{-E_g/2kT} \quad (3.2.2)$$

for an undoped active region.

The method outlined here allows us to characterize the laser under whatever arbitrary bias conditions are of interest. The electrical bias is defined by the function chosen for $J(t,x)$, which appears in eq. (3.2.1). In the simulations presented in this work, we generally consider $J(x)$ to be piecewise constant, in order to represent the split-contact geometry depicted in Fig. 2.1.1. Optical pumping of the laser is simulated by choosing the appropriate functions for $S^{+}_{me}(t)$ and $S^{-}_{me}(t)$ in eqs. (2.5.10) and (2.5.11). Each simulation provides us with the temporal response of the laser to the chosen bias conditions, so that we can generate information regarding not only the steady-state output of the laser under constant bias, but also about the evolution of the laser parameters due to changes in the applied bias. The determination of this temporal response is, of course, essential to the proper understanding of the self-pulsations and optical hysteresis that are observed in non-uniformly pumped lasers.

3.2.2: Some Computational Considerations

In order to carry out the actual calculations needed to generate the simulations described above, a Microsoft QuickBasic program was written. Unless otherwise specified, the values for the various constants (e.g. band gap, laser dimensions) are as listed in the Glossary in Appendix D. In order to characterize continuous variables such as space, time and wavelength, the program divides these dimensions into discrete partitions for the numerical computations. The relationship between the separation of points in space and time is $\Delta t = \Delta x / v_m$, as described in Section 2.5.3. Because of finite time it takes the computer to do each calculation, this serves to limit the resolution with which the

simulations can be performed. A high spatial resolution (small Δx) requires a small time increment, Δt, which in turn increases the amount of computer time needed to simulate a given amount of "laser time".

Because the model described in Chapter 2 does not include any information about the phase of light in the laser cavity, it cannot be used to generate the cavity mode structure. We have therefore arbitrarily imposed the mode structure illustrated in Fig. 3.2.1 on our model, to give an approximate picture of the laser spectra.

For $m \leq 9$, each wavelength λ_m in Fig. 3.2.1 represents the centre of a mode of the Fabry-Perot laser cavity. From simple phase matching criteria, the mode spacing, $\Delta\lambda_m$, can be shown to be given by

$$\Delta\lambda_m = \frac{\lambda_m^2}{2n_r L_T + \lambda_m} \tag{3.2.3}$$

Although this approach is not rigorous (the assumption that the 0th mode is centred $\Delta\lambda_0/2$ from the band edge is arbitrary, and we do not account for the change in the cavity index of refraction caused by varying carrier concentration), it does allow us to simulate laser spectra using the model developed in this work. The approximations mean that our spectral predictions are not to be considered quantitatively accurate, but hopefully are capable of illustrating the more interesting trends observed in non-uniformly pumped lasers.

In the simulations that follow we consider only the first 10 cavity modes of the laser. As the simulations show, this is sufficient to account for all modes in which there is a significant amount of optical power above threshold. However, it only covers a relatively

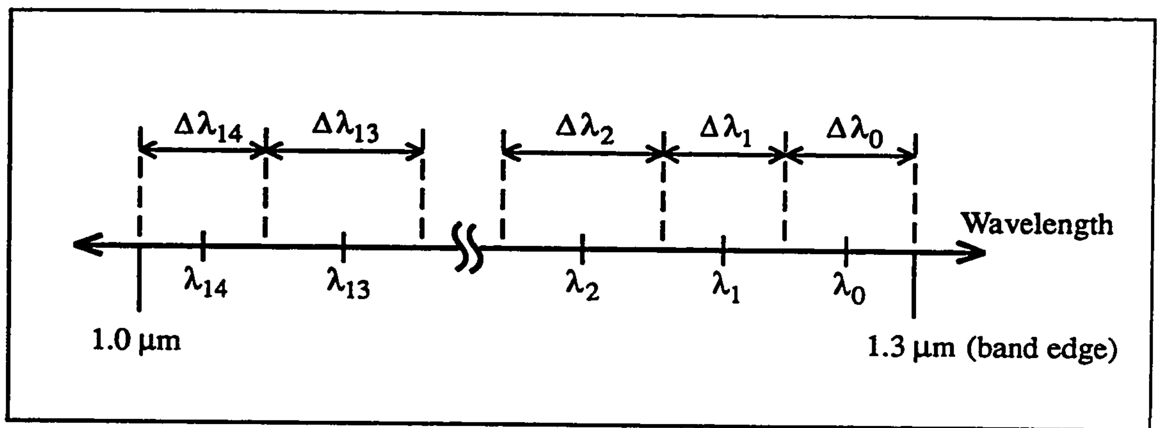

Figure 3.2.1: Laser Mode Structure
For simulation purposes, the laser modes are assumed to be centred at the wavelengths λ_m. For $m \leq 9$, the mode width, $\Delta\lambda_m$, corresponds to the free spectral range of the laser, given by eq. (3.2.3). For $m > 9$ the width is described in the text, below.

small wavelength range (typically on the order of 50 Å, depending on the length of the laser) compared to the spectral width of the spontaneous emission (see Fig. 2.3.1). For this reason we also include λ_{10} through λ_{14}, with separation $\lambda_{m>9} \sim 600$ Å. These cover the wavelength range from the edge of the highest cavity mode ($m = 9$) to $\lambda = 1.0\ \mu$m, although with a much coarser wavelength resolution than is used near the band edge. This has been done, not with a view to any accurate simulation of the spectral mode structure at these shorter wavelengths, but simply to give a more realistic description of the total amount of spontaneous emission generated in the laser.

Finally, we assume that the spontaneous emission rate and the gain/absorption do not vary significantly over the width of each mode. Calculations are only performed at the discrete values of λ_m, and these are assumed to represent the average for the mode. This means that the integration in eq. (2.5.12) over the width of the cavity mode reduces to $R_{sp}(n, \lambda_m)\,\Delta\lambda$ in our numerical analysis.

3.3: A Uniformly Pumped Laser Simulation

3.3.1: Motivation

In order to make our simulations of split-contact lasers more meaningful, we first present some results for the case where carrier injection into the active region of the laser is uniform. This corresponds to the case of a "normal" laser, for which the top and bottom contacts are continuous. We present the uniformly pumped simulations primarily for comparison purposes: since the characteristics of this type of laser have been more thoroughly studied, and are (relatively) simple compared to the non-uniformly pumped case, they serve to illustrate the capabilities of our model. This section serves as a basis with which to compare the non-uniform simulations that follow; in cases where the model is not quantitatively accurate, it can still be useful in predicting how the non-uniformly pumped laser compares to the traditional contact configuration.

3.3.2: The Time-Dependent Simulation

We refer to Fig. 2.1.1 for a schematic of the device simulated in this section, except that the two top contacts are electrically shorted together so that the device current is $I_{tot} = I_1 + I_2$, and the current density is uniform. The relevant lengths are given in

Symbol	Value	Description
L_1	250 μm	contact #1 length
L_2	250 μm	contact #2 length
L_T	500 μm	total cavity length
Δx	50 μm	step size for numerical solution

Table 3.3.1: Geometric Terms for the Device Simulation

Table 3.3.1; the other model parameters (i.e. the general values that are used in all the simulations) are given in the Glossary in Appendix D. Note that throughout this chapter we assume that the distance separating the top contacts is negligible.

To generate the simulations that follow, we begin with the device under zero bias at time $t = 0$. The total bias current, I_{tot}, is then incremented by 1 mA every 100 ns, up to $I_{tot} = 50$ mA. The resulting staircase-like bias function shown in Fig. 3.3.1, along with a log plot of the corresponding simulated optical output. The value of 100 ns for the time increment was chosen to allow the device to reach steady state after each change in the current, while keeping the total time calculated to a minimum. Also shown in Fig. 3.3.1 is

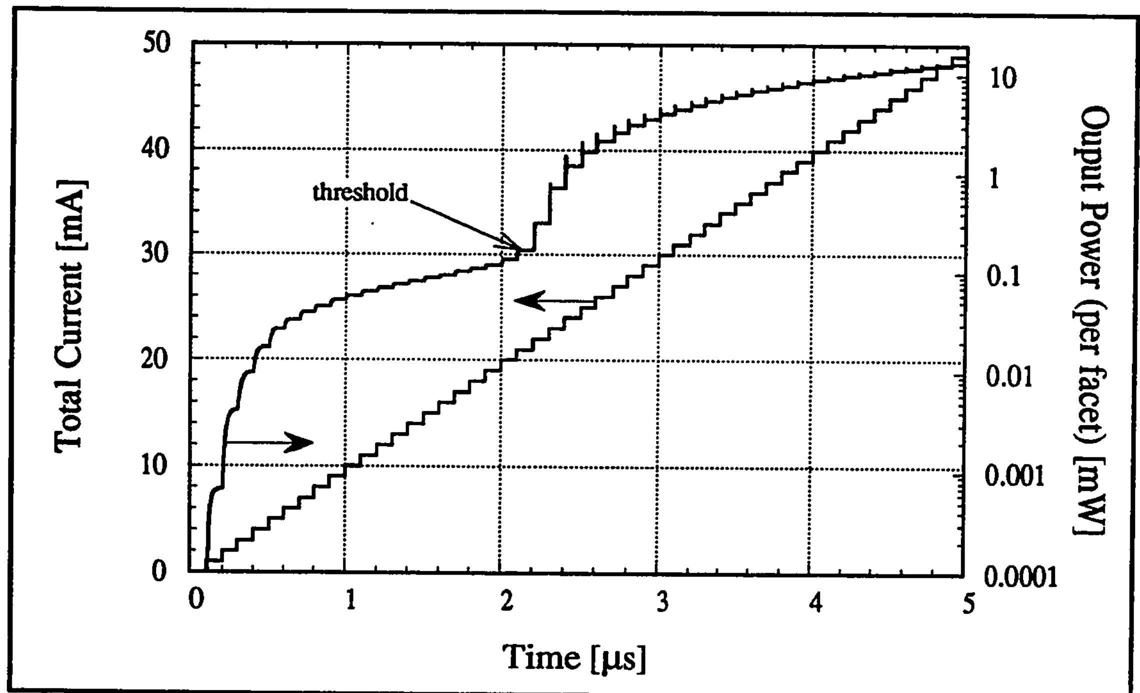

Figure 3.3.1: Current and Optical Output vs. Time
The light output vs. time for a uniformly biased laser simulation is plotted, along with the bias current driving the device. Threshold is reached at approximately 2.3 μs, where $I_{tot} = 22$ mA.

the evolution of the optical output as a function of time, given the bias conditions illustrated. We see that the optical power varies by more than four orders of magnitude, from hundreds of nanowatts at low biases to tens of milliwatts at high currents. The lasing threshold here occurs at $I_{th} = 22$ mA; below this bias the device emits primarily spontaneous light, whereas above I_{th} stimulated emission becomes significant, and the output power level is much higher.

In addition to the obvious difference in the magnitude of the optical output of the simulation above and below threshold, Fig. 3.3.1 also indicates a change in the temporal response of the laser. To illustrate this difference in more detail, we have plotted two sections of the optical output curve on an expanded scale in Fig. 3.3.2.

It is evident from Fig. 3.3.2 that the optical response of the laser is much faster above threshold than below. Settling times of 10 to 100 ns are required below threshold for the output of the device to stabilize, as compared to less than 5 ns when biased above I_{th}. This difference in speed is due to the fact that the dominant photon generation mechanisms above and below threshold are different. Below I_{th} the majority of the light is produced through spontaneous emission, which is a relatively slow process limited by the statistical radiative decay of electron-hole pairs. For $I > I_{th}$, photons are generated primarily via the much faster process of stimulated emission.

A related effect that is observed in Fig. 3.3.2 is the prediction of a monotonic change in the optical level when the bias is incremented below I_{th}, whereas relaxation oscillations are observed when in the lasing regime. These oscillations are a consequence of the fact that initially the current injection increases the carrier concentration in the cavity faster than stimulated emission reduces it: the excess carriers produce a gain increase that causes the photon concentration to overshoot its steady state value. This effect eventually

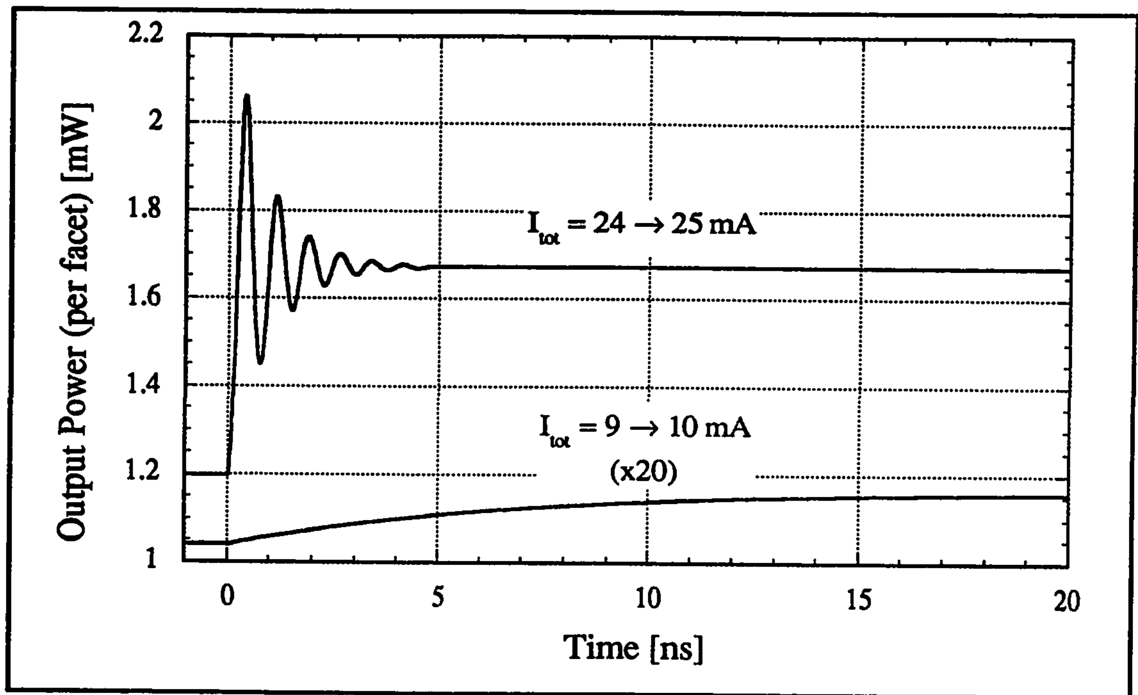

Figure 3.3.2: Optical Response to a Change in Bias Current

The optical response of the simulation to a step function change in the bias current is plotted. The current, I_{tot}, changes from 24 to 25 mA at $t = 0$ for the upper curve, and from 9 to 10 mA for the lower one. The output power has been magnified by a factor of 20 for the lower curve for illustrative purposes.

reverses because the increased photon density depopulates the carriers through stimulated emission, reducing the gain and, consequently, allowing the optical flux to drop. These oscillations are not observed below threshold because in this case the material is absorbing instead of amplifying, so that an increase in the photon flux does not depopulate the carrier density. For the parameters used in this simulation, the relaxation oscillation frequency varied from 1.3 GHz at $I_{tot} = 23$ mA to 4.7 GHz at 60 mA. These results are in line with observations of relaxation oscillations measured in actual lasers,[3,4] as well the predictions of less complicated models.[5] The ability of our model to reproduce this

oscillatory behaviour is significant, as it is closely related to the self-pulsations that occur in some of the non-uniformly biased cases.

3.3.3: The Steady-state Characteristics

We extract the steady-state operating characteristics of the laser from Fig. 3.3.1 by taking the level that the output approaches at the end of each current step. Figure 3.3.3 shows the steady-state optical output and carrier concentration (averaged over the length of the cavity) as a function of bias current; both of these are in agreement with what we expect from a uniformly biased laser.

The *L-I* characteristic in Fig. 3.3.3 consists of a region of low light emission, from $I_{tot} = 0$ to the lasing threshold at $I_{th} = 22$ mA, followed (as the bias increases) by a lasing region in which the optical output increases linearly with current injection. The above threshold differential efficiency of the simulation is about 96%, which is considerably greater than what is generally observed experimentally in semiconductor lasers.[a] However, this is to be expected from our model, because we do not account for effects such as scattering of light out of the laser mode, absorption due to defects or in the laser cladding or contacts, or carrier leakage out of the active region. We consider only such losses as non-radiative recombination and band-to-band absorption, which, being functions of the carrier concentration, are approximately constant above threshold. It is therefore not unexpected that the differential efficiency of our simulations should approach unity for $I_{tot} > I_{th}$.

Although one cannot directly measure the carrier concentration in a laser cavity, the $\bar{n}$-*I* curve in Fig. 3.3.3 seems reasonable in light of basic laser theory. Below threshold, the average carrier density increases with bias current in a slightly sub-linear fashion.

---

[a] The external differential quantum efficiency of the lasers discussed in Chapter 4 was typically 20 to 30% when biased uniformly.

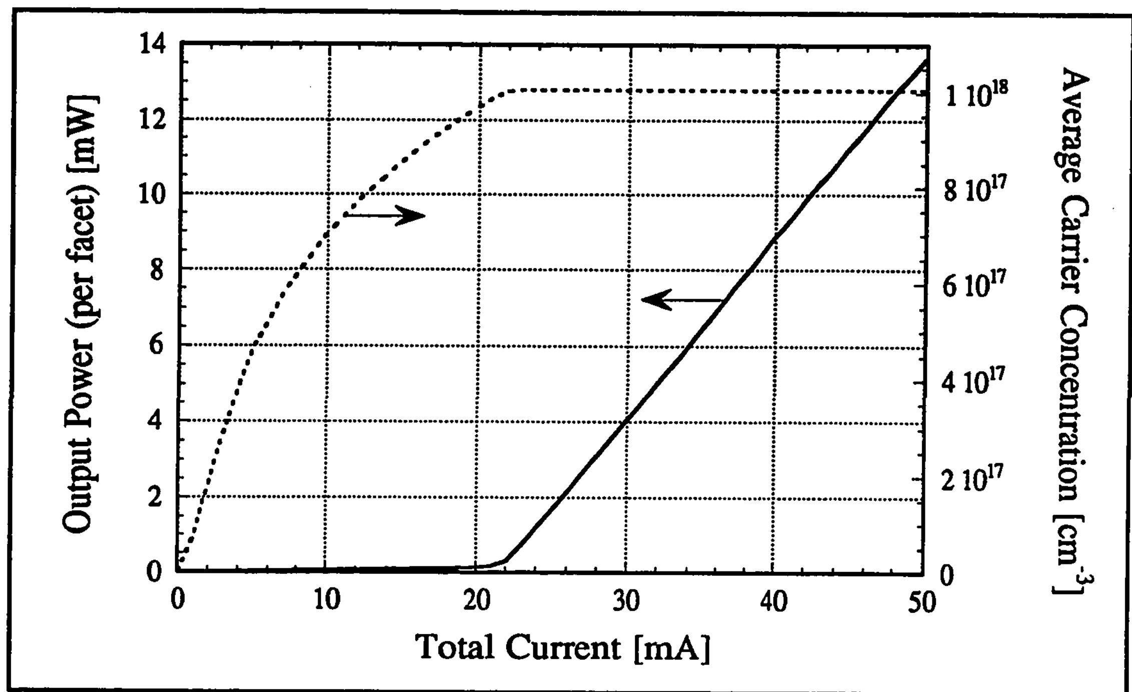

Figure 3.3.3: Steady-state Uniformly Biased Laser Characteristics
The optical output power per facet (solid line) and carrier concentration averaged over the cavity length ($\bar{n}$, broken line) are plotted vs. the laser bias current.

Above threshold the value of $\bar{n}$ is fixed at a constant value (to within 5×10^{14} cm^{-3}), corresponding to the level at which the cavity gain and losses are balanced.

3.3.4: The Spectral Characteristics

In addition to calculating the total amount of power generated in the laser as a function of bias, our model also allows us to simulate the spectral output of the laser at each bias point. Although the nature of our wavelength discretization does not allow a quantitatively accurate simulation of the spectra at biases significantly below threshold (see Section 3.2.2), we are able to generate useful spectral information close to and above threshold. Figure 3.3.4 illustrates the spectral output of our non-uniformly pumped laser,

for biases at which a significant portion of the output power is at wavelengths close to the band edge.

Remembering that the lasing threshold is 22 mA for this simulation, we now attempt to explain the spectra in Fig. 3.3.4. Below threshold we see that very little of the output power is emitted near the band edge, into modes #0 through #9. This is because the light emitted below threshold is primarily due to spontaneous emission, for which the peak emission wavelength is at least 20 nm from the band edge (see Fig. 2.3.1). As the current is increased through threshold, we find that the optical power becomes more and more concentrated within the first few mode spacings of the band edge (specifically modes #0-9

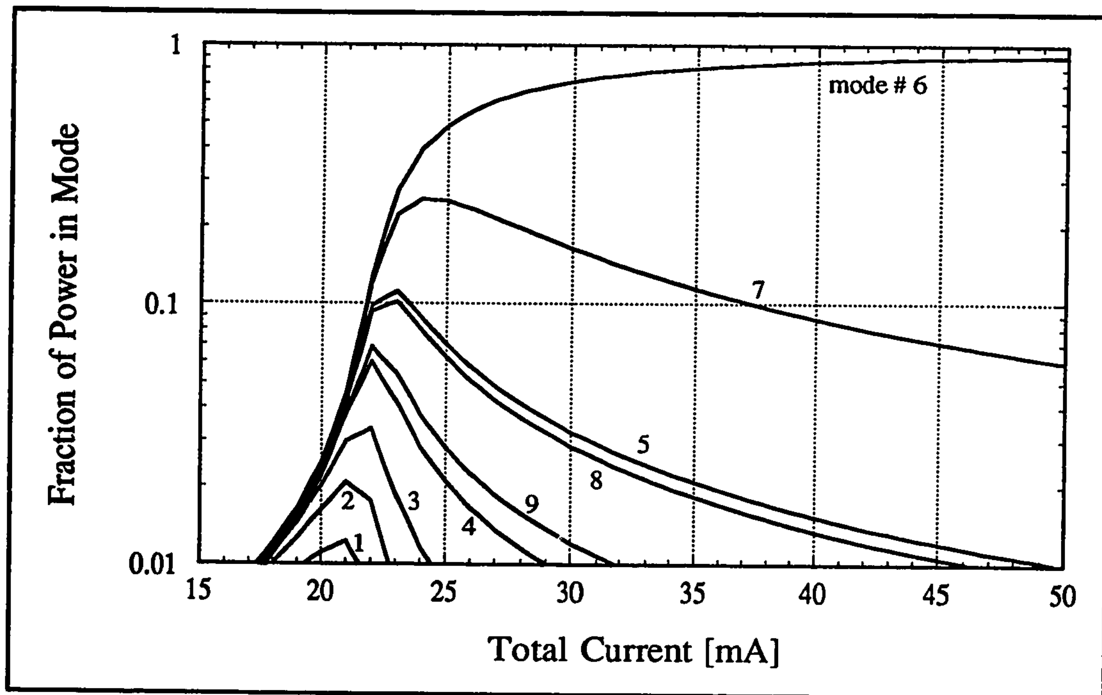

Figure 3.3.4: Steady-state Uniformly Biased Laser Spectra
The fraction of the total output power that is emitted into each cavity mode (i.e. with $\Delta\lambda_m/2$ of λ_m, see Fig. 3.2.1) is plotted vs. the laser bias current. Only the 10 lowest energy modes are plotted, covering a wavelength range of ~5 nm.

for this simulation). The fact that above threshold the gain is positive near the band edge (see Fig. 2.4.1) allows amplification of the small amount of spontaneous emission occurring in this spectral region, which shifts the emission peak toward the band edge.

At bias currents slightly greater than threshold, Fig. 3.3.4 indicates that the laser is operating multi-mode. For example, at $I_{tot} = 24$ mA, the strongest mode is #6, with 39% of the total power, while 25% is in mode #7, 9% in #5, and 8% in #8. However, as the bias current is increased further, the spectrum becomes increasingly single mode; the power in mode #6 rises linearly with current, while the power in the other modes saturates. This trend of becoming more single mode as the bias increases is commonly observed experimentally when heating effects are negligible (for example, see Section 4.6.2).

The fact that it is mode #6 that eventually dominates the lasing spectra is due to a combination of factors. One generally expects the device to lase at the wavelength with the greatest gain, determined by the above-threshold saturated carrier concentration. For a value of $\bar{n} \sim 10^{18}$ cm^{-3}, Fig. 2.4.1 indicates this to occur 1 to 4 nm below the band-gap wavelength (a range that includes mode #6 in this simulation). The specific wavelength at which the gain peak saturates generally depends on the various contributions to optical gain and loss in the cavity. The facet reflectivities, cavity length, and contact bias configuration (for the cases where the laser is not uniformly biased) all affect the lasing mode of the device, because each contributes to the net round-trip gain of the laser cavity. As we will see when we proceed to simulations of other device configurations, the dominant laser mode changes with these parameters.

The final point of interest in Fig. 3.3.4 is the fact that there is no indication of mode hopping in this simulation. Although the model used here does not include wavelength tuning due to heating or changes in refractive index, it is still able to simulate

shifts in the lasing mode caused by changes in the gain spectrum of the laser. In Fig. 3.3.4 we observe a transition from multi- to single-mode behaviour, but above threshold the strongest mode is always #6. This indicates that, for the case of uniform pumping, the position of the gain peak does not vary by more than a few tenths of an Angstrom with bias currents above threshold. This contrasts with the non-uniformly biased simulations described in Section 3.4.2, below, which do predict that mode hopping can be observed under some conditions.

3.3.5: The Effects of the Longitudinal Carrier Distribution

Less detailed models of semiconductor lasers generally assume that under a continuous electrical contact the carrier concentration is uniform;[6-10] however, as Fig. 3.3.5 illustrates, our more comprehensive analysis shows that this is not, strictly speaking, the case. Although the carrier *injection* in this simulation is uniform along the laser axis, the carrier *concentration* in the cavity does vary to a small extent with the position in the laser. The simulation indicates that the variation in $n(x)$ is smallest closest to threshold ($\Delta n/\bar{n} \sim 0.2\%$ just above I_{th}) and increases with bias (reaching ~1% at 40 mA above I_{th}).

Although this may seem like a small variation, it is significant. The value of $\bar{n}$ (the carrier concentration averaged over the laser length) is 1.00673×10^{18} cm^{-3} at $I_{tot} = 30$ mA and 1.00664×10^{18} cm^{-3} at 60 mA, a variation of less than 0.01%. The variation in the carrier density *along the laser* at a fixed bias is therefore considerably greater than the variation in the *average carrier density* with the bias current above threshold. In fact, we find that the average carrier concentration in the cavity actually *decreases* slightly as the current increases from 30 to 60 mA. Since the optical output of the laser increases significantly between these biases (see Fig. 3.3.3), the net gain of the cavity must be rising

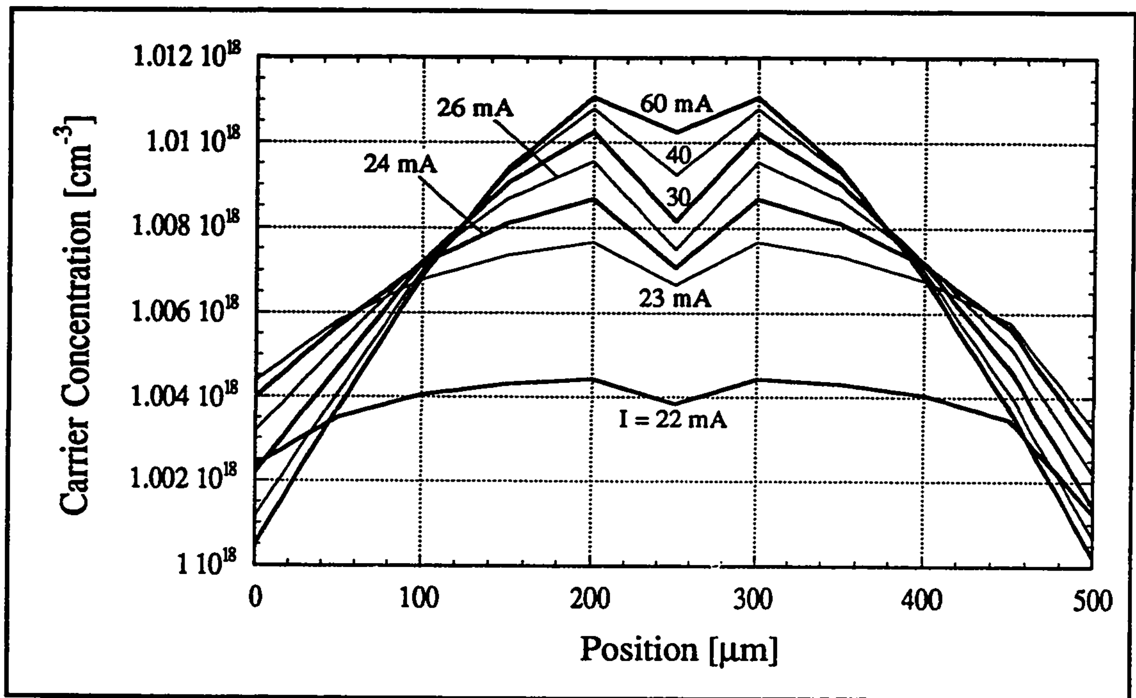

Figure 3.3.5: Carrier Concentration vs. Position in the Laser Cavity

The simulated carrier concentration is plotted vs. longitudinal position in the laser cavity, for a series of bias currents. Lasing threshold is at ~22 mA for this simulation.

over this range. Therefore, we can conclude that the increase in the output power of the laser in this range is primarily due to the redistribution of the carriers inside the cavity, rather than to an increase in the total number of carriers present.

To investigate the effects of the longitudinal variation of the carrier density in more detail, we have done the following. Our time-dependent simulation of the uniformly pumped laser gave us the spectral output of the laser at $I_{tot} = 60$ mA, as well as the steady-state carrier density profile shown in Fig. 3.3.5. From this carrier profile we calculate the average carrier density in the cavity, $\bar{n}$. Then, using eqs. (2.5.10) and (2.5.11), we simulate what the optical output of the laser would be, if the carrier density was a constant value (i.e. $\bar{n}$) along the cavity length, instead of having the profile in

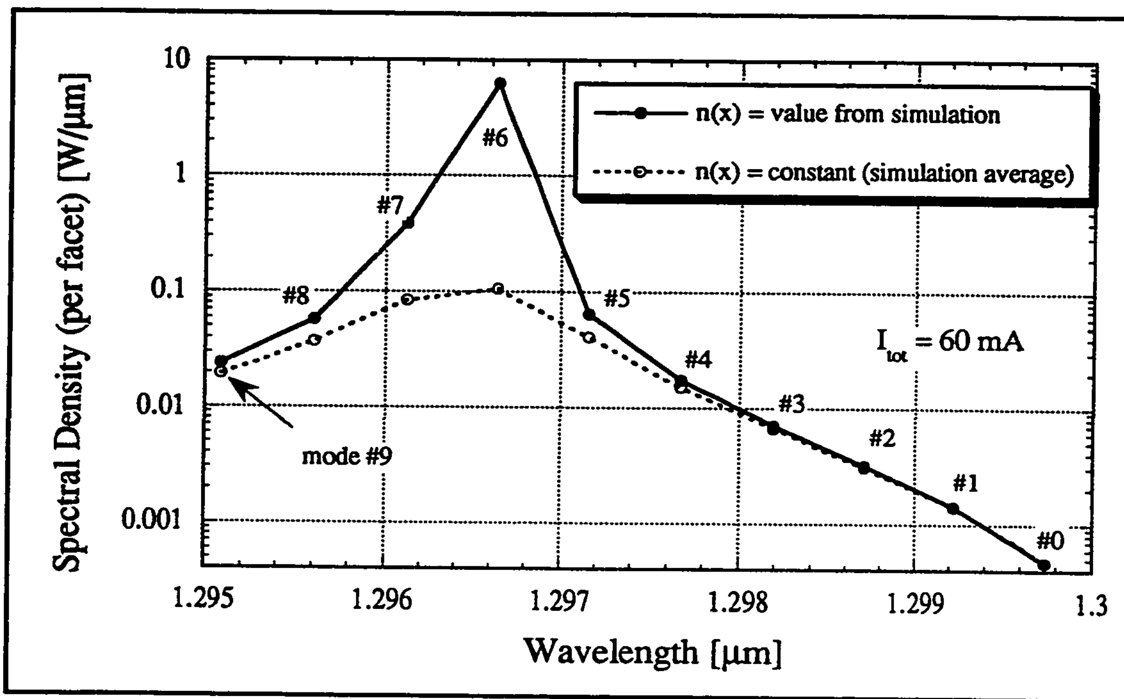

Figure 3.3.6: Spectra Using Varying and Constant Carrier Profiles

The spectral output generated from the complete, time-dependent simulation of the uniformly pumped laser (solid curve) is compared with the spectra found by assuming that the carrier density is constant over the device length (broken curve). The value taken for this constant carrier density is the average value from the simulated profile.

Fig. 3.3.5.[a] The resulting spectra are compared in Fig. 3.3.6.

Figure 3.3.6 illustrates the significant difference that a variation of only 1% in the carrier concentration can have on the optical output of the simulation. For both curves the total number of carriers in the cavity is the same, it is only the way in which they are distributed that differs. The curves approach each other for modes far from the lasing

[a] The steady-state values of S_m^+ and S_m^- are calculated by assuming that $S_m^+(t,x) = S_m^+(t - \Delta t, x)$, $S_m^-(t,x) = S_m^-(t - \Delta t, x)$, and $G_m(t,x) = G_m(t - \Delta t, x)$. Although this approach is not necessarily self-consistant to the extent that our general model is, it does give the proper results for an (arbirary) assumed carrier profile. Since we have assumed in this case that the carrier density is constant along the laser, the results can reasonably be compared with the time-dependent simulation.

wavelength, but the difference in power at the peak wavelength (mode #6) is nearly two orders of magnitude. This shows that even when the carrier injection is uniform, it can be important to calculate the carrier density profile in the active region self-consistently, instead of simply assuming it to be constant.

3.4: Non-Uniform Electrical Pumping: DC Simulations

3.4.1: The Device Parameters

The split-contact semiconductor laser structure simulated in this section is illustrated in Fig. 2.1.1. For brevity, in this work we only consider two-section structures, although the model is capable of describing an arbitrary top-contact geometry. The distance separating the top contacts is also assumed to be small compared with the length of the metallized sections of the laser, so that this unpumped region can be ignored. The relevant device parameters are given in the Glossary in Appendix D, unless otherwise stated.

3.4.2: Varying Bias for a Fixed Geometry

We begin by considering a 500 μm long device, with contact lengths $L_1 = 350$ μm and $L_2 = 150$ μm. This structure is referred to as laser **M1** hereafter. Simulations have been performed for a constant current bias on one contact, while the current into the other contact is varied. Three of the resulting steady-state *L-I* characteristics are plotted in Fig. 3.4.1, for cases where the bias on the 150 μm contact is fixed.

There are several points of interest in these curves. We see that, at least qualitatively, they are quite similar in structure to the uniformly biased simulation shown in Fig. 3.3.3: each curve consists of a region below threshold that is weakly emitting and an above threshold section with strong light emission and a linear current dependence. For

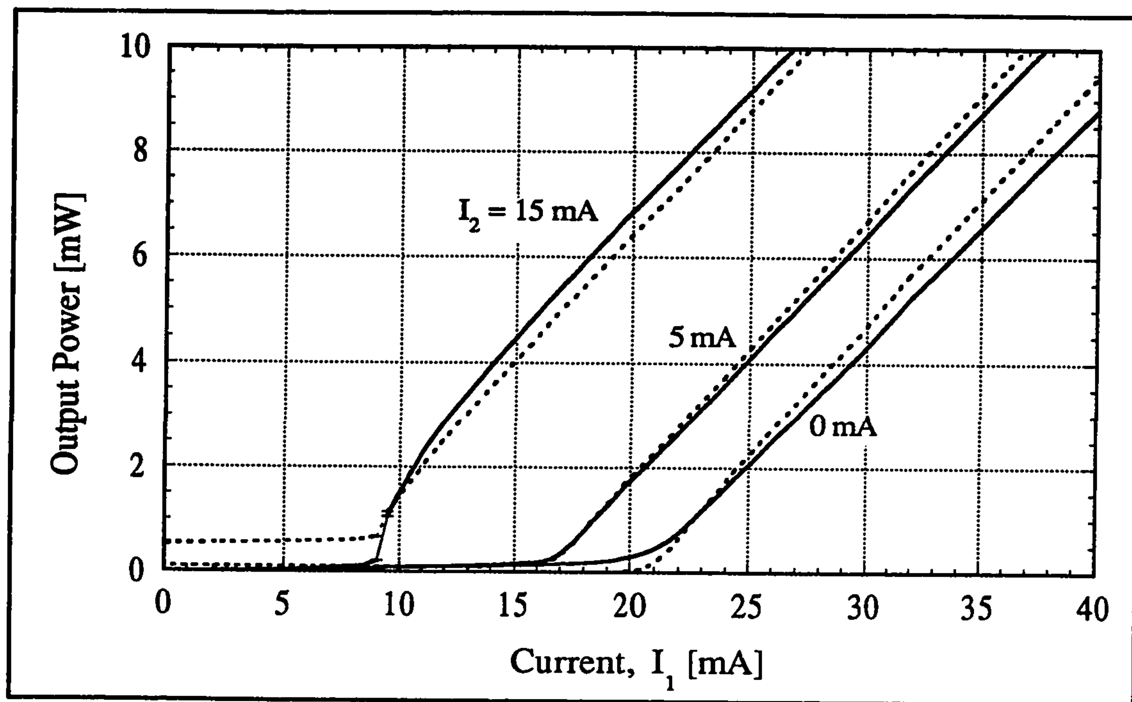

Figure 3.4.1: *L-I* Simulations with I_2 Fixed

The simulated *L-I* characteristic of laser **M1**, for which the current I_2 is fixed at 0, 5, and 15 mA. Solid lines represent the output from facet #1,[a] while the broken lines are for facet #2. Small horizontal dashes indicate the limits of the discontinuity at threshold.

reasons outlined in Section 3.3.3, the differential optical efficiency above threshold is nearly unity in all cases, but the position of threshold varies with the fixed bias I_2. As one might expect from considerations of the total current supplied to the device, a larger value of I_2 results in a lower threshold current.

The detailed behaviour of the device near threshold is also strongly influenced by the value of I_2. For low I_2 (0 and 5 mA), the optical characteristics are similar to the uniformly biased case (Fig. 3.3.3); they are smooth, continuous, and have a positive

[a] Facet #1 is defined as the one closest to contact #1, biased with current I_1.

curvature over the entire range. When $I_2 = 15$ mA, however, the situation is different. Threshold here is not a smooth transition: there is actually a discontinuity at $I_1 = 9.5$ mA in the *L-I* that separates the lasing and non-lasing states. The slope above threshold also decreases with increasing I_1, whereas it was increasing for $I_2 = 0$ and 5 mA. This type of behaviour is characteristic of a split-contact device, when the variation between the pumping rates in the two sections is large. When $I_2 = 15$ mA, the portion of the active region under contact #2 is strongly pumped even when $I_1 = 0$. This is indicated by the large amount of light emitted from facet #2 (~0.5 mW) even below threshold: this end of the laser is operating in the superluminescent regime. When I_1 is increased to ~9 mA, section #1 is pumped strongly enough for the saturable absorber effect to manifest itself. The absorption of superluminescent light from section #2 now generates sufficient carriers under contact #1 to decrease the absorption in that portion of the device, making it more transparent and allowing lasing to occur. This saturation is an abrupt effect, and causes the observed discontinuity in the *L-I* at threshold.

The simulated spectra of **M1** that correspond to the *L-I* in Fig. 3.4.1 are plotted in Fig. 3.4.2. When biased substantially above threshold, the dominant laser mode is #6 in all three cases; this seems reasonable, as this was also the lasing mode for the uniformly pumped laser of the same length (Fig. 3.3.4). As the current increases above threshold we expect the split-contact laser to behave more like a uniformly pumped device, because optical pumping of the weakly biased end tends to even out the carrier density along the length of the laser.[a] This redistribution of the carriers means that the gain is more uniform along the laser length, so that the interesting effects specific to split-contact lasers are generally observed near threshold.

---

[a] This will be shown explicitly in Fig. 3.4.3.

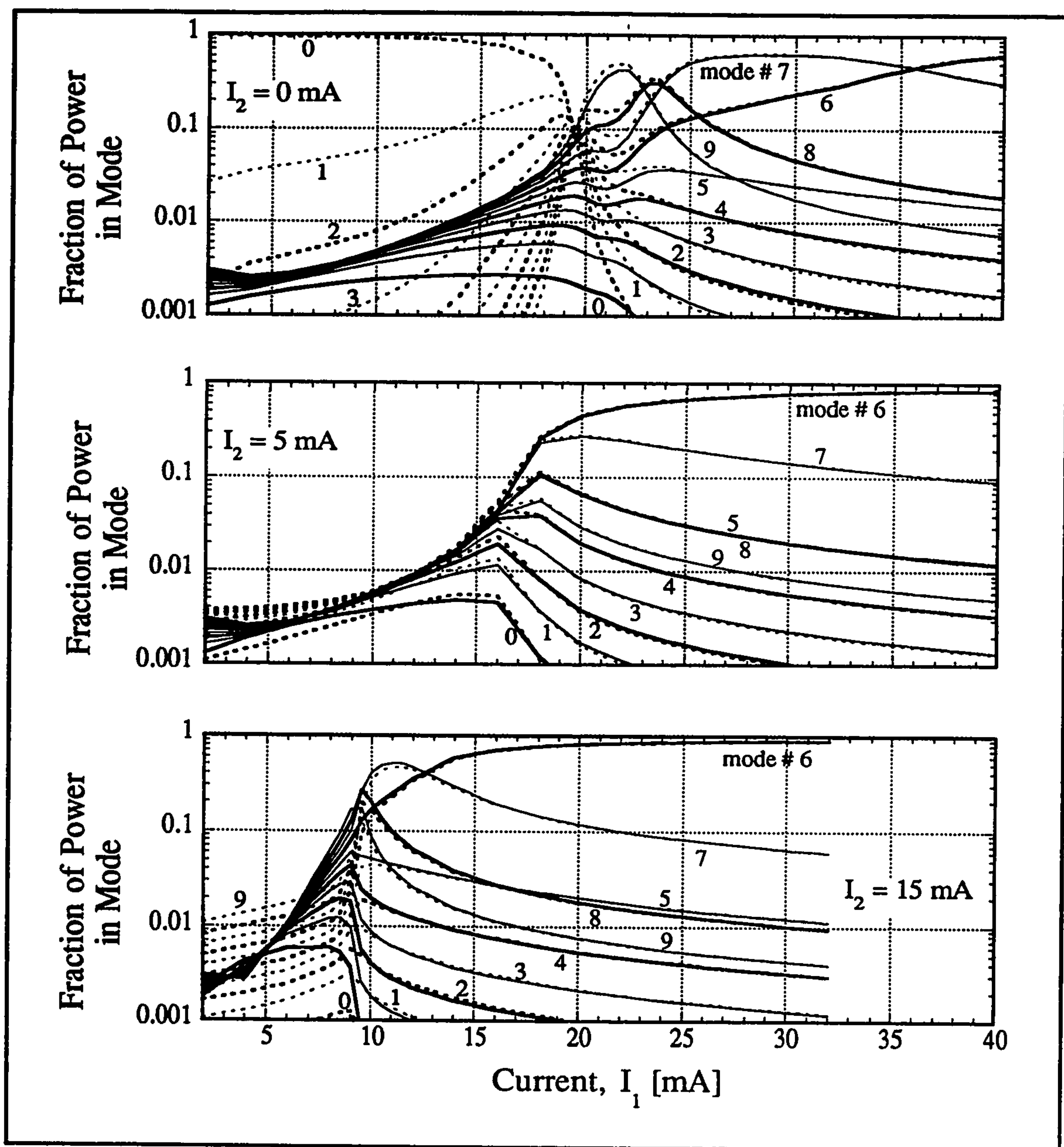

Figure 3.4.2: Spectral Simulations with I_2 Fixed

For laser **M1**, the fraction of the total power that is emitted in each mode is plotted versus the bias current, I_1, for $I_2 = 0$ (top), 5 mA (middle), and 15 mA (bottom). Solid lines indicate the output from facet #1; broken lines are for facet #2.

In all three cases we observe that the spectral output from the different facets of the laser is practically the same above threshold, although this is not the case at lower currents. When biased below threshold the net round-trip gain of the cavity is less than unity, and, as the simulated spectra indicate, the two sections of the laser behave as two independent LEDs. Above threshold, however, the laser facets and active region form a resonant cavity, and since the light makes multiple passes through both parts of the laser, the optical output from the two facets is strongly coupled. Although the total amount of light from each facet may differ to some extent, the spectral distributions are virtually identical for biases greater than a few milliamps above threshold.

Unlike the uniformly pumped case, when the bias is non-uniform along the device length our simulations indicate that mode hopping can occur. In particular, for $I_2 = 0$ mA the simulations indicate that for I_1 between 20 and 40 mA the dominant mode changes from #9 through #6, successively. For $I_2 = 5$ mA lasing always occurs in the 6th mode as I_1 varies, but at $I_2 = 15$ mA a hop from mode #7 to #6 is observed at $I_1 = 12.5$ mA. To understand the reason for this behaviour, we must consider the strength of the pumping under these different bias conditions. Figure 3.4.3 illustrates the simulated carrier distribution in the cavity under four conditions: with $I_2 = 0$ and 5 mA, $n(x)$ is plotted for both I_1 at threshold and 40 mA.

Figure 3.4.3 allows us to compare the carrier distribution in the active region for $I_2 = 0$ and 5 mA, at levels of I_1 equal to threshold and 40 mA. At $I_1 = 40$ mA (the broken lines) we see that the carrier profiles at $I_2 = 0$ and 5 mA are quite similar: in fact, they differ by 4×10^{16} cm^{-3} at the most over the device length.[a] Since Fig. 3.4.2 indicates

---

[a] This difference may be large compared with the those shown for the uniformly pumped case in Fig. 3.3.5, but, as Fig 3.4.3 indicates, it is minimal compared to the variations that occur close to threshold.

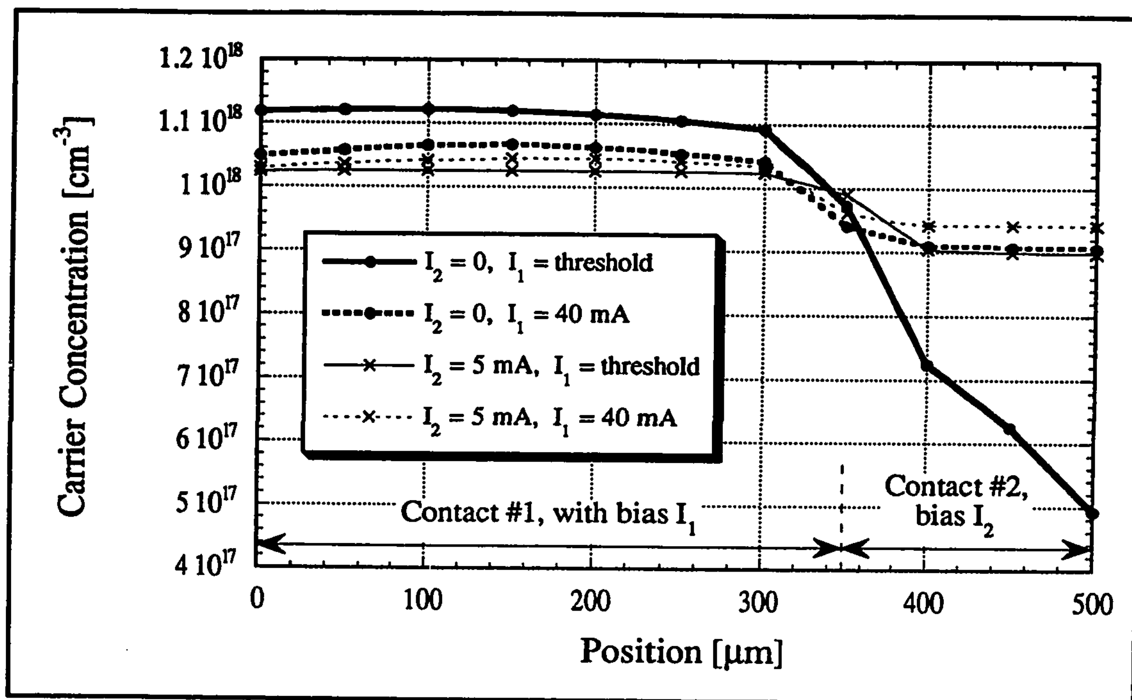

Figure 3.4.3: Carrier Profiles At and Above Threshold
The carrier density in the active region of laser **M1** is plotted vs. position, under four bias conditions. The solid lines represent the $n(x)$ when I_1 is at threshold, and the broken lines are for $I_1 = 40$ mA. The position and size of the electrical contacts are indicated at the bottom of the plot.

that in both these cases the dominant lasing mode is the same (#6), it is not surprising that the carrier profiles also match closely.

However, when we compare the carrier distributions just above the lasing threshold (the solid lines in Fig. 3.4.3), we note that the difference between the $I_2 = 0$ and 5 mA curves can be up to $4\text{x}10^{17}\ \text{cm}^{-3}$. At $I_2 = 5$ mA the distributions at threshold and $I_1 = 40$ mA are quite similar, and since one would expect that similar carrier distributions produce similar gain profiles, it is not surprising that the $I_2 = 5$ mA spectra show no mode hopping between I_1 = threshold and 40 mA.

The situation is quite different when $I_2 = 0$. In this case there is no electrical pumping of contact #2, and the carrier distribution in the cavity is quite uneven at low biases. In Fig. 3.4.3 we see that the carrier profile changes considerably between I_1 = threshold and 40 mA, because of carrier generation under contact #2 by photon absorption. This effect explains the change in the lasing mode from the 9th to the 6th in Fig. 3.4.2: the change in the carrier distribution has shifted the peak in the net cavity gain by three cavity modes (or, in terms of wavelength, by about 15 Å).

Thus far we have shown simulations for which I_2 was kept constant and I_1 swept to generate the *L-I* characteristics. Of course, we can just as easily fix I_1 and vary I_2. A comparison of these two bias configurations is plotted in Fig. 3.4.4.

Although the value of the threshold current is approximately 21 mA for both $I_1 = 0$ and $I_2 = 0$, the details of the two *L-I* curves in Fig. 3.4.4 differ considerably. In particular, the optical characteristic with the long contact open circuited ($I_1 = 0$) exhibits several of the phenomena that have been found to be characteristic of non-uniformly pumped lasers. In addition to a discontinuity at threshold (similar to the case where $I_2 = 15$ mA in Fig 3.4.1), the simulation with $I_1 = 0$ also has a small region of optical hysteresis, and a range of bias currents for which the device generates self-sustaining pulsations. This self-pulsing effect is treated in more detail in Section 3.5.

The origin of the hysteresis can be understood as follows. Bistability in the *L-I* is a phenomenon in which two distinct operating states are possible at a single bias, and is a consequence of the saturation of the absorption in the unbiased portion of the laser. As the bias I_2 is increased it raises the rate of photon generation in section #2, which in turn generates more carriers under contact #1 via absorption. Since these excess carriers lower the absorption of the unbiased portion of the laser (see Fig. 2.4.2 for the dependence of

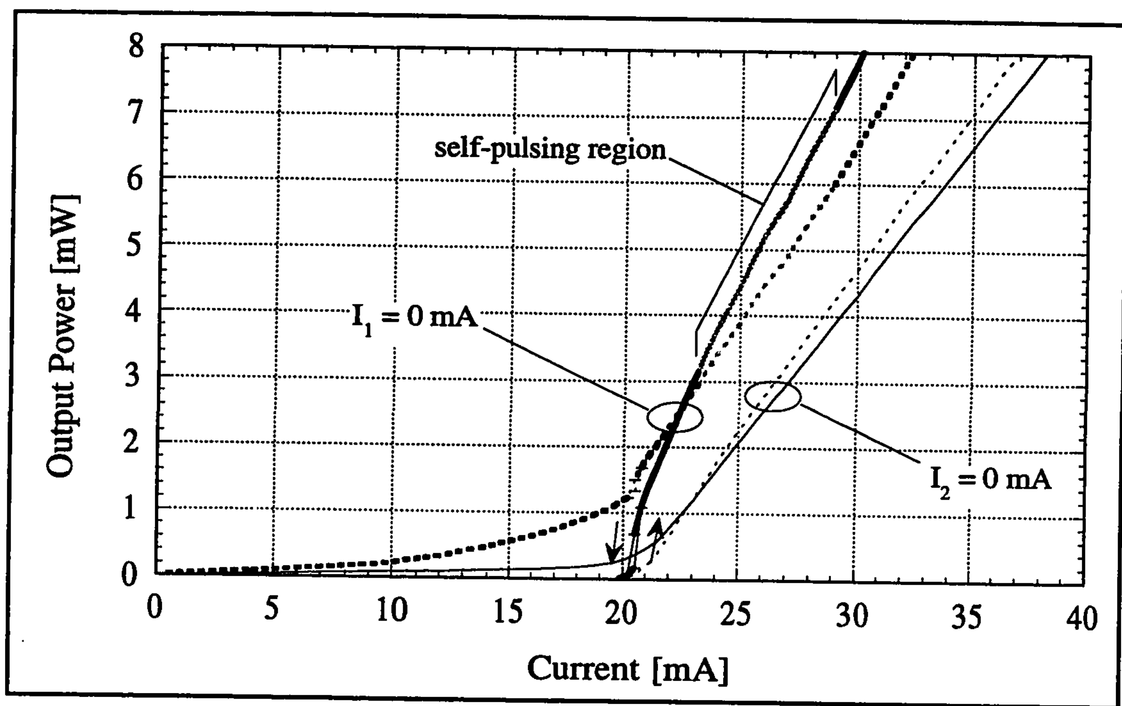

Figure 3.4.4: *L-I* Curves with Either Contact Open Circuited
The simulated optical characteristics of laser **M1** are plotted; sweeping the current bias on either contact. Solid lines represent the output from facet #1; broken lines are for facet #2. Regions of the characteristics that are shaded more lightly indicate that the device is generating self-sustained pulsations, and we have plotted time average for these points. There is also a small region of hysteresis in the curve for $I_1 = 0$: the direction of the current sweep is indicated by the arrows beside the loop. Small horizontal dashes show the limits of the discontinuity at threshold.

the absorption on carrier density), eventually the cavity loss drops to the point where lasing commences, and we see an abrupt increase in the optical output of the device. However, once this transition has been made, I_2 can actually be decreased slightly before the absorber recovers. Although the electrical bias inside the hysteresis loop is not sufficient to ***initiate*** lasing, it is enough to ***maintain*** it after it has begun. The result is that we have two possible operating states (optically "on" and "off") for a particular bias (in this case $I_1 = 0$, $I_2 = 20.5$ mA); the actual state that the device is in at a given time depends on previous biases through which the laser passed to reach this state. In other words, the split-contact

laser can be biased in an optically bistable mode, which introduces the possibility of applications as an optical memory element.

Figure 3.4.5 illustrates the carrier density in the active region in the ON and OFF states of the optical hysteresis loop shown in Fig. 3.4.4. It demonstrates that the change in the carrier profile needed to switch between the lasing and non-lasing states is relatively small, compared to the total carrier density. Although this slight redistribution of the carriers has a large effect on the device output, the laser cannot make the transition between the two states without some sort of external trigger (a variation in the bias current or an

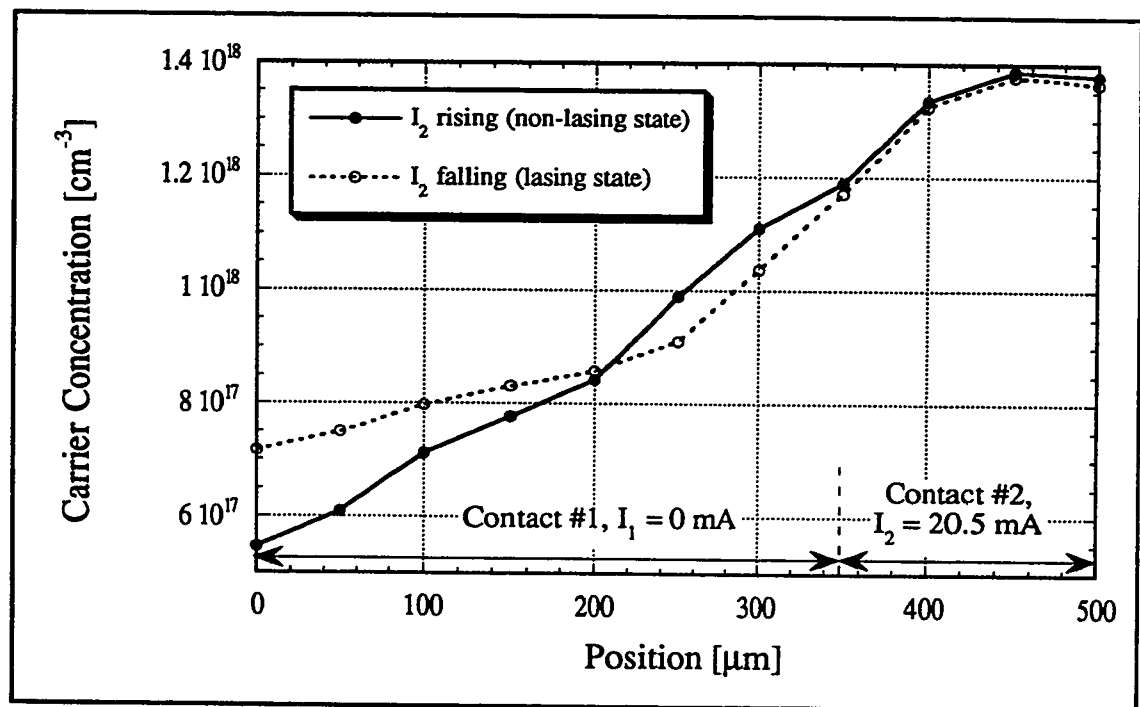

Figure 3.4.5: Carrier Profiles in the Hysteresis Loop
The carrier density in structure **M1** is plotted as a function of position, with a bias $I_1 = 0$ and $I_2 = 20.5$ mA. The solid curve represents $n(x)$ when I_2 is increasing (the lower segment of the loop), and the broken curve represents I_2 decreasing (the upper, lasing state).

incident optical signal).

The reason that these effects are observed for $I_1 = 0$ but not for the other biases simulated is that in this case the longer of the two contacts is held at a low bias. This means that there is a larger volume of active region acting as an absorber, which therefore requires a greater amount of light to achieve saturation. Since this optical energy is supplied by the electrically pumped portion of the device, a higher carrier density is required here to generate the additional light. Because of this, it is evident that when the absorbing section is longer, the pumping level in the biased section must be correspondingly greater for saturation to occur. Since the effects in question are a consequence of non-uniform pumping, one would expect phenomena such as hysteresis and self-pulsations to be more prominent when the device contains long, unbiased regions. We can confirm this line of reasoning by considering the limit in which the length of the unbiased region approaches zero: in this case we would expect its contribution to the laser performance to be minimal, and the device to behave as if it were uniformly biased.

To give an overall impression of how our model predicts the output of this laser to vary with bias, in Fig. 3.4.6 we have plotted several contours of constant output power as a function of the laser bias currents. These lines indicate the sets of bias conditions for either the threshold condition or a given output power level. The general trend that this plot suggests is an intuitive one: increasing either (or both) of the bias currents causes an increase in the output power of the laser. By appropriately varying both currents so that the bias point moves along one of the contour lines, we are able to maintain the selected output power. This could be useful in situations where we wish to tune the lasing wavelength while maintaining a constant output power level. For instance, by varying the bias from (I_1, I_2) = (25, 0 mA) to (21, 5 mA) the laser can be tuned from the 7th to the 6th cavity mode while preserving the output power at 2 mW.

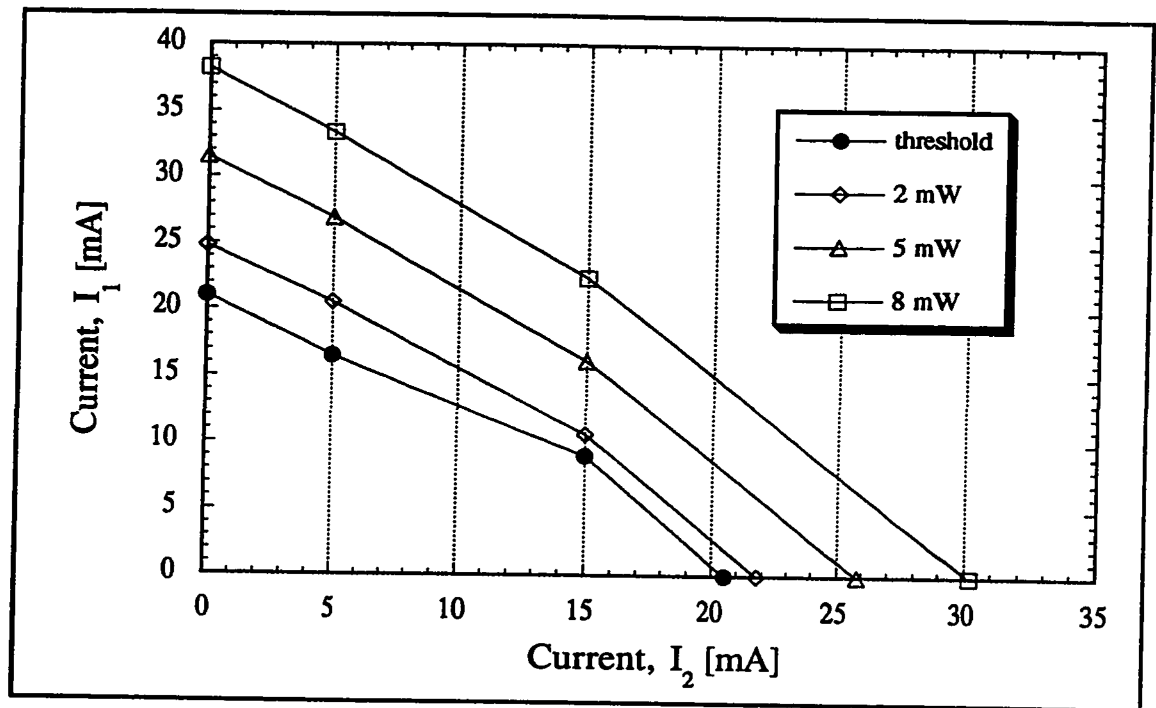

Figure 3.4.6: Optical Output Power Contours

Contours of constant output power (from facet #1) are plotted in the I_1-I_2 plane, for device **M1**. The data points in this figure are taken from the simulated *L-I* curves shown in Figs. 3.4.1 and 3.4.4.

It is also interesting that although the contours in Fig. 3.4.6 are nearly straight lines, the total amount of bias current $(I_1 + I_2)$ varies by up to ~30% along a given contour line: to reach a given condition, we require less total current if the majority of it flows through contact #1. This is due to the fact that the carrier injection is not uniform, and to the non-linear relationship between the carrier concentration and stimulated and spontaneous emission rates that we have included in our model (see Sections 2.3 and 2.4).

In regions of the I_1-I_2 plane where the current densities are large (i.e. when the majority of the current is confined to one contact), one might expect that effects such as heating and carrier leakage out of the active region to be noticeable in a real laser. This would increase the total bias current required to reach a given power level near the edges of

the plot, bending the extremities of the contours away from the axes.[*] However, since our model does not include these effects, it is not surprising that our simulated contours do not display this curvature.

3.4.3: Different Contact Geometries

Thus far our discussion of non-uniform pumping has been restricted to a single device geometry, i.e. **M1**, with contact lengths $L_1 = 350\ \mu m$ and $L_2 = 150\ \mu m$. It is, of course, of considerable value to understand how variations in the lengths of these contacts affect device performance, so that structures can be designed that optimize particular properties of the laser. To this end, we now consider a laser that we denote by **M2**, with the same total length as **M1** ($L_T = 500\ \mu m$), but with $L_1 = 433\ \mu m$ and $L_2 = 67\ \mu m$. Figure 3.4.7 shows the simulated *L-I* characteristics of both these devices, with a constant bias on the longer contact ($I_1 = 0$), and the bias on the shorter contact, I_2, varied.

The *L-I* of lasers **M1** and **M2** contrast in several ways. Firstly, we see that the threshold current for **M2** is ~28.5 mA, approximately 8 mA greater than the value for **M1**. This is because the total amount of absorption under the unpumped contact increases approximately exponentially with its length. Now, in order to reach threshold the round trip gain of the laser cavity must approach unity. Since the unbiased section in **M2** is longer than that in **M1**, a greater bias is needed to saturate the absorbing section in **M2**, and therefore a greater bias current is required to achieve threshold.

The second obvious difference in the characteristics in Fig. 3.4.7 is the fact that the discontinuity at threshold for device **M2** is several times larger than for **M1**. The reason

---

[*] See Section 4.5 for experimental evidence of this.

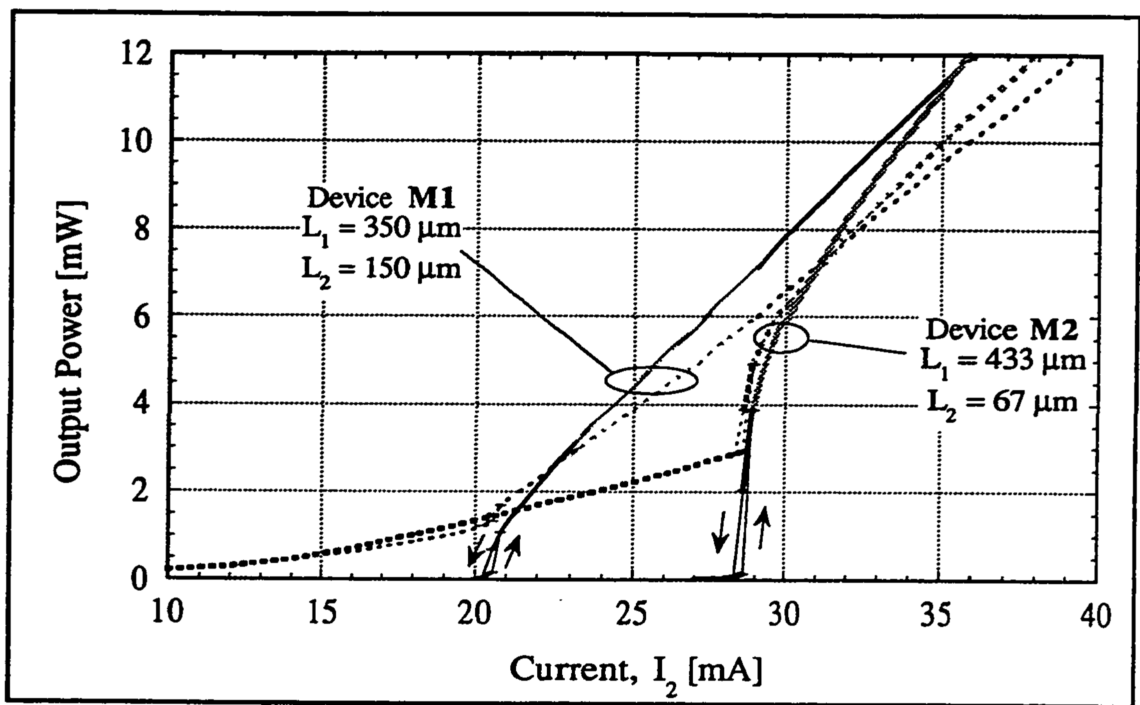

Figure 3.4.7: *L-I* of Two-Contact Lasers with the Same Total Length

The *L-I* characteristics for devices **M1** and **M2** are plotted, where $I_1 = 0$ and I_2 is swept between 10 and 40 mA. Solid lines represent the output from facet #1; broken lines represent facet #2. In the lighter coloured portions of the curves the devices were unstable: the time-averaged power in the light pulses has therefore been plotted. The direction of the current sweep in the hysteresis loops is indicated by arrows beside the *L-I* curves, and small horizontal dashes show the limits of the discontinuity at threshold.

for this difference is linked to the higher value of threshold for **M2**, as follows. The discontinuity occurs because the saturation of the absorbing section is an abrupt effect: when the absorber reaches saturation the associated loss in the cavity suddenly drops, and the steady-state light output jumps immediately into a lasing state. The exact level to which the output jumps can only be determined by going through our full simulation calculations; however, we have argued (in the previous paragraph) that it takes a greater amount of light, and a correspondingly larger current bias, to saturate a longer absorbing region. When saturation occurs and the associated absorber loss disappears, we would therefore expect

the output to jump to a higher level for the device that is more strongly biased. Thus, the larger discontinuity at threshold for laser **M2** is a consequence of it occurring at a higher bias level, which is in turn due to the fact that in device **M2** the unbiased contact is longer.

The *L-I* for **M1** and **M2** in Fig. 3.4.7 also differ in the ranges for which self-sustained pulsations occur (the sections of the curves shaded grey). Laser **M1** oscillates for 23 mA $\leq I_2 \leq$ 28.5 mA (a range that commences ~3 mA above threshold), whereas **M2** produces pulsed emission at all $I_2 > I_{th}$ (at least up to the highest current simulated, I_2 = 60 mA). As explained in Chapter 1, the self-sustained pulsations that occur under non-uniformly biased conditions are caused by absorption saturation in the weakly pumped section of the laser. Since this effect is strongest in laser **M2** (the device with the greatest ratio of unpumped to pumped length), it is not surprising that this device exhibits oscillations over a broader range of currents, as well as a larger discontinuity at threshold. We will discuss this self-pulsing behaviour in more depth in Section 3.5.

In addition to varying the ratio of the lengths of the contacts in lasers of the same length, we have also performed simulations for lasers with different total lengths. In particular, we have simulated structure **B1**, which has L_1 = 850 μm and L_2 = 150 μm. This device has the same length for contact #2 as **M1**, but contact #1 is 500 μm longer. The simulated *L-I* characteristics for **B1** are plotted in Fig. 3.4.8; these can be compared to the corresponding plots for **M1** shown in Fig. 3.4.4.

The data for laser **B1** in Fig. 3.4.8 confirm several of the trends we observed for device **M1** in Fig. 3.4.4. In both cases, when the shorter contact is unbiased ($I_2 = 0$) the *L-I* is similar to that of a uniformly pumped laser: the output is continuous, linear above threshold, and non-oscillatory. When $I_1 = 0$ (i.e. the long contact is unbiased), **B1** also exhibits the phenomena we associate with non-uniform pumping: a discontinuity at threshold, hysteresis, and self-sustained pulsations.

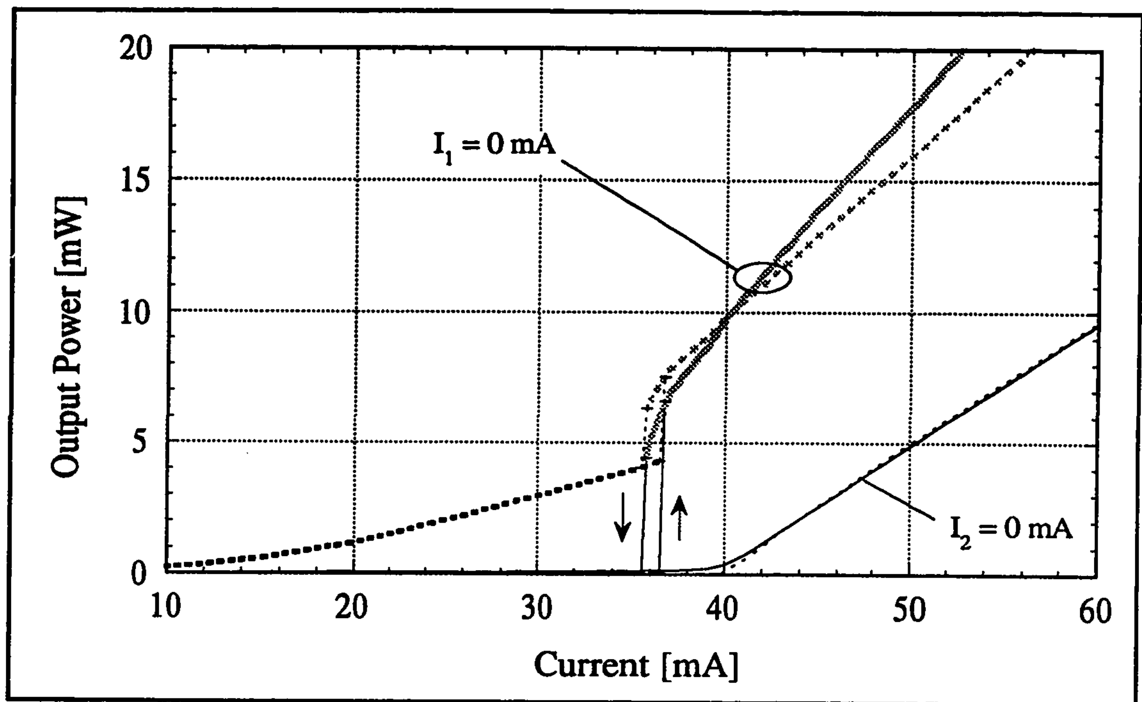

Figure 3.4.8: *L-I* Characteristics of a 1000 μm Split-Contact Laser
The optical characteristics of laser **B1** are plotted for two bias configurations. Solid lines represent the output from facet #1; broken lines represent facet #2. In the portions of the curves shaded more lightly the device was unstable: the time-average over the pulses has been plotted. The direction of the current sweep in the hysteresis loops is indicated by arrows beside the *L-I* curves, and small horizontal dashes show the limits of the discontinuity at threshold.

A close comparison of Figs. 3.4.4 and 3.4.8 indicates that device **B1** displays these non-linear properties to a greater extent than **M1** did. For $I_1 = 0$ (i.e. driving the current I_2 through a 150 μm contact in both cases), the width of the hysteresis loop is clearly larger for the 1000 μm device (1.0 mA instead of less than 0.3 mA), and the height of the discontinuity is larger (nearly 7 mW instead of ~0.9 mW). Our argument concerning the differences between the *L-I* of **M1** and **M2** also applies here: since the unbiased contact in **B1** is nearly 2.5 times longer than in **M1**, we would expect **B1** to have more pronounced saturable absorber effects.

The sub-threshold output from facet #2 reaches 4 mW for device **B1**, which is a significant fraction of the power achieved even 20 mA above threshold. This is due the elevated carrier densities in the pumped section of the laser: they are high enough to produce a positive optical gain at wavelengths near the band edge, so that the spontaneous emission generated under contact #2 is amplified. Although this type of elevated optical output below threshold does exist for devices **M1** and **M2** (see Fig. 3.4.7), threshold is reached in the shorter lasers before it rises to the level that **B1** reaches. We attribute the greater amount of sub-threshold light from **B1** to its longer unbiased contact, more light being required to saturate a longer absorber. As discussed in Section 1.3.1, there are applications in which amplified spontaneous emission from a laser is desirable, so it is advantageous for our simulations to be able to predict the dependence of this effect on the laser parameters.

3.4.4: High Reflectivity Facets

Although we have discussed the effects of varying the biases and contact lengths in the previous sections, it has always been assumed that the facet reflectivities are ~28%.[a] In many practical applications it is desirable to coat one (or both) of the facets with a material that changes that facet's reflectivity. For instance, for many high power applications it is necessary to maximize the coupling of the laser light into the receiving optics. In this case we might wish to apply a highly reflective coating to the back laser facet, so that the majority of the optical power is emitted from the front. To investigate the effects of different facet reflectivities on split-electrode lasers, we have therefore performed the following simulations.

[a] This value is determined by assuming simple InGaAsP-air facet, with a real refractive index in the semiconductor of 3.27.

We define structures M3 and M4 to be identical to M1, except that we make $R_1 = 90\%$ for M3, whereas for M4 we set $R_2 = 90\%$ (see Appendix C for a complete summary of these structures). In both cases, the other facet remains 28% reflecting. Figure 3.4.9 illustrates the simulated *L-I* curves for lasers M3 and M4, along with the $I_2 = 0$ mA curves for device M1, reproduced from Fig. 3.4.1. The bias configuration for the three devices is the same (i.e. I_2 is held constant at 0 mA while I_1 is swept); the only differences between the simulation parameters are the reflectivities of the facets.

The first thing we observe in Fig. 3.4.9 is that the total output powers are

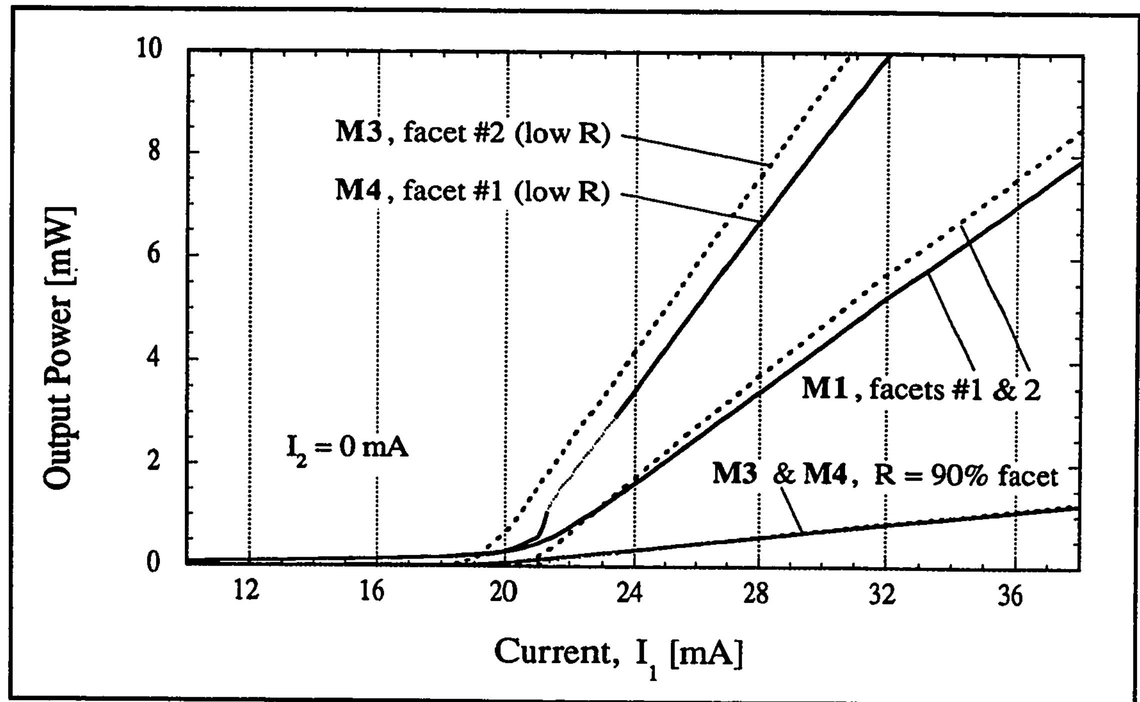

Figure 3.4.9: *L-I* Curves with Different Facet Reflectivities
The *L-I* curves for devices M1 (the basic structure), M3 (with $R_1 = 90\%$) and M4 (with $R_2 = 90\%$) are shown. Solid lines represent the output from facet #1; broken lines represent facet #2. In the portions of the curves shaded more lightly the device was unstable: the time-average over the pulses has been plotted.

approximately equal at a given bias above threshold (at $I_l = 30$ mA, the variation between the devices is less than 12%). In contrast, the ratio of the power from the two facets of any specific structure is strongly dependent on the facet reflectivities (at $I_l = 30$ mA, over 92% of the power is emitted from the low reflectivity facet for **M3** and **M4**, while the output levels from the facets of **M1** are approximately equal). Although this is an interesting result in terms of maximizing the output coupling of the laser light, it is something that one would expect to occur in both split-contact and uniformly pumped lasers.

Somewhat more interesting is the behaviour of the different devices near threshold. Although the threshold currents for the three structures are quite similar (they are all within ~1.5 mA of $I_l = 20$ mA), the stability of the laser is dependent on the facet reflectivities. Although lasers **M1** and **M3** behave like "normal" lasers (unistable, with a smooth threshold), **M4** exhibits both a negative curvature and self-pulsations in the region above threshold. As we have seen, both of these effects are due to the saturation of the absorption in the weakly biased section of the laser: this simulation therefore demonstrates that self-pulsations are dependent not only on the bias and the length of the absorbing section, but also on the reflectivity of the proximate laser facet.

3.5: Self-Sustained Pulsations

3.5.1: Detailed Self-Pulsing Examples

The self-sustaining optical pulses generated by non-uniformly pumped semiconductor lasers are of considerable interest to us, both from a purely scientific viewpoint and in terms of practical applications. Although we have indicated the regions of our *L-I* simulations in the previous section for which this oscillatory behaviour is observed, it now seems appropriate to investigate the matter in more detail.

In Fig. 3.5.1 we have plotted samples of the simulated pulse trains for lasers **M1** and **M2**, in order to examine the two types of self-pulsing behaviour more closely. The bias conditions ($I_1 = 0$ and $I_2 = 28$ mA for **M1**, $I_1 = 0$ and $I_2 = 38$ mA for **M2**) were chosen to give approximately the same oscillation frequency for the two devices, in order to make comparisons easier. The output power from both facets is plotted, along with the average carrier concentration in the active region, $\bar{n}$, so that we can investigate the relationship between these three parameters. We note that the shape and size of the optical pulses from M2 are quite similar to those measured experimentally by Marcenac et al.[11] and Farrel et al.[12]

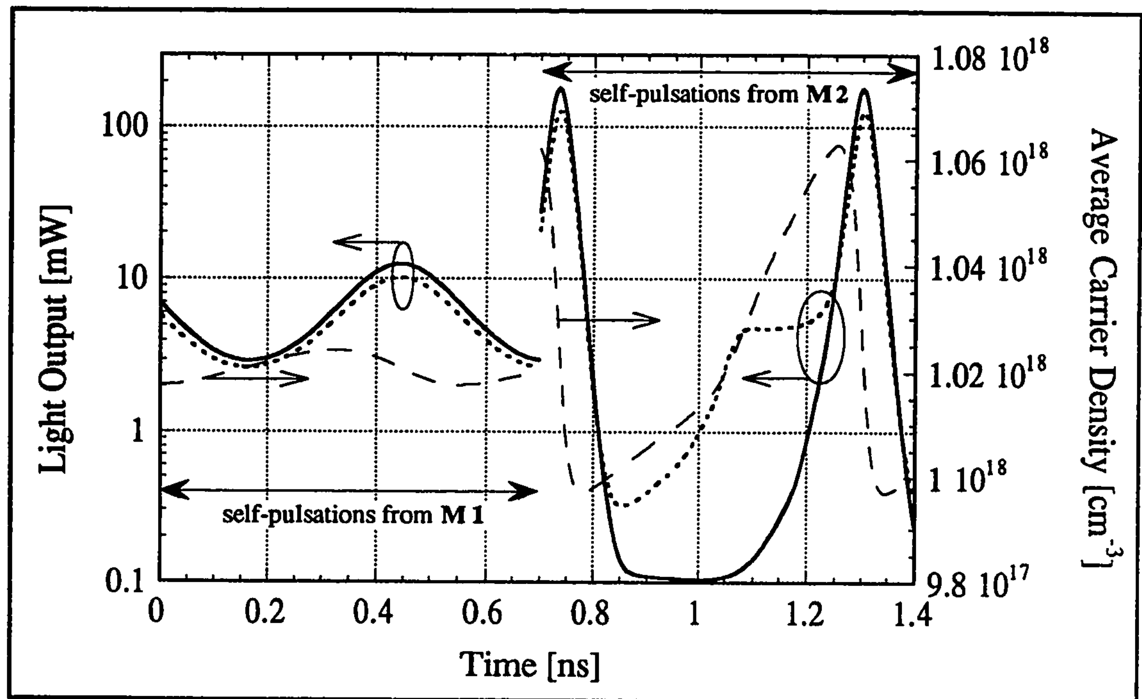

Figure 3.5.1: Simulated Self-Sustaining Pulse Trains

The output power from facets #1 (solid) and #2 (dotted), and the average carrier density (dashed) are plotted vs. time. $0 \leq t \leq 0.7$ ns represents device **M1**, biased with $I_1 = 0$ and $I_2 = 28$ mA; $0.7 \text{ ns} \leq t \leq 1.4$ ns covers laser **M2**, with $I_1 = 0$ and $I_2 = 38$ mA.

The first impression one receives from Fig. 3.5.1 is that, at approximately the same self-pulsing frequency, the depth of modulation of the light output, and of $\bar{n}$, is much greater for **M2** (0.7 ns $\le t \le 1.4$ ns) than for **M1** ($0 \le t \le 0.7$ ns). The on-pulses from laser **M2** are sharp spikes with a FWHM ~ 35 ps (note that the light output is on a logarithmic axis in Fig. 3.5.1) and with an maximum-to-minimum power ratio of about 2000; the oscillations from **M1** are much smoother, having a FWHM of ~200 ps and a maximum-to-minimum ratio of 4.2.

We also notice that the structure of the light pulses from **M2** is more complicated than it is in those from **M1**. For **M1**, the outputs from facets #1 and 2 are essentially identical, except for a small scaling factor. Since this is not the case for laser **M2**, we now consider its behaviour in some depth. After the minimum of the first pulse (at $t \sim 0.86$ ns in Fig. 3.5.1) the output P_2, from facet #2, begins to recover considerably more quickly than P_1 (from facet #1). Facet #2's output increases while #1's remains essentially constant up to $t \sim 1.08$ ns, at which point P_2 reaches a plateau and P_1 finally starts to increase. After another ~0.16 ns P_1 has become comparable to P_2; from here on both outputs rise rapidly, peak at $t \sim 1.3$ ns, and fall back in a short time to their minimum level.

This behaviour in laser **M2** can be interpreted as follows. We begin by considering time $t \sim 0.86$ ns, at which point the carrier densities are low enough that neither section of the laser causes significant amplification of the spontaneous emission. However, since section #2 is under forward bias, P_2 soon begins to rise as the diminished carrier concentration is restored by the current I_2. It is only when P_2 reaches approximately 4 mW that the absorption of light under contact #1 becomes strong enough to noticeably affect the carrier density in section #1. At this point the amplified spontaneous emission from section #2 begins to bleach the absorbing section, a process which is sufficiently complete by

$t \sim 1.24$ ns that lasing commences, and the power from both facets rises abruptly. An effect of this rapid increase in the light emission is that the carrier density in the laser cavity is depopulated, limiting the peak power to which P_1 and P_2 can rise. In fact, this reduction of the carrier density is sufficient to drop the gain in both sections of the laser to a level at which lasing is no longer possible, which brings us back to the point in the self-pulsing cycle at which we began.*

Clearly, this argument is not true for laser **M1**. Although the general mechanism underlying the self-pulsations is the same (feedback between the amplification of light by the carrier density in the active region and the reduction of the carrier density by stimulated radiative emission), the extent to which it occurs in **M1** is not as great as for device **M2**.

Comparing the optical output of **M1** in Fig. 3.5.1 with its *L-I* curve in Fig. 3.4.4, we see that the minimum output power during self-pulsing (~3 mW) exceeds the lasing power just above threshold (this occurs at $I_2 = 20.5$ mA, and is ~0.7 mW). In other words, for device **M1** the self-sustained pulsations are a modulation of a continuously lasing output, rather than a switching on and off of the lasing, as in **M2**. The pulses generated by laser **M1** are quite similar, in fact, to the relaxation oscillations observed in a uniformly biased device (see Fig. 3.3.2). In both cases the oscillation is a modulation of a continuously lasing output, the difference being that they are damped out in the uniformly pumped case, while the saturable absorber effect sustains them indefinitely in the split-contact laser.

The reason why the peak instantaneous power from **M2** is so much greater than from **M1** is now apparent. During the time which **M2** is not lasing the carrier density is

---

* This gain saturation effect, which is caused by the high photon flux, is also observed in a related device configuration under external optical pumping conditions, as shown in Section 3.7.3.

allowed to build up to levels greater than the "normal" threshold density, so that when the absorber eventually saturates there are many more carriers available to contribute to the optical gain. This method of giant pulse generation is known as Q-switching or Q-spoiling.

To further substantiate this explanation for the simulated device behaviour, we have plotted the carrier density profile in the active region for lasers **M1** and **M2** in Fig. 3.5.2, at selected times during the self-pulsing cycle. $n(x)$ is shown at the times when $\bar{n}$ is at both its maximum (solid lines) and minimum (broken lines) values. Referring back to

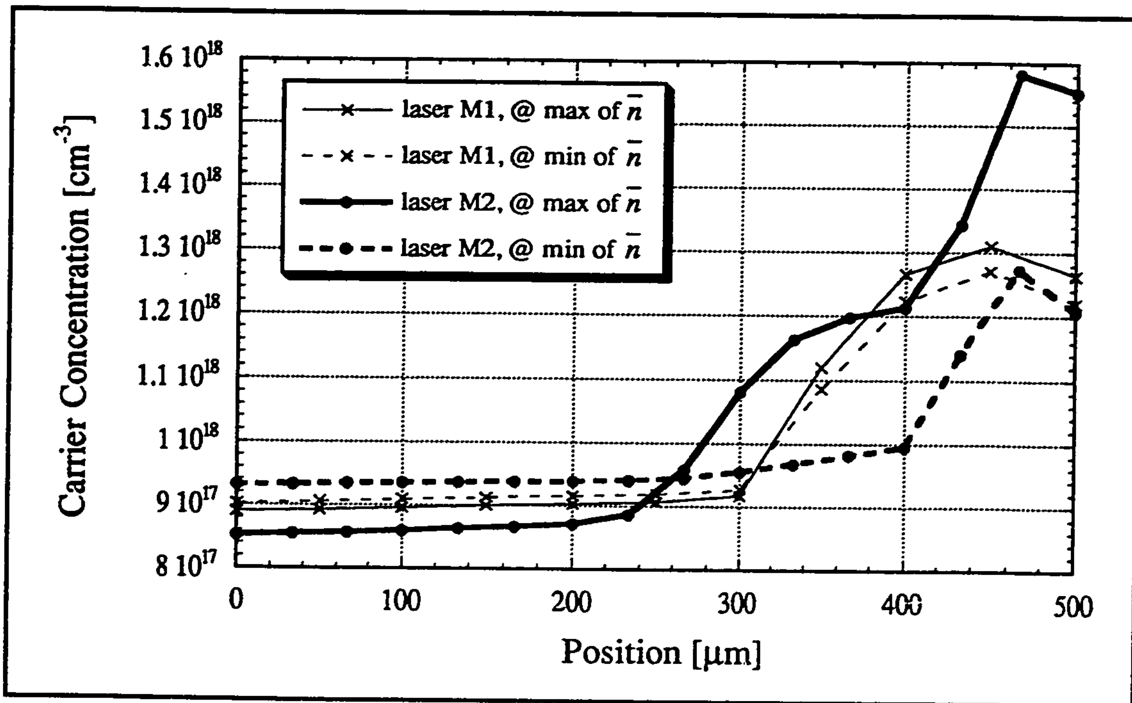

Figure 3.5.2: Simulated Carrier Density Profiles During Self-Pulsations

The carrier concentration is plotted as a function of position in the active region. Thin lines represent data from laser **M1**, thick represent **M2**. Solid curves are taken at the times when $\bar{n}$ for each device is a maximum (see Fig. 3.5.1), while broken lines are at the minima of $\bar{n}$.

Fig. 3.5.1, these maxima are at $t \sim 0.32$ ns for **M1** and 1.25 ns for **M2**; the corresponding minima occur at 0.56 ns and 0.78 ns.

The trends observed in Fig. 3.5.2 verify our interpretation of the two types of self-sustained pulsations that our model has generated. As expected, we see that the change in the carrier profile over the oscillation cycle for laser **M1** (indicated by thin lines) is quite small compared to the variations in **M2**. The maximum level to which the carriers accumulate before the output pulse from **M2** (solid, thick curve) is also substantially greater than for **M1**, a result of the Q-spoiling behaviour in **M2**. These excess carriers in the region $x > 400$ µm are available to contribute to the optical gain once the absorber saturates, which leads to the enhanced peak pulse power from this device. In fact, we see evidence of the beginning of absorber saturation in the $n(x)$ curve for **M2**: in the curve for which $\bar{n}$ is a maximum (solid thick line), absorption has caused a significant increase in $n(x)$ in section #1 near the contact junction (which is at $x = 433$ µm). However, this increase has not yet reached all the way to $x = 0$, so that the absorption in section #1 is still partially unsaturated.

3.5.2: General Pulse Characterization

In order to obtain a more general picture of the self-pulsing behaviour in our split-contact laser simulations, the output pulse frequency vs. bias current is plotted in Fig. 3.5.3 for several device geometries. The contact lengths and L-I of laser structures **M1, M2, M4,** and **B1** have been described in Section 3.4; in addition, we also include the frequency data for another device, **S1**, with $L_1 = 250$ µm and $L_2 = 50$ µm. (The parameters for all of these structures are summarized in Appendix C.)

We see in Fig. 3.5.3 that the range of self-pulsing frequencies in our simulations is from hundreds of MHz to a few GHz, which is what we would expect from previous work

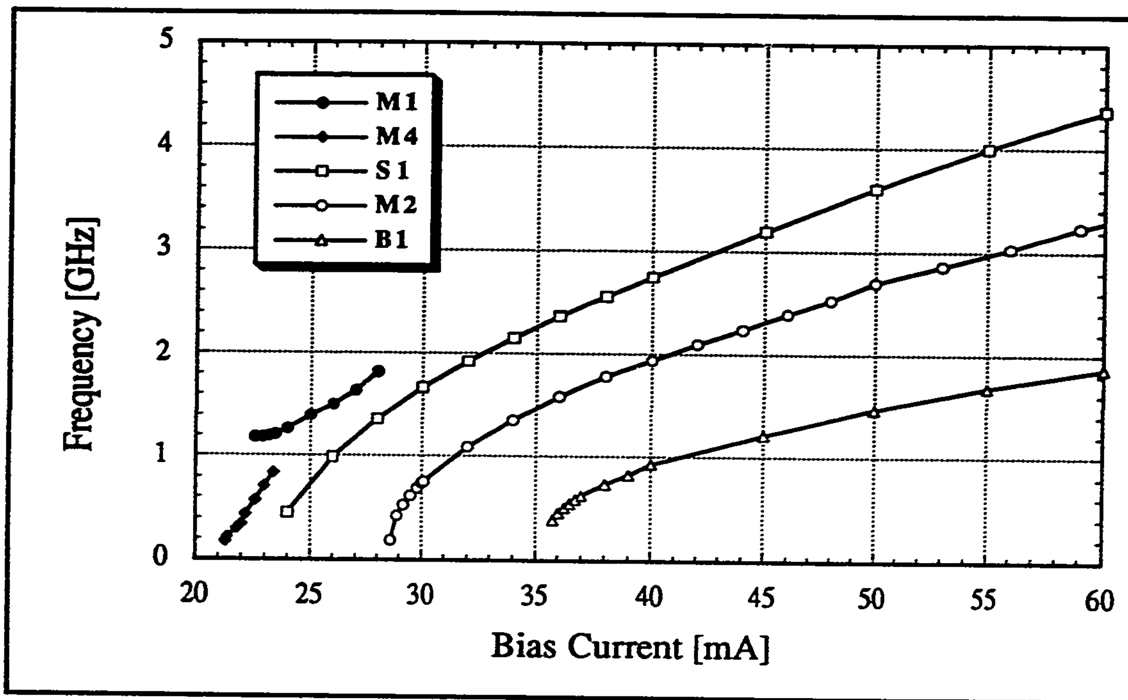

Figure 3.5.3: Self-Pulsation Frequency vs. Bias Current
The frequency of the self-pulsations occurring in the simulations of lasers **M1**, **M4**, **M2**, **S1**, and **B1** is plotted vs. bias current. The data is shown over the entire range over which self-sustained pulsations were found, up to the maximum of 60 mA.

in the field.[13,14] In general the frequency increases with the bias current: we note that for structures **S1**, **M2**, and **B1** the frequency has a sublinear dependence on I_2, but for **M1** and **M4** the dependence is slightly stronger than linear. Of course, these devices are also anomalous in that their oscillations only occur for a small range of biases.

It is also evident that, for lasers **S1**, **M2**, and **B1** biased at a given value of I_2, the oscillation frequencies decreases with device length. This is due, at least in part, to the fact that the lasing threshold increases with device length. In fact, we find empirically that the dependence of frequency on the bias for all three of these structures can be fit quite well[a] by

[a] The least-squares correlation coefficient, R, is > 0.999 for all three structures.

the expression

$$f = f_o(I_2 - I_{th})^z \qquad (3.5.1)$$

where $f_o \sim 0.5 \pm 0.06$ GHz and $z \sim 0.5 \pm 0.08$. Although this does not give a perfect match (to optimize the fit, both f_o and z must be increased slightly as the device length increases), it does serve to illustrate the trend produced by the simulations. Similar current dependencies of the oscillation frequency have been observed experimentally (for example by Barnsley,[15] although he attributes the sublinearity to enhanced carrier leakage at larger biases). Equation (3.5.1) does not, however, apply to the frequency dependence of lasers **M1** and **M4**; in fact, we will find that the oscillations in these devices are irregular in several ways.

In addition to the frequency of the self-sustained oscillations, our simulations also revealed the structure of the pulses generated. In Section 3.5.1 we noted that the waveforms from lasers **M1** and **M2** were fundamentally different; to illustrate these differences more clearly, and since for most applications the maximum and minimum output power during the cycle are important, we have plotted the these parameters in Fig. 3.5.4, for the same laser geometries as were used in Fig. 3.5.3.

As was the case with the oscillation frequency, we again notice in Fig. 3.5.4 that although the curves for devices **S1**, **M2**, and **B1** are similar, **M1** and **M4** do not follow the same patterns. The peak powers out of **S1**, **M2**, and **B1** are in the range of several hundred milliwatts, while the minimum is always less than 200 μW; this results in a peak-to-valley ratio of greater than three orders of magnitude. In contrast, the extrema of the output power for lasers **M1** and **M4** are much closer together, differing by a factor of ~30 at most. The general shape of the plots for **S1**, **M2**, and **B1** in Fig. 3.5.4 are also similar, but those from **M1** and **M4** have the opposite curvature.

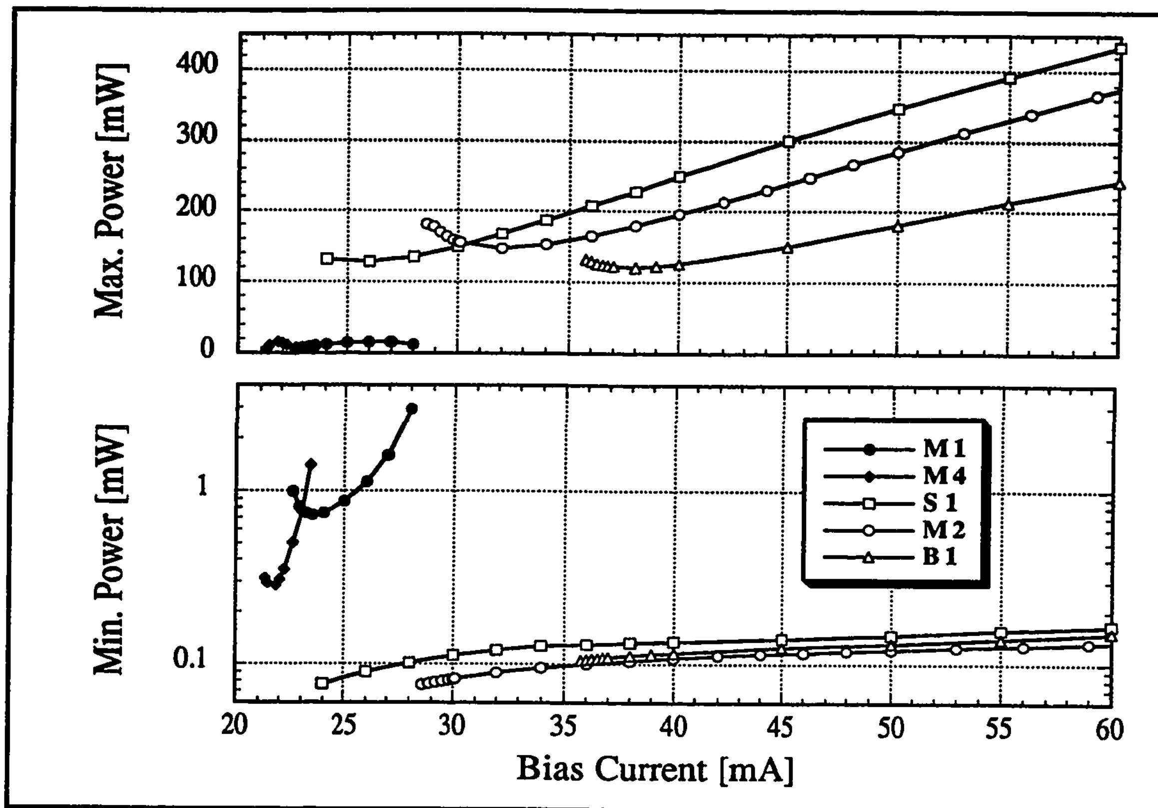

Figure 3.5.4: Extrema of the Output Power During Self-Pulsations
The maximum (top) and minimum (bottom) output powers from facet #1 are plotted as a function of bias current, for lasers **M1**, **M4**, **S1**, **M2**, and **B1**.

The differences in the self-pulsing frequencies and power extrema, along with the bias current ranges over which they occur, seem to indicate that perhaps there are (at least) two different oscillation modes that can be generated in non-uniformly pumped lasers. Lasers **M1** and **M4** produce relatively "shallow" oscillations over a narrow range of bias currents near threshold. In contrast, the other devices simulated generate much sharper pulses which do not cease when the bias is raised substantially above threshold.

The results of the simulations, then, indicate that there are three basic types of behaviour exhibited by two-section semiconductor lasers, as far as their stability is concerned. An example of the first type would be the $I_2 = 0$ curves in Fig 3.4.1, where

the device operates much like a uniformly biased laser (i.e. stable for all current biases). In the second case the oscillations appear as a modulation of the continuously lasing output, as shown in Fig. 3.5.1 for laser **M1**. For this type the range of biases for which self-sustained pulsations occur is confined to a small range of biases close to threshold, as demonstrated by the *L-I* in Fig 3.4.4. In the third case, such as the $I_l = 0$ simulation shown in Fig. 3.4.8, the laser behaves unstably at all biases above threshold. In this mode of operation giant optical pulses are generated as lasing is alternately quenched and re-established. In addition to these temporal stability considerations, the *L-I* characteristic either may or may not exhibit bistability, and during the on-portion of this hysteresis loop it either may (e.g. Fig. 3.4.8) or may not (e.g. Fig. 3.4.4, $I_l = 0$ mA) be self-pulsing.

It is reassuring that the split-contact laser theory of Ueno and Lang[16] also describes these different sorts of laser behaviour. Although their calculations are based on a less comprehensive model, they do predict the three different types of stability we have found in our simulations, as well as the existence of regions in which hysteresis develops. However, their analysis is only able to determine whether a given gain distribution results in a stable or unstable optical output. The advantages of our work, then, lie in the more detail information we can extract. Firstly, our model produces valuable information about the frequency and shape of the pulses, carrier profiles, and spectra. We also explicitly describe the dependence of the optical gain on bias, which is an essential step in relating theory back to measurable device parameters. This is the first analysis of which we are aware that combines all of these factors into a detailed, self-consistent model of split-contact laser operation.

In summary, then, we are able to predict which biases (if any) cause a laser to exhibit self-sustained pulsations, as well as to characterize the pulse frequencies and waveforms that are produced. The effect of different contact geometries and facet

reflectivities on these parameters has also been presented, along with the demonstration and discussion of two distinct types of self-pulsing modes (i.e. variations in a continuously lasing output vs. oscillation between lasing and non-lasing states).

3.6: MODULATED CURRENT SIMULATIONS

3.6.1: Detailed Modulation Examples

In the previous sections of this chapter we have taken care to extract the simulated data at times when the laser bias was held constant, so that we could simulate the steady-state device characteristics. However, because our simulations are generated by solving time-dependent device equations, it is also possible for us to examine the response of the split-contact laser to *changes* in bias. This type of information is essential when we are trying to evaluate the speed performance of the devices, which can be an important factor for many applications. We have therefore performed a series of simulations on structure **M1** (see Appendix C for details) in which we bias the laser with a small signal modulation on top of the average, d.c. current bias.

Figure 3.6.1 shows the simulated laser response to modulations of a particular device bias at three different frequencies. To generate these plots we have selected the bias point (I_1, I_2) = (12 mA, 15 mA); the steady-state operating point for laser **M1** at this bias can be seen in Fig. 3.4.1. Beginning with the device operating in steady state at this bias, we then simulate a 0.5 $mA_{peak\text{-}peak}$ square wave modulation of current I_1 at the desired frequencies. The curves in Fig. 3.6.1 indicate how the model predicts the laser will respond to this input, including the transient behaviour observed at the beginning and end of the modulation.

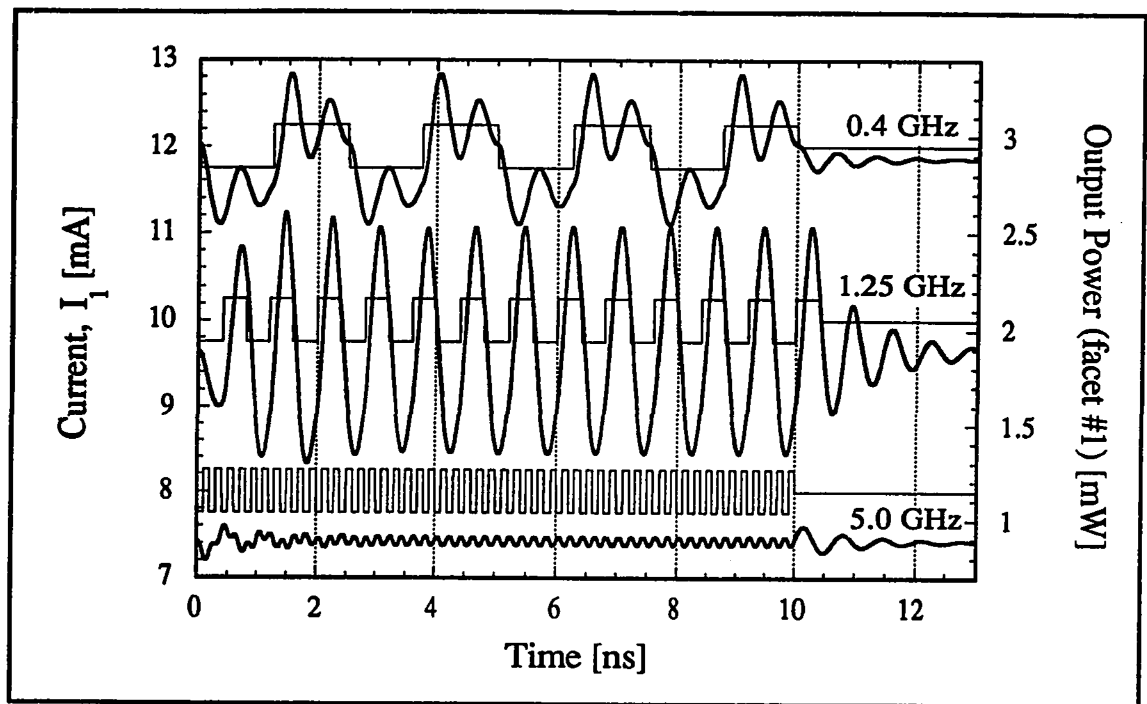

Figure 3.6.1: Temporal Response to Bias Current Modulation
The variations in the output of laser **M1** are shown at modulation frequencies of 0.4, 1.25, and 5.0 GHz. Bias current I_2 is held constant at 15 mA, while the average value $I_1 = 12$ mA is modulated with a small square wave (depth = 0.5 $mA_{peak\text{-}peak}$). The time-average output powers and current levels are actually the same in all three cases: the 1.25 and 5.0 GHz curves have been offset in this plot for clarity.

As Fig. 3.6.1 demonstrates, the response of the laser at a given bias is a strong function of the frequency at which it is modulated. At the relatively low frequency of 0.4 GHz we see that, although the laser output is able to follow the changes in the bias to some extent, there is also a substantial amount of ringing at a frequency of ~1.25 GHz. This represents the resonance frequency of **M1** at this particular bias: this is the frequency at which relaxation oscillations occur whenever the carrier or photon concentrations are perturbed from their steady state values.

Because 1.25 GHz is the "natural" oscillation frequency at the chosen bias point, we see in Fig. 3.6.1 that if we apply an external modulation at this frequency, the depth of modulation is enhanced. The resonance between the relaxation oscillation frequency of the device and the external modulation rate amplifies the effect of the bias modulation on the laser output.

When we modulate the bias at frequencies above resonance (for example, the 5 GHz curves in Fig. 3.6.1) the depth of the variations in the laser output is reduced. Above 1.25 GHz the laser output is not able to respond to the rapid changes in bias as effectively, because the device has become limited by the speed at which the photon concentration in the cavity can build up and drop off. Figure 3.6.1 also indicates that at 5 GHz it takes ~2 ns for the output frequency to "lock on" to the external modulation: initially the device tends to operate at the resonance frequency of 1.25 GHz. Similarly, when the modulation ceases (at $t = 10$ ns), the output frequency reverts back to that of the intrinsic relaxation oscillations.

3.6.2: General Modulation Characterizations

Although Fig. 3.6.1 provides specific examples of the laser response to a modulated current input, it would take a large number of similar plots to give a complete description of the split-contact laser modulation characteristics. We have therefore attempted to summarize the results of our simulations in Fig. 3.6.2, where the modulation efficiency (ratio of the peak-to-peak variations in the output power to the variations in bias current) is plotted as a function of frequency. Four bias points have been selected from the $I_2 = 15$ mA *L-I* curve in Fig. 3.4.1, so that we can observe the effect of the d.c. bias level on the modulation response. It should be noted that although we have only plotted the results for facet #1 in Fig. 3.6.2, the output from facet #2 is quite similar.

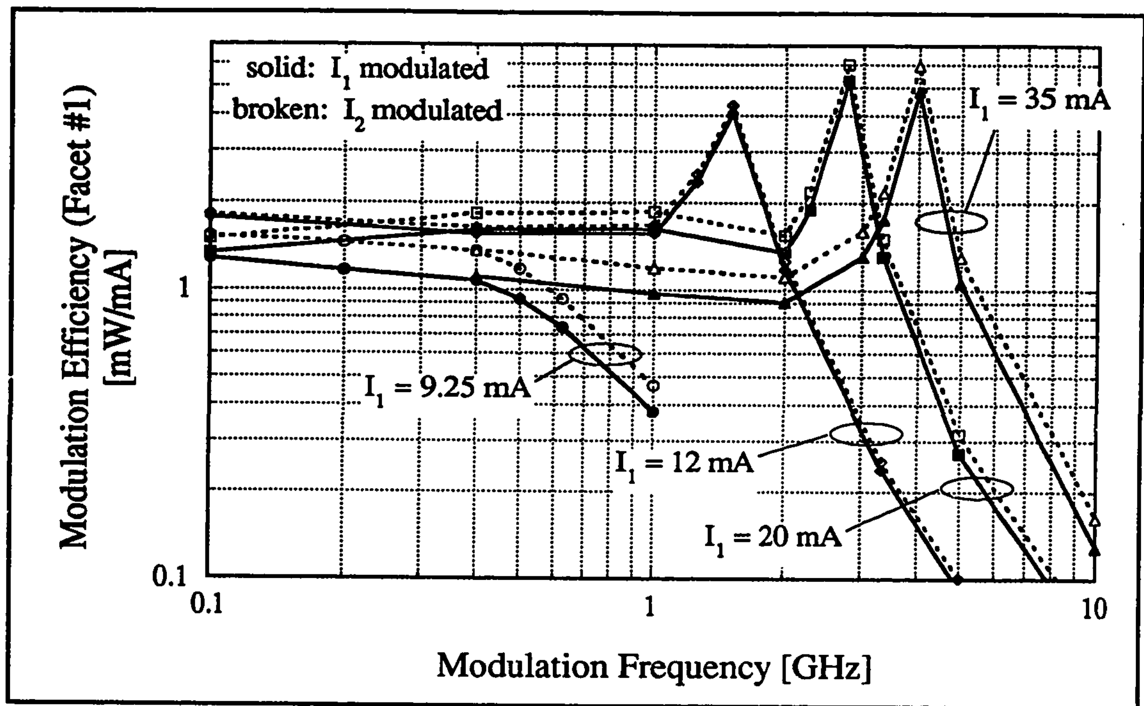

Figure 3.6.2: Simulated Modulation Efficiency vs. Frequency
The modulation efficiency is plotted vs. frequency for device **M1**, with bias levels I_2 = 15 mA and I_1 = 9.25, 12, 20, and 35 mA. This bias is modulated by a small-signal square wave with a strength ΔI = 0.5 mA_{pp}.[a]

The general shape of the curves in Fig. 3.6.2 is what one might expect from the standard modulation theory of uniformly pumped lasers:[17] The response is a plateau at low frequencies, ending in a peak at the relaxation oscillation frequency of the laser. Above this resonance the modulation efficiency drops off with an approximately ν^{-2} dependence. Our simulations also show that the height and frequency of the resonance peak increase with the laser bias current. This is because at greater bias currents the material gain in the active region is stronger, which in turn means that the photon flux can respond more quickly to the modulating signal. The frequencies at which the peak occurs (hundreds of megahertz to

[a] Additional simulations have indicated that the modulation efficiency does not vary with the size of the current variations, for $\Delta I \leq 2$ mA_{pp}.

a few gigahertz), are also in line with what previous work in laser modulation has indicated for semiconductor lasers.[18]

In addition to these basic points, which are not original to our model but serve to support its validity at high speeds of operation, there are also several features in Fig. 3.6.2 that are specific to non-uniformly pumped lasers. Firstly we note that at a given d.c. bias and frequency, the efficiency for modulation of I_2 is consistently higher than for I_1. Although this difference is not great (dP_1/dI_2 is from 100% to 120% of dP_1/dI_1), it is evident in all of our simulations. This result is due to the fact that contact #2 is less than half as long as #1 ($L_1 = 350\ \mu m$, while $L_2 = 150\ \mu m$), so that for the same modulation level of the bias currents, the variations in the current *density* under contact #2 are proportionally larger. This effect is partially offset by the fact that light passing along the length of the laser spends a smaller fraction of its time in section #2 (the region where the modulations of the current density are strongest), so that the ratio of the modulation efficiencies does not attain the same ratio as the contact lengths.

A close examination of the appropriate *L-I* curve in Fig. 3.4.1 reveals that there is a discontinuity in the output power of device **M1** at $(I_1, I_2) = (9.25\ mA,\ 15\ mA)$. This point was therefore selected for a modulation simulation: the $I_1 = 9.25\ mA$ curves in Fig. 3.6.2 give an indication of the speed at we can switch the absorbing portion of the split-contact laser between the saturated and unsaturated states. This curve reveals no evidence of a resonance peak, and the response begins to drop off rapidly at a frequency of ~400 MHz. This relatively low cut-off frequency is not entirely unexpected, however, considering that we are operating the laser at threshold.

If we consider modulation frequencies below the cut-off, the large slope of the *L-I* curve at the discontinuity might lead one to expect the modulation efficiency to be higher at this point than in the linear region above threshold. The simulations, however, indicate that

even down to 100 MHz the response is, at best, equal to the higher bias levels. Evidently, the speed at which the absorption can switch from saturated to unsaturated in this type of device is low, at least compared to operation substantially above threshold. This would seem to indicate that electrical switching of the split-contact laser between its on- and off-states is not likely to be practical above ~100 MHz.

3.7: NON-UNIFORM OPTICALLY PUMPED LASER SIMULATIONS

3.7.1: Introduction

In our discussion thus far we have considered semiconductor lasers in which non-uniform pumping is achieved by dividing the top laser contact into multiple sections. Although this is an important application of the theory presented in Chapter 2, it is not the only means of varying the carrier injection along the length of the active region. Our model is also suitable for describing such devices as amplifiers or optically controlled switching devices, in which carrier generation is due, at least in part, to external photon injection through the facet(s) of the device.[a] This produces non-uniform pumping because light enters the laser active region at two distinct points (the facets), as opposed to illuminating the length of the device evenly.

When biasing the device electrically, the parameters we have at our disposal are the electric currents through the device contacts, which can be functions of time. In the optically pumped case, there is an extra degree of freedom involved: we can set the intensity and cavity mode number (i.e. the wavelength) of the light incident on each facet. The large number of variables involved here makes it impractical to give a comprehensive

---

[a] Optical injection is accounted for by the $S^{+}_{me}(t)$ and $S^{-}_{me}(t)$ terms in eqs. (2.5.10) and (2.5.11).

summary of all possible optical pumping configurations, even for a single device structure with fixed electrical bias. Instead, we simply present a series of examples that illustrate the results of the simulations, indicating the more intriguing features and potential applications of optical pumping in semiconductor lasers. The simulation parameters have not necessarily been optimized to maximize these effects, but they do demonstrate some possible types of device behaviour.

In this section we describe a combination of non-uniform electrical (via the split-electrode, as discussed in Sections 3.4 through 3.6) and optical pumping. The simulations begin with the laser biased at a particular point on one of the d.c. *L-I* curves presented in Section 3.4, and then add in an optical signal. Subsections 3.7.2 through 3.7.4 cover the three cases of unistable, bistable, and unstable operation.

3.7.2: Operation in the Unistable Regime

We begin by considering laser **M1** (the structure is described in Appendix C) with $I_1 = 30$ mA and $I_2 = 0$. As Fig. 3.4.1 illustrates, this operating point lies well above threshold, in the linear, unistable portion of the *L-I* characteristic. In Fig. 3.7.1 we show an example of the temporal response of this laser, in this case to a 1 ns wide pulse of light consisting of 1 mW of power incident on facet #1. We have chosen to pump mode #7 for this simulation[a] because this is the dominant lasing mode at the chosen bias when the device receives no external illumination (see Fig. 3.4.2).

As we can see, the incident light causes a large transient response, both when it begins and ends, but the on-transient settles down to a steady state level in less than 1 ns. Although this on-level is quite close to the unilluminated output, we are operating at an

[a] In this simulation, as in the others that follow, we assume that, except for a reflective loss at the facet, all of the incident light is coupled into a single optical mode of the laser cavity.

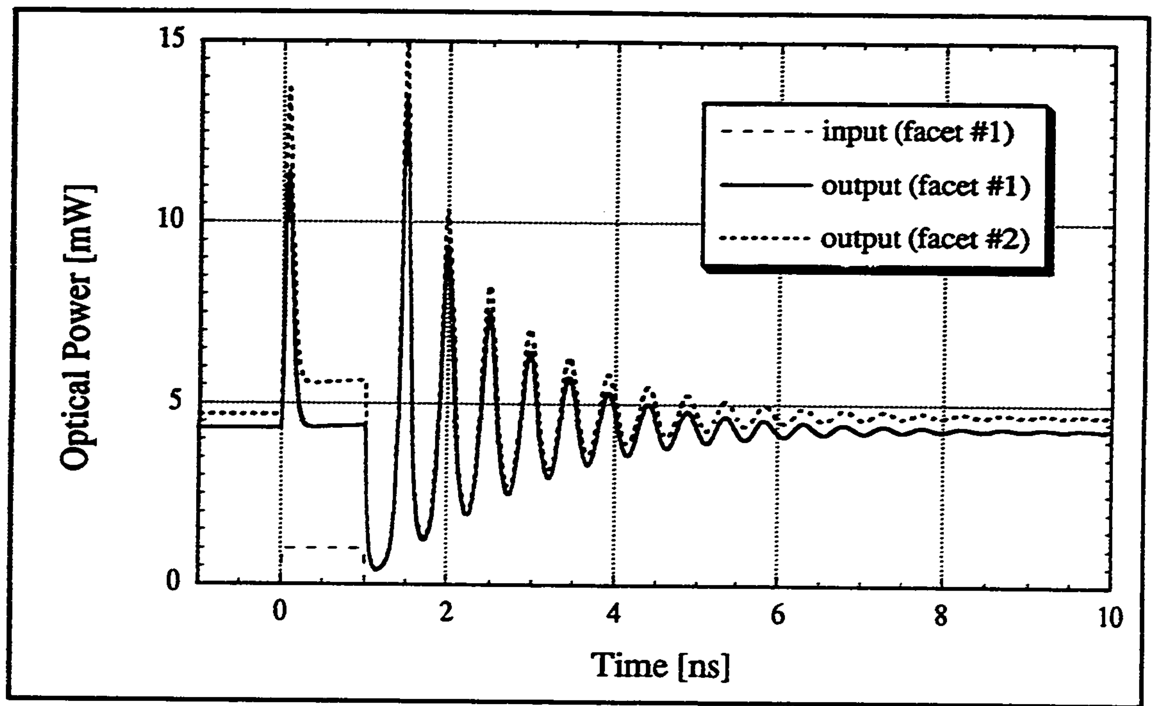

Figure 3.7.1: Temporal Response to an Incident Optical Pulse
The simulated laser response to a 1 mW, 1 ns optical pulse incident on facet #1 is shown as a function of time. The electrical bias is $I_1 = 30$ mA, $I_2 = 0$.

electrical bias 10 mA above threshold ($I_1 \sim 1.5 I_{th}$). We would therefore not expect a 1 mW optical signal to cause as large a relative change in the output power as when the current bias is near threshold. The more interesting effects of the optical illumination cannot be observed in response curves in Fig. 3.7.1, but become apparent when we examine the spectra of the laser.

Figure 3.7.2 shows the spectral output of laser **M1** with no optical input (solid curve, filled squares), and with various levels of incident illumination. The unpumped and 1 mW curves correspond to t = -0.01 ns and 0.99 ns, respectively in Fig. 3.7.1; the time response for the other power levels is not shown. Figure 3.7.2 demonstrates that the

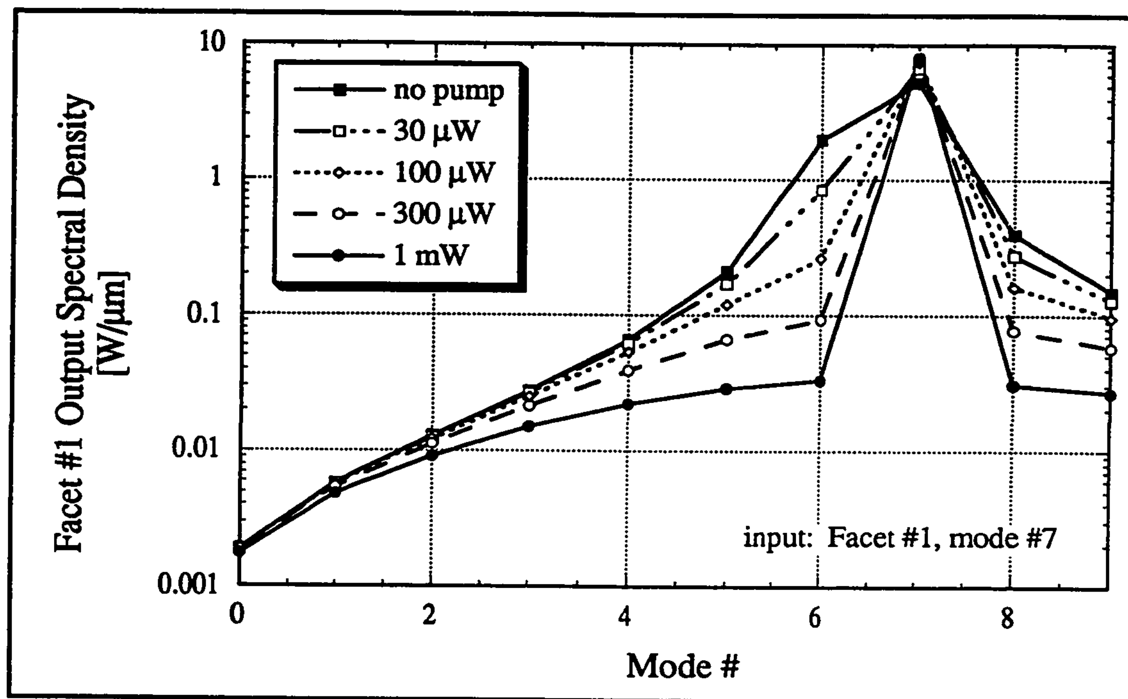

Figure 3.7.2: Laser Spectra, Varying Incident Optical Power
The simulated output spectra of **M1** with $I_1 = 30$ mA and $I_2 = 0$ are plotted after the laser reaches steady state, for optical pumping powers of 0 to 1 mW. The incident light is confined to mode #7, and is incident on facet #1 of the laser.

primary effect of the incident light occurs in the spectra of the laser, as opposed to the total output power. We see that with no illumination the peak lasing mode is #7, which contains ~65% of the power, but there are still significant amounts of power in the nearby modes as well (24% in #6 and 5% in #8). However, when we begin to optically pump the laser (injecting into mode #7 in this case), we begin to see a significant reduction of the side mode power at as little as 30 µW incident power. This trend toward single mode operation continues at least up to an injection level of 1 mW, at which point 97% of the light is in mode #7, with the next strongest mode (#6) having less than 0.5% of the total output power. This simulation clearly indicates that we can improve the single mode behaviour of the laser by injecting a small amount of optical power into the dominant lasing mode.

In fact, we can use an optical input not only to decrease the number of cavity modes that lase, but also to select which mode is the dominant one. Figure 3.7.3 shows a spectral plot similar to Fig. 3.7.2, but in this case we have varied the wavelength of the incident light instead of the power. These simulations show that it is possible to shift the lasing wavelength from its unilluminated value (mode #7) to a mode determined by an external optical source. Pumping modes that are relatively close to #7 (for example, #5 or #9) results in a shift in the lasing mode to match the pump mode, as well as a change from multi- to single-mode operation. In these cases stimulated emission amplifies the external light, which changes the carrier profile in the active region sufficiently to reduce the gain at

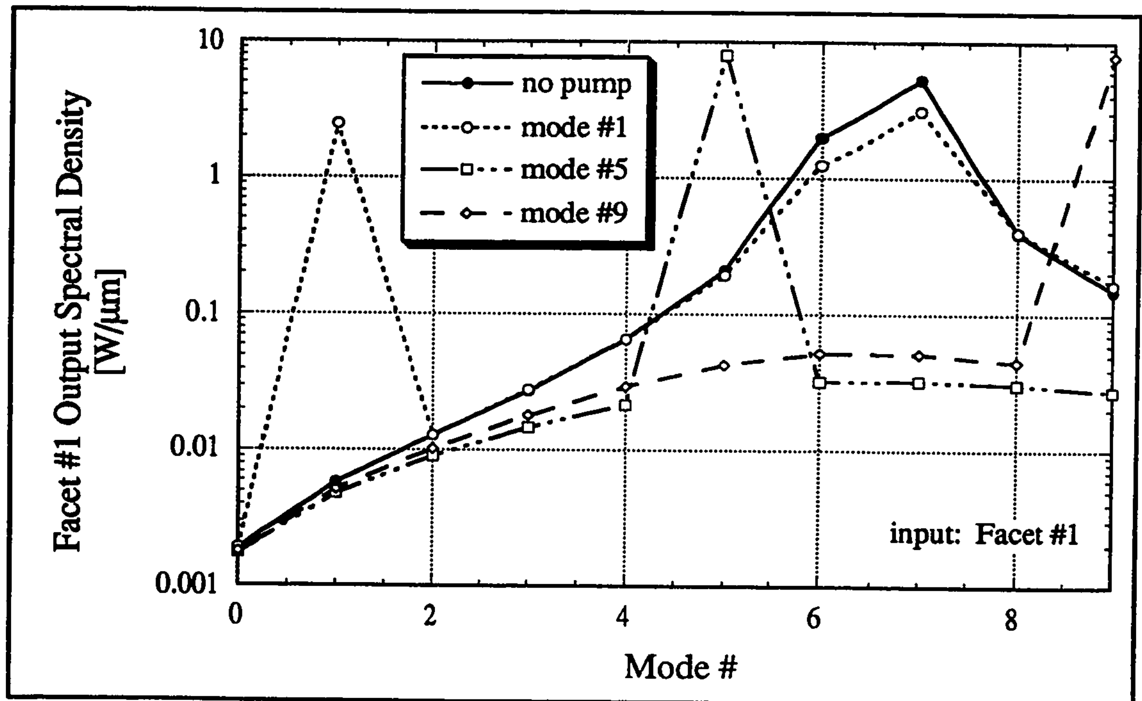

Figure 3.7.3: Laser Spectra, Varying Incident Optical Mode
The simulated output spectra of **M1** with $I_1 = 30$ mA and $I_2 = 0$ are plotted after the laser reaches steady state, for optical pumping of modes #1, #5, and #9. Incident power is 1 mW for each of these cases, and is incident on facet #1 of the laser. The unilluminated spectrum is also shown, for reference.

mode #7.

As the pump signal is moved farther from the unilluminated lasing wavelength (to mode #1 in Fig. 3.7.3), we see that, although a considerable fraction (32%) of the output light is in the pumped mode, lasing also occurs in the modes that dominated the unilluminated spectrum. In this case we are getting amplification of the pump signal, but this stimulated emission does not decrease the gain in modes #6 and 7 enough to quench lasing at those wavelengths.

The simulations presented here, then, suggest the possibility of using non-uniform optical pumping as a means of tuning the split-contact laser (this is similar to the technique of injection locking under direct current modulation, as described in Section 1.3.3). Although the device can be tuned to some extent electrically, as discussed in Sections 3.4 and 3.8, the use of incident light allows for additional, direct optical tuning of the laser, as well as improvements in the power distribution in the output spectra.

3.7.3: Operation in the Bistable Regime

Although optical pumping of a split-contact laser biased in the unistable regime has its applications, if we truly wish to take advantage of the unique features of these lasers we must consider bias configurations in which saturable absorber effects manifest themselves. To begin with we consider the bistable configuration of laser **M1**: the relevant *L-I* for this device was presented in Fig. 3.4.4. We have expanded the region of interest around the bias point b_1, (i.e. $I_1 = 0$ and $I_2 = 20.5$ mA) in Fig. 3.7.4. It should be noted that the laser is not self-pulsing on either branch of this bistable loop.

Bias b_1 in Fig. 3.7.4 represents a bistable state: we can switch the device into the on-state electrically by briefly raising the bias current I_2 to 20.6 mA, or force it off by

lowering I_2 to 20.4 mA. However, as the simulation in Fig. 3.7.5 demonstrates, it is also possible to switch the laser via optical injection. This plot represents an example of all-optical switching of the laser, showing the optical input and output of the laser as a function of time.

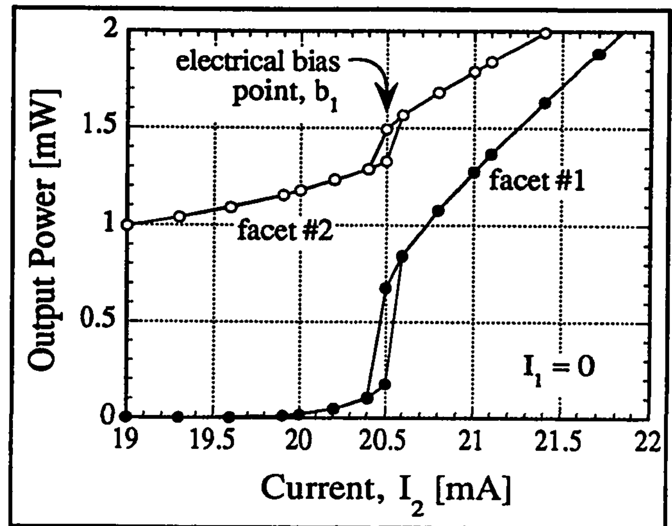

Figure 3.7.4: *L-I* Showing Bistable Region The *L-I* characteristic of **M1** is shown, with the electrical bias point in the bistable region indicated.

Figure 3.7.5 is especially interesting because it shows that we can induce the laser to switch states in either direction by varying only the input pulse power: neither the facet of incidence nor the wavelength need be changed. The mechanism for the switch-on process (initiated by the pulses at $t = 10$ and 50 ns) is fairly straightforward, and is similar to what occurs as the bias current is increased. When the laser in the off-state receives a 1 mW pulse of light into facet #2, the incident light is amplified by stimulated emission in this strongly pumped section. Upon reaching section #1 this light is absorbed, saturating the absorption in that section and allowing the device to lase. Because we are operating inside the hysteresis loop, when the pump signal ceases the laser output settles to the on-state level (this takes approximately 16 ns from the termination of the input pulse).

The manner in which the laser is turned off optically is somewhat less intuitive, as it has no electrical analogue. In this case, beginning with the laser in the on-state we inject an optical pulse similar to that which caused turn-on, but with a greater intensity (the 10 mW

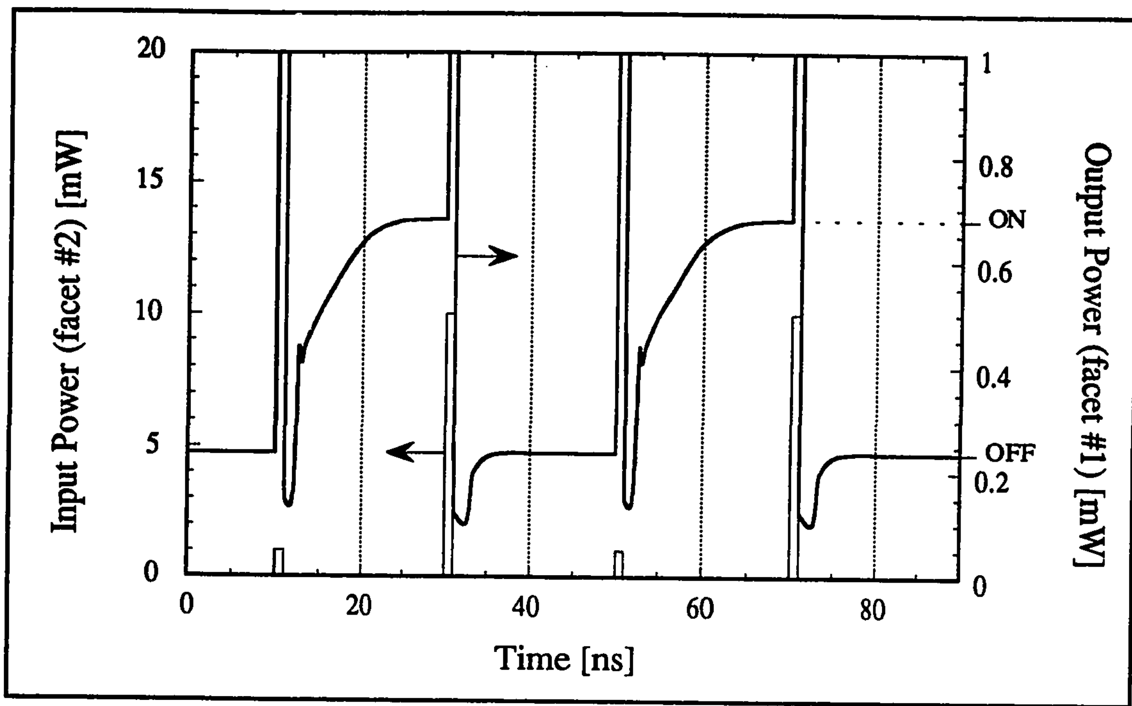

Figure 3.7.5: All-Optical Switching in the Hysteresis Loop
Switching of laser **M1** between the on- and off-states by means of optical pumping is shown. The electrical bias point is b_l. Optical pulses of 1 ns duration, 1 mW peak power, into cavity mode #9, are used to switch the laser on; similar, 10 mW pulses return it to the off-state.

pulses at $t = 30$ and 70 ns in Fig. 3.7.5). Again, this input is amplified in section #2, and saturates the absorption in section #1. However, the transient caused by this incident light pulse is very large (peaking at 60 mW, as opposed to 6.9 mW for the turn-on pulses). This large photon flux depletes the carrier concentration (by stimulated emission) to such an extent that, when the input ends, the laser is "closer" to being off than on. The plot shows that less than 10 ns after the off-pulse ends the laser has reached steady state in the lower branch of the hysteresis loop. The minimum in the optical output that occurs ~1 ns after the end of the off-pulse in Fig. 3.7.5 represents this so-called "gain saturation effect". There is also evidence of a similar drop in the output power after the turn-on pulse, but in this case the gain saturation is not sufficient to switch the laser back off.

At this point we should note one other relevant point pertaining to Fig. 3.7.5. Although we have not shown it in this plot, each size of pulse (either 1 mW or 10 mW) can cause a state change in only one direction. For example, if the laser is in the off-state a 1 mW pulse will turn it on, but if it is already on, a 1 mW input will not switch it back off. Similarly, a 10 mW input is only able to cause a shift from the on- to the off-state.

The simulation shown in Fig. 3.7.5 raises the question "How much power is needed in the input pulse to cause the laser to change state?" Figure 3.7.6 summarizes the results of a series of simulations performed to answer this, in which we keep all of the

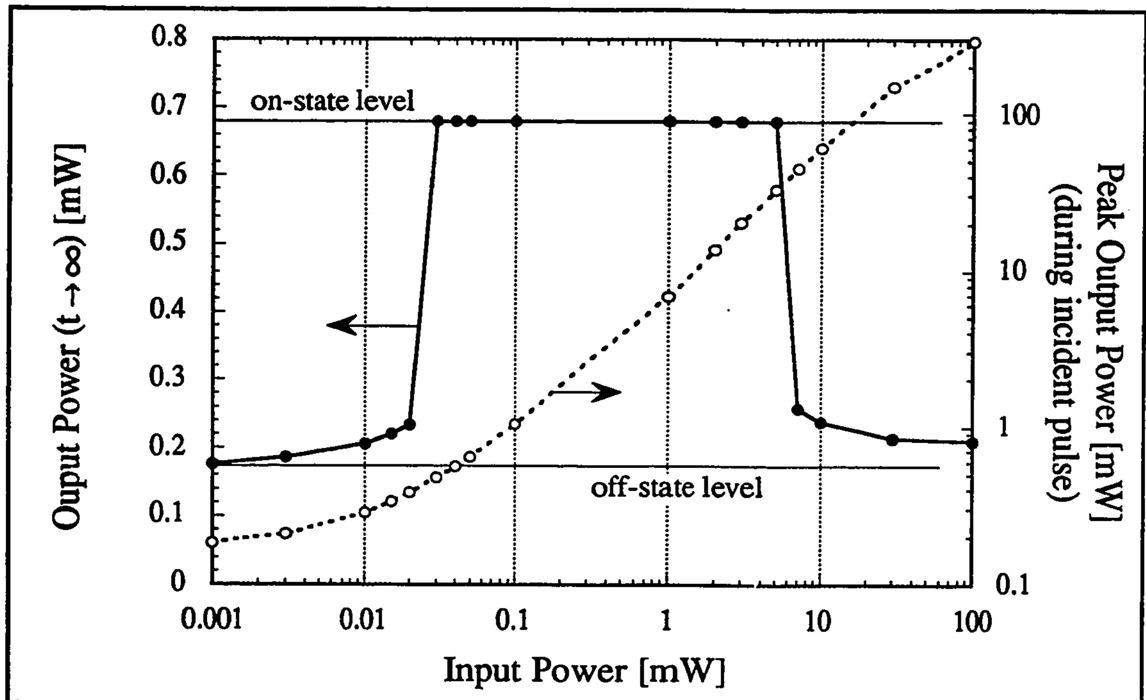

Figure 3.7.6: Laser Output vs. Incident Pulse Power

The steady-state (after the input pulse ends) and peak (during the input pulse) optical output powers from laser **M1** (biased at b_1) are plotted vs. the incident pulse power. The steady-state off- and on-levels are also indicated, and should be read from the left-hand axis. As in Fig. 3.7.5, the input pulses were directed into cavity mode #9 through facet #2, and were 1 ns in duration.

device parameters except for the input pulse power constant.

In terms of their ability to switch the laser state, the steady-state output power curve in Fig. 3.7.6 (solid line, filled circles) shows that the incident pulse powers fall into three distinct regions. For low powers (< 30 μW) the optical pump is not sufficient to switch the laser from the off- to the on-state, although a slight rise in the level of the off-state is indicated at the upper end of this region. This range of input powers has no effect when the device is already in the on-state either: the light levels are simply to weak to have a significant effect on the laser. In the second region, where the input powers range from 30 μW to 5 mW, the optical input saturates the absorption in the unpumped section, switching the device from off to on. This is the range that the pulses at t = 10 ns and 50 ns in Fig. 3.7.5 fall into: they are capable of switching the laser on if is initially off, but not vice versa. Finally, for input powers greater than 5 mW an incident pulse results in the final state of the laser being on.

The broken curve in Fig. 3.7.6 shows the dependence of the peak output power (during the pump pulse) on the incident power: this maximum occurs shortly after the start of the incident pulse, and is off-scale in Fig. 3.7.5. Unlike the steady-state output power, this peak level increases monotonicly with the input (the laser is functioning as an optical amplifier). In order to minimize the effect of this large surge in the laser output, which could be detrimental if the device were to be used for optical memory applications, it would be desirable to work at the lower limit of the available switching ranges. For instance, if we use a 30 μW pulse to turn the laser on, the peak output power during the pulse of 0.47 mW, which is less than the on-state power, 0.68 mW. The minimum power that is capable of switching the device off is 7 mW, which yields a 45 mW peak output. Unfortunately, the settling time until steady-state is reached and the minimum input pulse width capable of causing switching both increase as the input power is reduced, so that a

trade-off between minimizing the size of the on-transient and maximizing the device speed is encountered.

At this point a few words about the switching speeds of the laser appear to be in order. From Fig. 3.7.5 the optical turn-on time for this device is ~16 ns, while turn-off takes ~8 ns. A similar simulation (not shown) in which switching is achieved electrically (by raising I_2 to 21 mA to turn the laser on, and reducing it to 20 mA for turn-off) indicates switch-on and -off times of ~11 ns and ~75 ns, respectively. Although the electrical and optical turn-on times are similar, we notice that turn-off can be achieved much more rapidly optically than by varying the bias current. The reason for this difference seems to be related to the speed at which carriers can be extracted from the saturated absorber. In electrical switching we must either extract the carriers out through the device contacts (which is only possible if the junction is reverse biased), or wait for relatively slow recombination processes to deplete the population. The gain saturation which causes the optically induced turn-off is a much faster mechanism, because carrier depopulation is achieved through the stimulated emission of a very large photon density. Note that although the electrical switching times could probably be improved by optimizing the levels of the bias currents used in switching, the relative slowness of this type of switching is not unique to our simulations.[19]

3.7.4: Operation in the Self-Pulsing Regime

The self-pulsing regime of operation is the final one for which we wish to consider the effects of optical pumping. We have characterized the biases and resulting self-pulsing waveforms of several device structures in Sections 3.4 and 3.5; the *L-I* from one of these (laser **B1**) has been expanded in the region of interest in Fig. 3.7.7. For the following simulation, the electrical bias is held constant at the point b_2 ($I_1 = 0$, $I_2 = 36$ mA). This

bias point, like b_1 in Fig. 3.7.4, is inside the hysteresis region; the difference in this case is that on the upper (but not the lower) segment of this loop, the device is generating self-sustained pulsations.

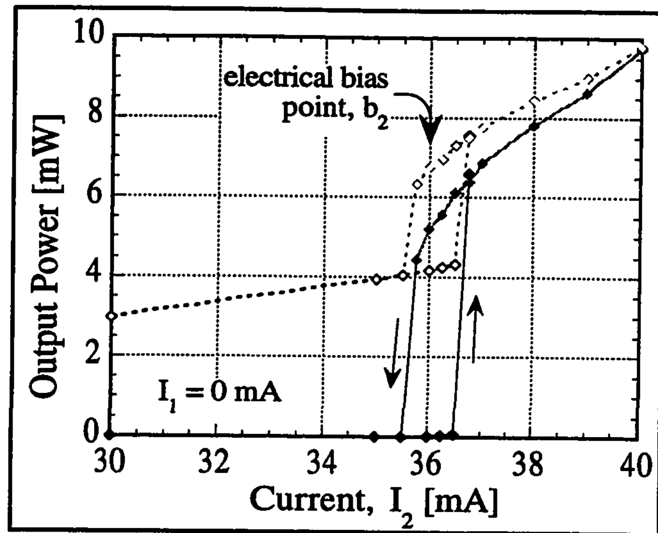

Figure 3.7.7: *L-I* Showing Self-Pulsing Region

The *L-I* characteristic of **B1** is shown, with the electrical bias point, b_2, in the self-pulsing region indicated. In the more lightly shaded regions of the curves the laser is generating self-sustained pulsations.

Figure 3.7.8 shows that the behaviour of **B1** under the influence of an optical input is considerably different from what we previously observed for laser **M1** (in Section 3.7.3). For this simulation we have started the device in the off-state, and plotted the response to a series of optical inputs as function of time. The optical pulses are 20 ns in duration, 1 mW in height, and couple through facet #2 into mode #7. The first optical pulse (at $t = 0$) increases the optical output to ~5 mW, but after the initial transient the laser output becomes stable. When the input light is switched off, however, the laser switches fully into the on, self-pulsing state. The second input pulse ($20 \text{ ns} \le t \le 30 \text{ ns}$) does not switch the laser between the branches of the hysteresis loop, but it does quench the self-pulsing behaviour for the duration of the incident light; the laser then returns to the normal on-state when the input ceases.

Figure 3.7.8 is interesting in that it suggests the possibility of utilizing a split-contact laser for optically controlled pulse generation. A signal as small as 1 mW can be

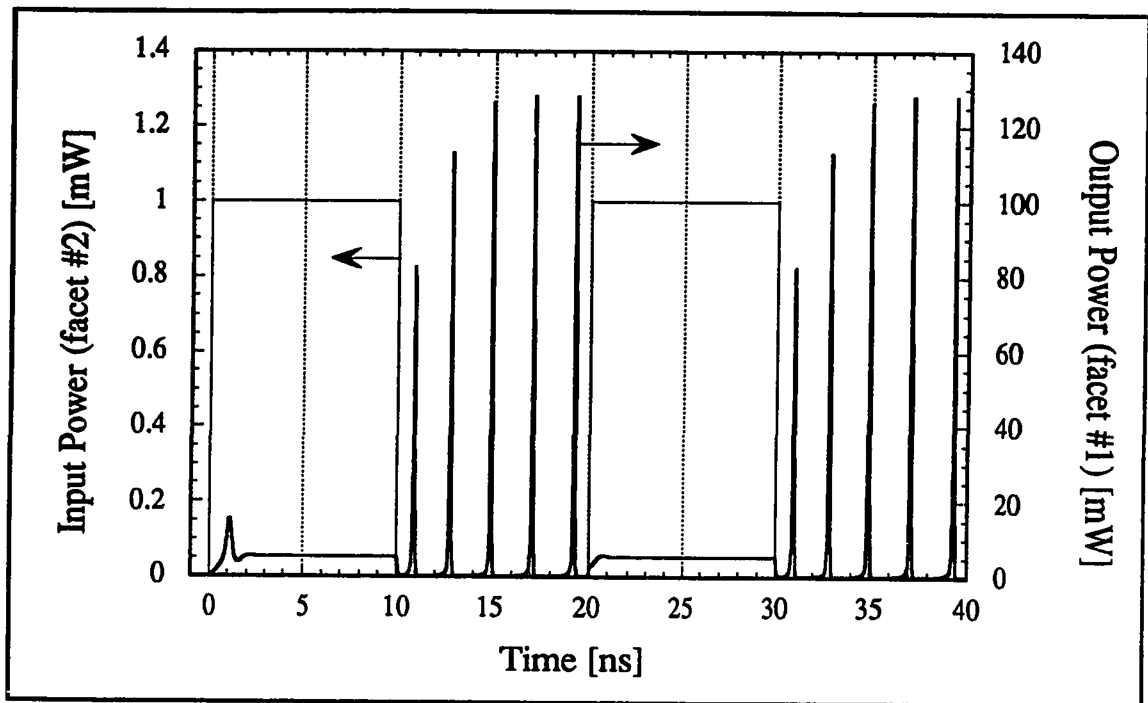

Figure 3.7.8: Optical Pumping with Self-Pulsations

The temporal response of laser **B1** (at bias b_2) is plotted, showing the effect of optical pumping on the self-pulsing behaviour. The incident light is coupled into mode #7.

used to switch the laser output from an approximately 5 mW d.c. level to a 0.5 GHz pulsed output with a peak power of 120 mW. The time scale on which we can control the laser output is comparable to the self-pulsing period. This simulation indicates that the device would be well suited to applications involving the generation of binary, digital optical signals, especially if optical control is required or beneficial.

3.8: Tuning Due to Refractive Index Changes

One of the simplifications that we made earlier in order to obtain a solvable set of equations was that the real part of the index of refraction, n_r, did not vary with the device bias. Since we somewhat arbitrarily chose a static model of the cavity mode spectrum (see

Section 3.2.2), even if changes in the refractive index had been calculated they would not have affected the simulated laser output. However, because it has been demonstrated that variations in n_r can significantly affect split-contact laser spectra,[20,21] it would be beneficial if we could extract some information about this tuning mechanism from our simulations.

We can, in fact, use our model to estimate the effect of variations in the index of refraction on the output of a non-uniformly biased laser, by utilizing the relatively detailed gain calculations described in Section 2.4. It has been established that the real and imaginary parts of a complex variable such as the index of refraction ($n_c = n_r + \mathrm{i}\, n_i$) are related by a set of equations known as the Kramer-Kronig relations. Since n_i can be calculated from the gain, G_m, we can use this relationship to calculate the function $n_r(n,\lambda)$. The details of the mathematics describing this process are given in Appendix B.

Figure 3.8.1 shows a sample plot of the complex refractive index for a 1.3 μm InGaAsP quaternary, as calculated using the method described above. The range of wavelengths used covers the 10 cavity modes that we have considered in our model (see Section 3.2.2). We see that although n_i can vary significantly with wavelength (it is proportional to λG_m), n_r is nearly constant at a fixed carrier density (the difference between n_r and its equilibrium value varies by less than 3% over the wavelength range of interest).

Of more interest to us, however, is the dependence of n_r on carrier concentration, which determines the wavelength shift that the cavity modes experience. As expected, Fig. 3.8.1 indicates that n_r decreases with increasing carrier density: an analysis of the data reveals that at $n = 10^{18}$ cm^{-3} the rate of change is $\frac{\partial n_r}{\partial n} \sim -3.4\times10^{-19}$ cm^3.

This refractive index data that we obtained through the Kramer-Kronig relations can be combined with the carrier concentrations from our previous laser simulations to

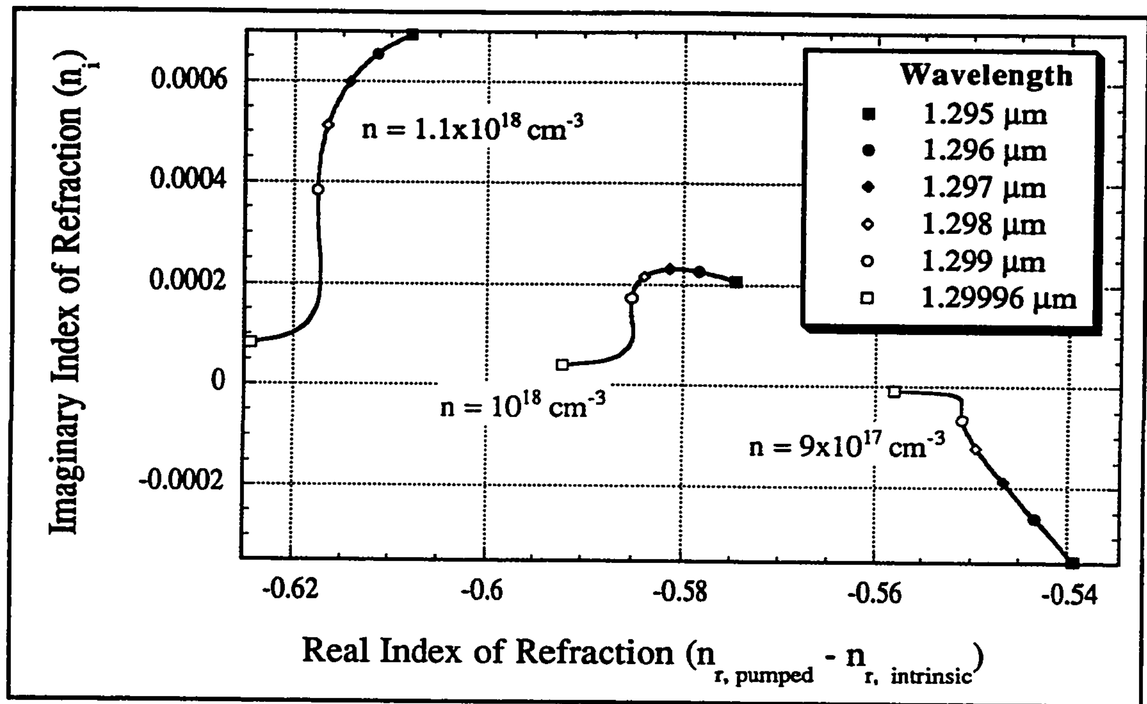

Figure 3.8.1: The Complex Index of Refraction

The index of refraction is plotted in the complex plane at a series of wavelengths, for three values of the active region carrier density. The real part of the index is given relative to the value under zero bias.

determine the wavelength shift that we expect the cavity modes to experience. It is straightforward to show that the change in the wavelength of each mode is given by

$$\delta\lambda_m \approx \frac{\Delta n_r}{n_r}\lambda_m \tag{3.8.1}$$

where Δn_r is the change in the real part of the refractive index. Since we can calculate $n_r(n)$, if we know the range of carrier densities that a given laser experiences, we can determine $\delta\lambda_m$.

To understand the sorts of shifts predicted by this model we first consider the curves in Fig. 3.4.6, which shows the constant output power contours for laser **M1**. As explained in Section 3.4, as we vary the bias along one of these contours the output power from the laser does not vary, but the lasing wavelength may. In order to determine how the refractive index changes along these constant power contours, we have summarized the corresponding carrier concentration data in Table 3.8.1. Although these variations in n are only on the order of 10^{16} cm^{-3}, they are large compared to those that occur during uniform pumping: the simulation in Section 3.3 yields a variation in the carrier density of only ~$2\text{x}10^{14}$ cm^{-3} for output powers between 1 and 8 mW.

Output Power [mW]	Carrier Density Variation [10^{16} cm^{-3}]
1.0	2.47
2.0	1.83
5.0	1.69
8.0	1.52

Table 3.8.1: Laser M1 Output Powers and Carrier Density Variations

We can use the data in Table 3.8.1, together with eq. (3.8.1) and our knowledge of the real index of refraction, to determine the variation of the position of a mode caused by changes in the refractive index. These wavelength shifts are plotted in Fig. 3.8.2, where we see that the model predicts that continuous shifts of up to 33 Å can be obtained without having to vary the output power of the laser. The tuning range is largest for low output power, although there is still a 20 Å range with an output power of 8 mW. This is due to the fact that variations in the carrier concentration are greatest close to threshold, where the non-uniform pumping effects are strongest.

It should be noted that the method we have outlined here to calculate this wavelength shift is not strictly self-consistent. To perform a proper calculation it would be necessary to feed these wavelength shifts back into the main simulation algorithm, to determine new values of the centre cavity mode wavelengths (the λ_m's in Fig. 3.2.1).

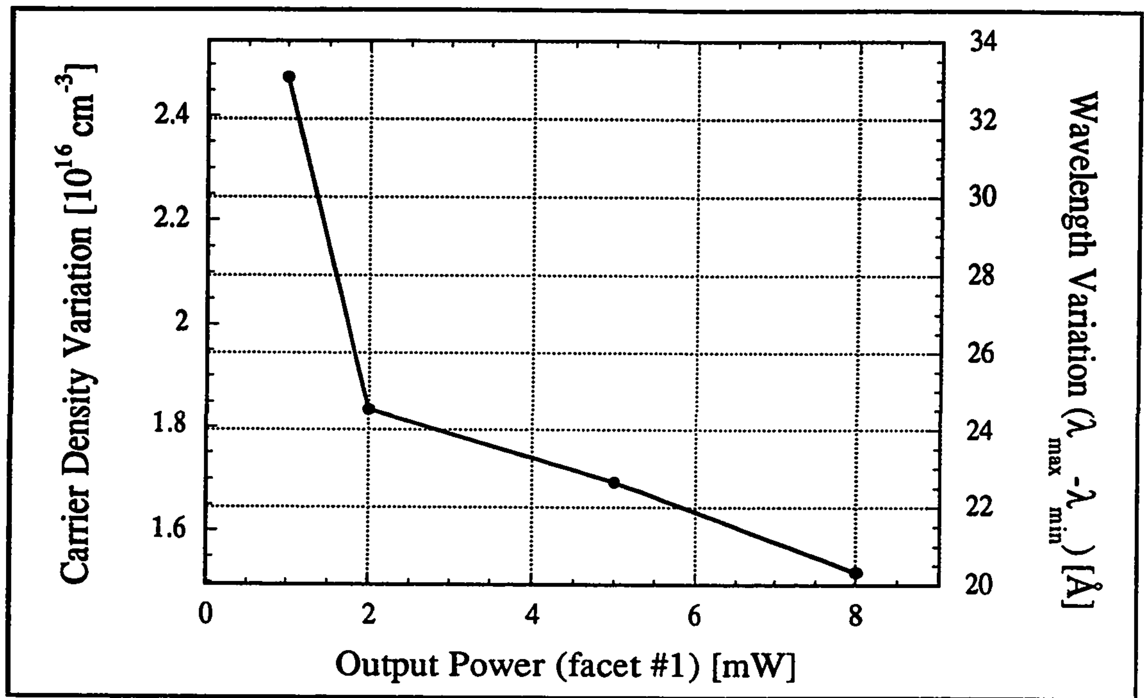

Figure 3.8.2: Carrier Density & Wavelength Variations vs. Output Power
The total amount of variation in the carrier density (n_{max}-n_{min}) and wavelength (λ_{max}-λ_{min}) along the constant power contours in Fig. 3.4.6 are plotted vs. the output power for laser **M1**.

Successive iterations could then be performed until self-consistent results were obtained, so that the position of each mode was tracked as the simulation progressed. Unfortunately, these iterations would have to be performed at each time simulated, and would seriously reduce the speed at which our simulations could be accomplished. For this reason Fig. 3.8.2 has been produced using the "simple" calculation method, in which the mode shifts are not fed back into the laser simulation.

It is also important to keep in mind that these simple calculations of the wavelength shift apply to specific modes of the laser cavity, and do not necessarily correspond to the change we expect in the lasing wavelength. Figure 3.8.2 implies that we can expect shifts in the wavelength of the cavity modes on the order of tens of Angstroms at a given power

level, but we must remember that the free spectral range of laser **M1** is only ~5 Å. In a real device, this would mean that as we try to tune the laser using the index of refraction, the cavity mode at which the gain peak occurs will change once we have shifted the lasing wavelength by at most 5 Å. The resulting mode hopping will limit the practical tuning range of the lasing output to approximately the free spectral range of the Fabry-Perot cavity.[a] Note that if the longer, self-consistent technique outlined in the previous paragraph were used, this phenomenon would be incorporated directly into the simulations.

The free spectral range limit on the tuning wavelength could, under some circumstances, be lifted, because of the other tuning mechanisms that occur simultaneously with the changing index of refraction. We have already seen in Section 3.4 that changes in the gain peak can affect the output wavelength of a split-electrode laser. If this gain shift can be correlated with the changing refractive index shift, it would be possible to reduce mode hopping by shifting the cavity mode and the gain peak together. (However, we must note that if these two mechanisms were to act in opposite directions, the tuning range would be decreased.) Since other mechanisms such as heating effects can also affect the laser spectrum, it is expected that the combination of these competing effects will make the lasing wavelength of a real multi-electrode laser a rather complicated function of the bias.

---

[a] Of course, this limitation could be compensated for by introducing a Bragg grating in the laser cavity. This would increase the mode spacing in the laser, and in principle allow us to achieve the full tuning range implied in Fig. 3.8.2.

CHAPTER 3: REFERENCES

[1] Kant, Immanuel, Critique of Pure Reason, London, U.K.: The Guernsey Press Co. Ltd., 1988, p. 165

[2] Pierret, Robert F., Advanced Semiconductor Fundamentals, Don Mills, Ont.: Addison-Wesley Publishing Company, Inc., 1989, p. 121, eq. (4.60)

[3] Suemune, I., Coldren, L.A., Yamanishi, M., and Kan, Y., "Extremely wide modulation bandwidth in a low threshold current strained quantum well lasers", *Appl. Phys. Lett.*, vol. 53, pp. 1378-1380, 1988

[4] Arakawa, Y. and Yariv, A., "Quantum well lasers - gain, spectra, dynamics", *J. Quantum Electron.*, vol. QE-22, pp. 1887-1899, 1986

[5] Verdeyen, Joseph Thomas, Laser Electronics, Second Edition, Englewood Cliffs, New Jersey: Prentice Hall, 1989, Section 9.3.2

[6] Lasher, G.J., "Analysis of a proposed bistable injection laser", *Solid-St. Electron.*, vol. 7, pp. 707-716, 1964

[7] Baoxun, D., "A theory on stability of double-section semiconductor lasers", *IEEE J. Quantum Electron.*, vol. 25, pp. 847-849, 1989

[8] Paradisi, A. and Montrosset, I., "Numerical modeling of bistable laser diodes with saturable absorbers", *IEEE J. Quantum Electron.*, vol. 27, pp. 817-823, 1991

[9] Le Bihan, J., Goujon, J.-M., Auffret, R., and Chawki, M.J., "Theoretical characteristics of a tunable two-electrode Fabry-Perot (TEFP) laser diode", *J. Lightwave Technol.*, vol. 10, pp. 1931-1934, 1992

[10] Lee, C.-H., Shin, S.-Y., and Kang, S.-G., "Perturbation solution of self-pulsing in semiconductor lasers with a saturable absorber", *IEEE J. Quantum Electron.*, vol. 30, pp. 1396-1404, 1994

[11] Marcenac, D.D. and Carroll, J.E., "Distinction between multimoded and singlemoded self-pulsations in DFB lasers", *Electron. Lett.*, vol. 30, pp. 1137-1138, 1994

[12] Farrell, G., Phelan, P., and Hegarty, J., "Selfpulsation operation regime for absorber of twin section laser diode", *Electron. Lett.*, vol. 27, pp. 1403-1404, 1991

[13] Duan, G.-H. and Landais, P., "Self-pulsation in multielectrode distributed feedback lasers", *IEEE Phot. Technol. Lett.*, vol. 7, pp. 278-280, 1995

[14] Simler, Y., Gamelin, J., and Wang, S., "Pulsation stabilization and enhancement in self-pulsating laser diodes", *IEEE Phot. Technol. Lett.*, vol. 4, pp. 329-332, 1992

[15] Barnsley, P., "All-optical clock extraction using two-contact devices", IEE Proc.-J, vol. 140, pp. 325-336, 1993

[16] Ueno, M. and Lang, R., "Conditions for self-sustained pulsation and bistability in semiconductor lasers", *J. Appl. Phys.* vol. 58, pp. 1689-1692, 1985.

[17] Verdeyen, J.T., 1989, op. cit., Section 11.7

[18] Lau, K.Y. and Yariv, A., "Ultra-high speed semiconductor lasers", *IEEE J. Quantum Electron.*, vol. QE-21, pp. 121-138, 1985

[19] Uenohara, H., Kawamura, Y., and Iwamura, H., "Long-wavelength multiple-quantum-welll voltage-controlled bistable laser diodes", *IEEE J. Quantum Electron.*, vol. 31, pp. 2142-2147, 1995

[20] Kameda, T., Mori, H., Onuki, S., Kikugawa, T., Takahashi, Y., Tsuchiya, F., and Nagai, H., "A DBR laser employing passive-section heaters, with 10.8 nm tuning range and 1.6 MHz linewidth", IEEE Photon. Technol. Lett., vol. 5, pp. 608-610, 1993

[21] Eddolls, D.V., Vass, S.J., Ash, R.M., and Park, C.A., "Two-segment multiquantum well lasers with 7 nm tuning range and narrow linewidth", *Electron. Lett.*, vol. 28, pp. 1057-1058, 1992

CHAPTER 4: EXPERIMENTAL RESULTS

That which coheres with the material conditions of experience (sensation), is *real.*

Immanuel Kant, *Critique of Pure Reason*[1]

4.1: INTRODUCTION

In Chapter 2 we developed a model describing the operation of non-uniformly pumped semiconductor lasers, and in Chapter 3 we presented simulations generated from this model. The results appear to be in agreement with what we expect to be possible in device behaviour; the simulations do not violate any fundamental physical laws (such as conservation of energy), and the results have been interpreted in a manner which seems to make intuitive sense. However, aside from being an exercise in abstract reasoning, even a perfectly self-consistent model of a physical system is only of practical use in comparison with observations we make experimentally, of *real* devices in the *real* world. In this chapter, we therefore present the results of an experimental study of non-uniformly pumped lasers.

The first reason for making measurements of real devices is to confirm (or refute) the theory we have developed. If experimental observations contradict our simulations to a large extent, or in any fundamental way (can a saturable absorber really cause optical bistability in a laser?), then it will be necessary to re-examine the model. In general, discrepancies may be due to three factors: either the actual measurements (or the interpretation thereof) are somehow faulty, or our physical model is somehow inappropriate (as would be the case if we tried to describe the non-uniformly pumped laser physics by the time-independent equations described in Section 2.5.2), or we have made approximations that do not accurately describe reality. While the first possibility can be a

source of error, it does not reflect directly on the validity of our theoretical work. When it appears, the second problem is a rather fundamental one, as it generally invalidates the entire framework on which the simulations are based. The third tends to be more a matter of degree: since we know what approximations we made in developing our model, a comparison of the discrepancies between theory and practice allows us to judge the validity of these assumptions.

The second reason for an experimental investigation of non-uniformly pumped semiconductor lasers is simply to gain an empirical understanding that will aid future device design. Although a model allows us to investigate the devices on a theoretical level, in many cases we are more interested in designing devices for a particular practical application. While our model may aid us in this regard, it is often more expedient to carry out an empirical investigation of a series of devices. When we are merely trying to optimize some device parameter(s) for a given application, this approach allows us to avoid the difficulties involved in constructing a quantitatively accurate theoretical representation.

4.2: Device Growth & Fabrication

A series of InGaAsP/InP, ridge-waveguide, multi-quantum well lasers were grown, fabricated, and mounted, in order to study split-contact devices in an empirical manner. The layer structure of the lasers used in this work is depicted in Table 4.2.1. These devices were grown by metal-organic chemical vapour deposition (MOCVD) at Nortel Technologies (formerly Bell-Northern Research) in Ottawa, Ontario.

The devices were processed as "standard" ridge waveguide semiconductor lasers, except that one, two, or three separate contacts were formed on the top of the waveguide ridge. Individual devices were fabricated by a combination of reactive ion and wet

Layer Name	Material	Thickness	Dopant	Dopant Level [cm^{-3}]
cap	InGaAs	0.2 μm	Zn	10^{19}
buffer	InP	1.6 μm	Zn	10^{18}
buffer	InP	0.2 μm	Zn	$4x10^{17}$
etch stop	Q (1.3)	30 Å	Zn	$4x10^{17}$
grinsch	InP	0.1 μm	Zn	$4x10^{17}$
grinsch	Q (1.0)	200 Å	Zn	$4x10^{17}$
grinsch	Q (1.1)	200 Å	Zn	$4x10^{17}$
active region	Q (1.3)	35 Å	none	
barrier	Q (1.1)	100 Å	Zn	$8x10^{17}$
active region	Q (1.3)	35 Å	none	
barrier	Q (1.1)	100 Å	Zn	$8x10^{17}$
8 additional wells (& 7 barriers) for a total of 12 wells				
active region	Q (1.3)	35 Å	none	
barrier	Q (1.1)	100 Å	Zn	$8x10^{17}$
active region	Q (1.3)	35 Å	none	
grinsch	Q (1.1)	200 Å	Si	$4x10^{17}$
grinsch	Q (1.0)	200 Å	Si	$4x10^{17}$
buffer	InP	1.5 μm	Si	$2x10^{18}$
substrate	InP	500 μm	S	

Table 4.2.1: Nominal Laser Wafer Structure

The layers of the laser structure are identified. Q (λ) represents lattice matched InGaAsP quaternary, with an emission wavelength of λ (in μm).

chemical etching to form ridges 2 μm wide and 2 μm deep. The mask allowed these ridges to be formed with gaps approximately 2 μm wide, to allow electrical isolation of the different sections of the lasers. SiO_2 sidewall passivation was then deposited, via holes were opened, and the Ti/Pt/Au top contacts were formed. After lapping and polishing, Ni/Ge/Au was evaporated to form the bottom contact, and the wafer was cleaved into individual laser die.

The cleaved devices were mounted on carriers as indicated in Fig. 4.2.1. The bottom contact of the laser was die bonded to the Au coated SiC heat sink using AuSn solder, which in turn was soldered to the copper block. This entire assemblage is fastened with epoxy to the ceramic carrier, and Au wire bonds make connect from the top of the laser to the Au bond pads on the ceramic carrier. This type of mount facilitated the handing of individual devices, as well as making electrical and thermal contact possible.

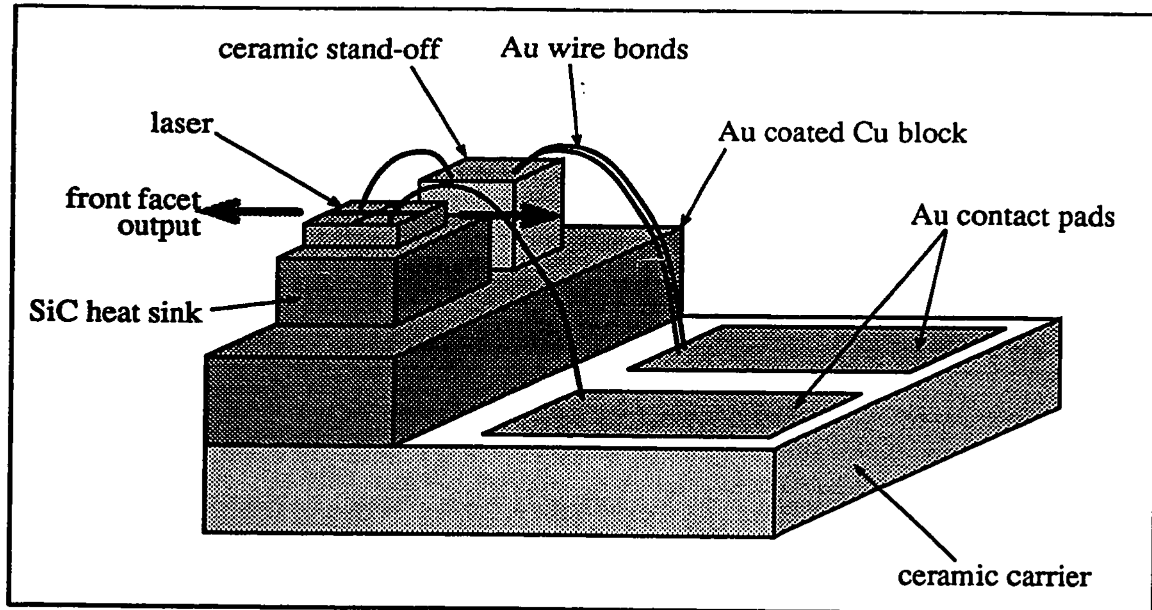

Figure 4.2.1: Schematic of the Mounted Laser Structure
The configuration of the lasers after mounting is shown. Electrical contact is made to the top contacts at the Au contact pads on the ceramic carrier. The device can be grounded through the copper block, which is electrically connected to the bottom laser contact.

The dimensions of the devices studied in this thesis are given in Table 4.2.2. Contact sizes were limited at one extreme by the minimum size that could be contacted by the wire bonder, and at the other by the maximum length of the laser (~1000 μm) that could be easily mounted on the SiC heat sinks, and by the design of the mask itself. Because of the nature of the mounts, it was only possible to extract light from the front

Bar #	Contact Lengths [μm]	Approx. Laser Length [μm]
1	200 / 310	510
2	100 / 290	390
3	300 / 300	600
4	300 / 400	700
5a	500 / 300	800
5b	200 / 600	800
6	450	450
7a	500 / 150	650
7b	400 / 250	650
7c	300 / 350	650
8a	100 / 400 / 390	890
8b	300 / 200 / 390	890
8c	200 / 400 / 290	890
8d	400 / 490	890

Table 4.2.2: Laser Contact Lengths

The contact lengths for the lasers available for this study are indicated, along with the total device length.

facet of each laser. However, because there were from three to ten of each type available, nominally identical devices could be mounted with opposite orientations, in order to measure the light output from either end of similar lasers.

In order to check the electrical isolation between the two sections of the lasers, current-voltage measurements were made between the top two contacts; the resulting resistances varied between 550 Ω and 1200 Ω from device to device. This range is orders of magnitude greater than the resistance of a forward biased p-n junction (typically a few ohms), so that we can reasonably neglect longitudinal leakage between the contacts. The assumption that carriers are injected vertically through the cladding into the active region under the contact, which we made for the model in Section 2.1, therefore seems

reasonable for the lasers used in this work. It is possible that leakage between the contacts might become significant under strong reverse bias, but these extreme conditions did not occur for the biases presented in this work.

4.3: Experimental Apparatus and Technical Considerations

4.3.1: Optical Power Measurements

The first stage in characterizing our split-contact lasers was to measure the light output as a function of the bias currents (i.e. *L-I* characteristics). The experimental set-up used to collect this data is shown schematically in Fig. 4.3.1. Bias current is supplied to the top contacts of the laser through two (or more) of the source-measurement units (SMUs) in the parameter analyzer. This configuration allows us to record the contact voltages as we supply current (i.e. perform *I-V* measurements), in cases where this is desired. The back contact is grounded through the copper block, which also allows thermal contact between the laser substrate and the thermo-electric (TE) cooler. A third SMU is used to measure the photocurrent from the InGaAs detector.

The TE cooler was driven by an ILX LDC-3722 Laser Diode Controller, using a 10 kΩ thermistor to monitor the substrate temperature. Unless otherwise stated, the controller was set to fix the TE cooler at a constant 21°C. Since the test laser was not in an evacuated chamber the device was exposed to the ambient air in the room, and the temperature of the active region of the laser was not necessarily at this fixed temperature. However, our measurements showed that the presence of the TE cooler was sufficient to stabilize the laser output characteristics.

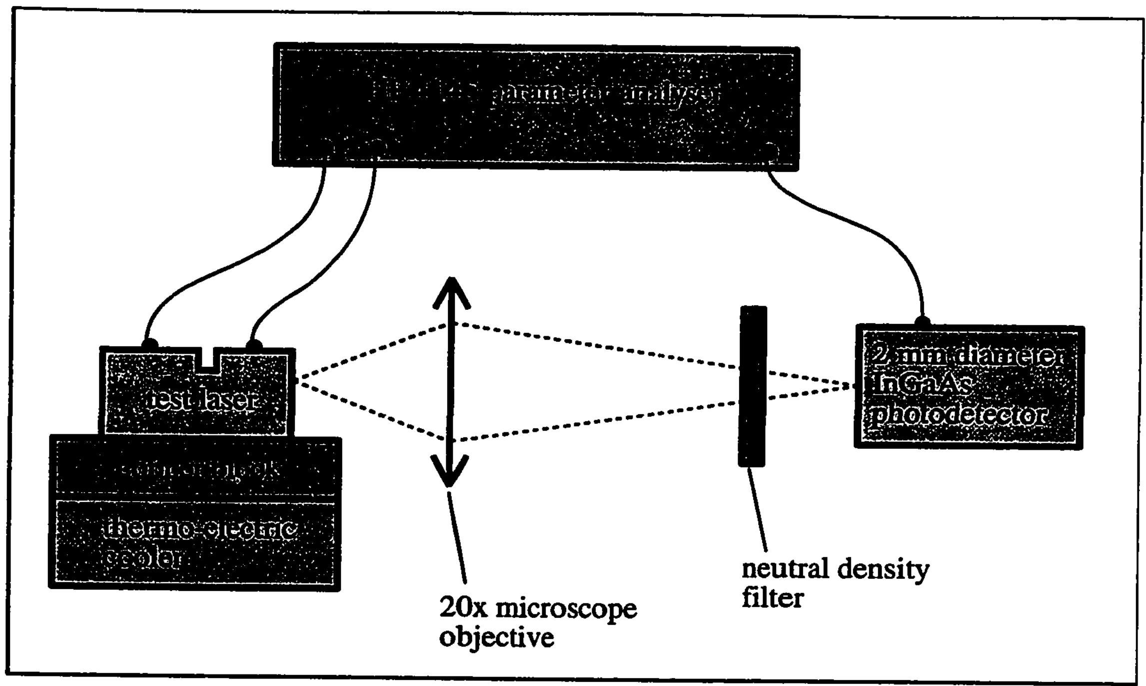

Figure 4.3.1: Schematic of *L-I* Measurement Apparatus

The experimental set-up used to collect *L-I* data from the lasers is shown. The parameter analyzer supplies the bias to the laser and measures the corresponding detector photocurrent. The neutral density filter is removable, and is only used in cases where the optical power exceeds the detector limits.

With the neutral density filter shown in Fig. 4.3.1 removed, the overall optical responsivity of this system was estimated at ~0.71 A/W. In what follows, this figure has been used to convert the measured detector photocurrent into the optical power out of the laser facet. In cases for which the optical power reached levels that could saturate or damage the detector, a neutral density filter was added to the system; the data presented in this work has been corrected for the effect of this filter.

4.3.2: Spectral Measurements

In addition to making measurements of the output power vs. bias on our split-contact lasers, we have also performed investigations of their output spectra. Fig. 4.3.2 illustrates the equipment used to collect the spectral data: the Keithley SMUs[a] were used to apply constant current biases to the two contacts of the laser, and the InGaAs detector to collect the light from the exit slit of the monochromator. This detector was connected to the current input of the Stanford Research Systems Lock-in Amplifier, so that the photocurrent could be measured directly. The Spex 500M is a 0.5 m monochromator with a 600 groove/mm blazed grating. Syncronization and data collection were automated by

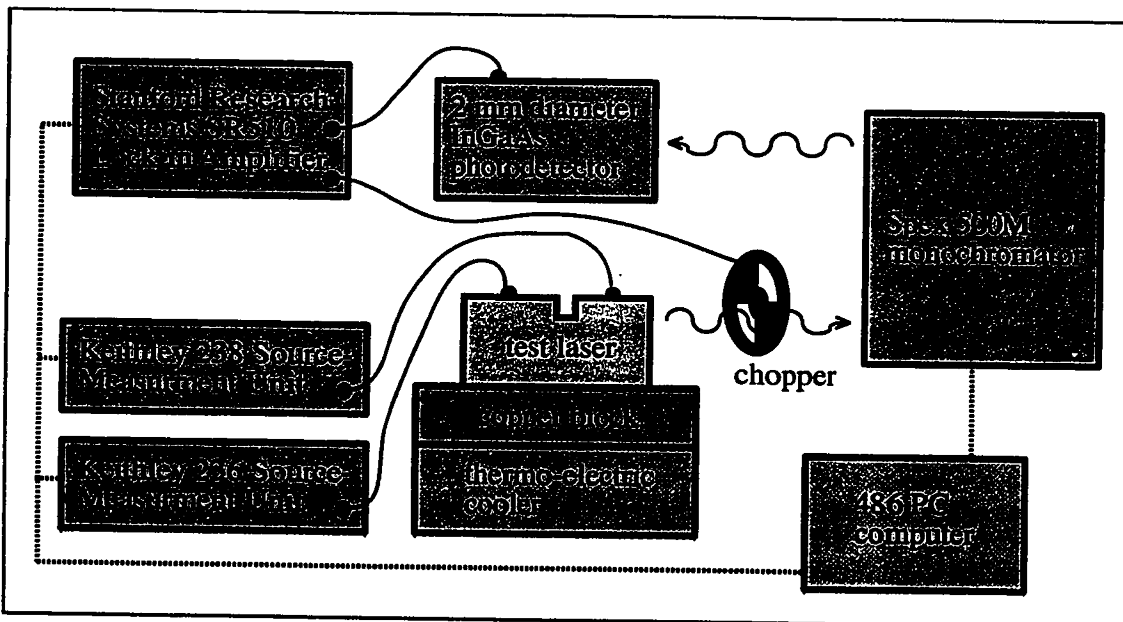

Figure 4.3.2: Schematic of Spectral Measurement Apparatus
The experimental set-up used to collect spectral data from the lasers is shown. The Keithley SMUs supply the bias to the laser and the lock-in measures the corresponding detector photocurrent. Dotted lines represent PC-GPIB connections, through which the computer automates the measurements.

---

[a] Source-measurement units, similar to those in the H.P. 4145 in Fig. 4.3.1.

the 486 computer, which controlled everything except for the chopper and temperature controller. The device substrate temperature was set to 21°C for all of the following measurements: the temperature stage is the same as that used for the *L-I* measurements, and is described in more detail in Section 4.3.1.

4.3.3: Comparing Experimental and Simulated Results

Before we commence with the presentation of the experimental measurements, a few words seem necessary with regard to comparisons made between the measured and simulated results. Although there are many possible causes of discrepancies between these two sets of data, there are two that seem to be particularly significant, and deserve specific mention.

The first of these has to do with the experimental environment in which we are working. As explained in Section 4.3.1, although the temperature of the laser substrate is generally held at a fixed value, because of the mounting system used the same is not necessarily true of the active region. In particular, for measurements in which large currents are being applied to small contact areas, the high current densities mean that the power dissipated per unit area is large. This naturally leads to some heating of the active region of the laser. The effect of this on the laser characteristics is twofold: 1) the energy distribution of the carriers in the active region becomes broadened, causing an increase in the leakage current which can affect both the threshold and output efficiency, and 2) the semiconductor band-gap will decrease slightly,[a] resulting in a red shift in the output wavelength. Since neither of these factors has been considered in the model, any comparisons of theory with experiment must be interpreted in this light.

---

[a] Adachi[2] estimates the rate of change in lasing wavelength with temperature to be $d\lambda/dT \sim 4$ Å/°C, for an InGaAsP/InP based device operating at ~1.3 μm.

The second major cause of discrepancies lies in our approximation of the semiconductor band structure. In Section 2.1.1 we explained that we had decided to consider only simple, isotropic, parabolic bands in our simulations, which results in a $\sqrt{E}$ dependence of the density of states on the carrier energy. However, as Table 4.2.1 indicates, the actual devices that we have to work with contain a multi-quantum well active region whose density of states is expected to be piecewise constant. Although this may affect all of the simulated characteristics to some degree, the most noticeable effect is expected to be in the spectral simulations. The wavelength of the gain peak is expected to be at some energy slightly above the band edge for parabolic bands (see Fig. 2.4.1), but ideally it is always at the band edge in a quantum well structure.[3] The wavelength shifts caused by variations in the gain peak with carrier injection that are observed in our simulations are therefore not expected to be observed for a quantum well device. However, tuning effects caused by varying index of refraction (as described in Section 3.8) and heating are still present in the quantum well lasers.

Our experimental study has also been somewhat limited in its range by the equipment available, and by the laser mounting configuration. In particular, the bonded laser shown in Fig. 4.2.1 is not suitable for high speed device modulation, and the time-domain response of our apparatus made measurements of gigahertz self-pulsations impractical. We have endeavoured to supply the applicable literature references along with our simulations in areas where our own measurements are lacking.

4.4: Examples of Optical Power vs. Bias Current

The variety of contact lengths available for this study, combined with the different combinations of biases that can be applied to each device, results in a formidable selection of optical characteristics to present. We therefore endeavour in this section to show a series

of typical *L-I* curves that illustrate the trends we have observed. In Section 4.5 we give a more general picture of how the laser output varies with bias and contact geometry by comparing the output power contours and threshold currents of different devices.

4.4.1: *L-I* Curves Demonstrating Typical Device Operation

The first series of optical characteristics that we wish to consider, a set of L-I_B curves with I_F as the parametric variable, is plotted in Fig. 4.4.1. Here we show the optical output from a typical device from Bar #2 (see Table 4.2.2), with the longer section toward the front of the mount. The output is characteristic of what we have come to expect from a non-uniformly pumped laser: for each constant value of I_F we observe a low-output

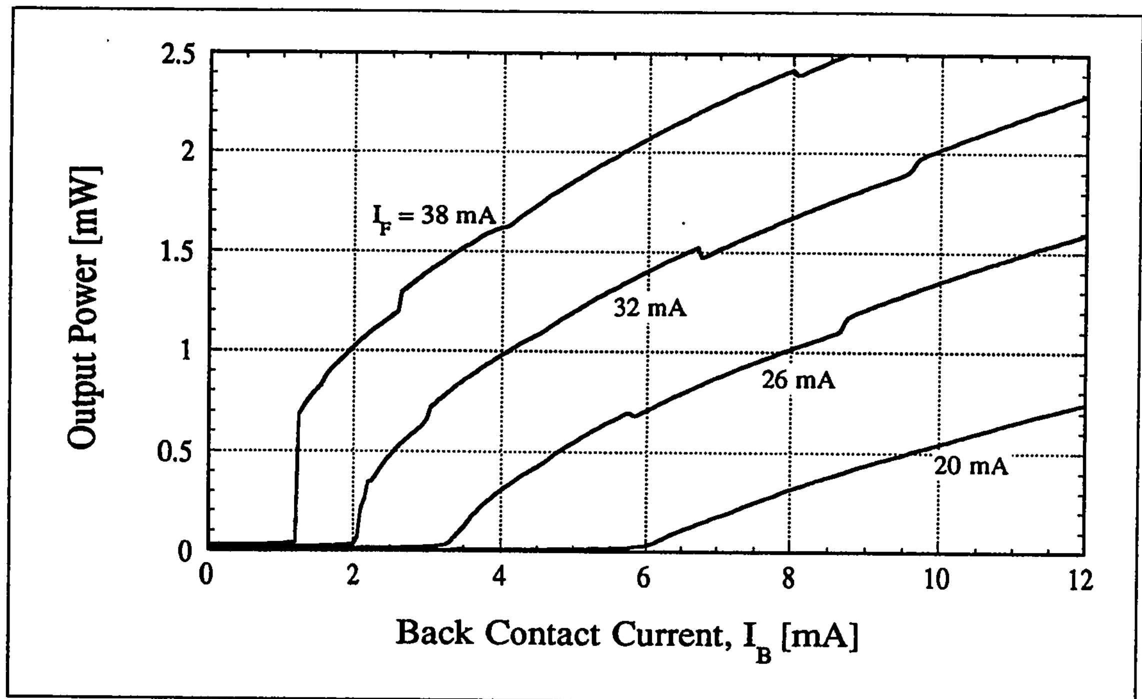

Figure 4.4.1: *L-I* Curves, Illustrating Varying Threshold & Discontinuity
Several *L-I* curves are plotted, at constant values of the front contact current, I_F, and with the back contact current, I_B increasing. The front contact length is $L_F = 290$ µm, the back contact is $L_B = 100$ µm.

region below threshold, and a lasing, strongly emitting region at higher currents. The value of the threshold current at the back contact, $I_{B,th}$, decreases for larger I_F, as we would expect both from qualitative considerations and from the simulated results plotted in Fig. 3.4.1.

In addition to these broader trends, we also note that the non-linearity in the output is greatest just above threshold, and more pronounced for larger values of the constant bias (in fact, there is a discontinuity at threshold for the $I_F = 38$ mA curve). This is a feature that is predicted by our model, as evidenced by the *L-I* simulations shown in Fig. 3.4.1. Although the match between the simulated device parameters and the measured lasers is not quantitatively ideal, the *L-I* characteristics near threshold changes in a similar manner with the constant current in both Figs. 3.4.1 and 4.4.1.

There are a few features in Fig. 4.4.1 that our model does not anticipate. Firstly, the *L-I* curves are not perfectly linear, even well above threshold. To some degree this curvature can be attributed to heating effects which we have not taken into account in our model. This would generally cause the output power to have a slightly sub-linear dependence on the bias current, because the device efficiency is expected to decrease with temperature. Although our model does predict the curvature near threshold, heating is likely the cause of the decreasing values of dL/dI at biases substantially above threshold. This phenomenon is commonly observed in uniformly pumped lasers (see Shimura et al.,[4] for example).

A second somewhat unexpected feature of the *L-I* in Fig. 4.4.1 is the small jumps that occur above threshold (for example in the $I_F = 26$ mA curve, at $I_B \sim 5.8$ and 8.8 mA). Although the reason for this structure is not obvious from the data presented here, further investigations have indicated that at these bias points the laser spectra was undergoing a mode hop. (This mode hopping behaviour is discussed in more detail for

uniformly pumped lasers by Gray et al.[5]) In a real device the different cavity modes may not have the same optical confinement factors, scattering rates, and detailed spectral structures; these factors can cause the variations in the experimentally observed output power that are correlated with mode hops in Fig. 4.4.1. Since these effects are not considered in our theoretical model, the simulated *L-I* curves to not contain jumps at points where mode hops occur (see, for example, the $I_2 = 0$ *L-I* plot in Fig. 3.4.1, and the corresponding spectral simulation in Fig. 3.4.2).

4.4.2: *L-I* Curves Demonstrating Superluminescence

In Fig. 4.4.2 we have plotted a family of L-I_F curves (with I_B as the parametric variable) from a laser from Bar #5a (see Table 4.2.2) which illustrate the superluminescent regime of device operation. This device is more than twice as long as the one used for Fig. 4.4.1 ($L_T = 800\ \mu m$, as opposed to 390 μm), and in Fig. 4.4.2 the strongly pumped contact is also the shortest one. The combination of these two factors results in a relatively high threshold current value, with a distinct region of enhanced emission as threshold is approached (between $I_F \sim 30$ mA and threshold). This high level of sub-threshold output is due to the strong pumping of the shorter contact: the gain in this section of the laser is great enough to amplify the spontaneous emission. Even so, this light must reach a considerable power level before threshold is achieved because the relatively weak pumping of the long section of the laser results in high absorption losses.

This superluminescent effect is one which we have also observed in our simulations (specifically in Figs. 3.4.7 and 3.4.8), and occurs for similar device configurations. Both experimentally and theoretically we find that this regime of device operation is enhanced by increasing the length of the absorbing section of the laser, and by decreasing the bias current into this contact.

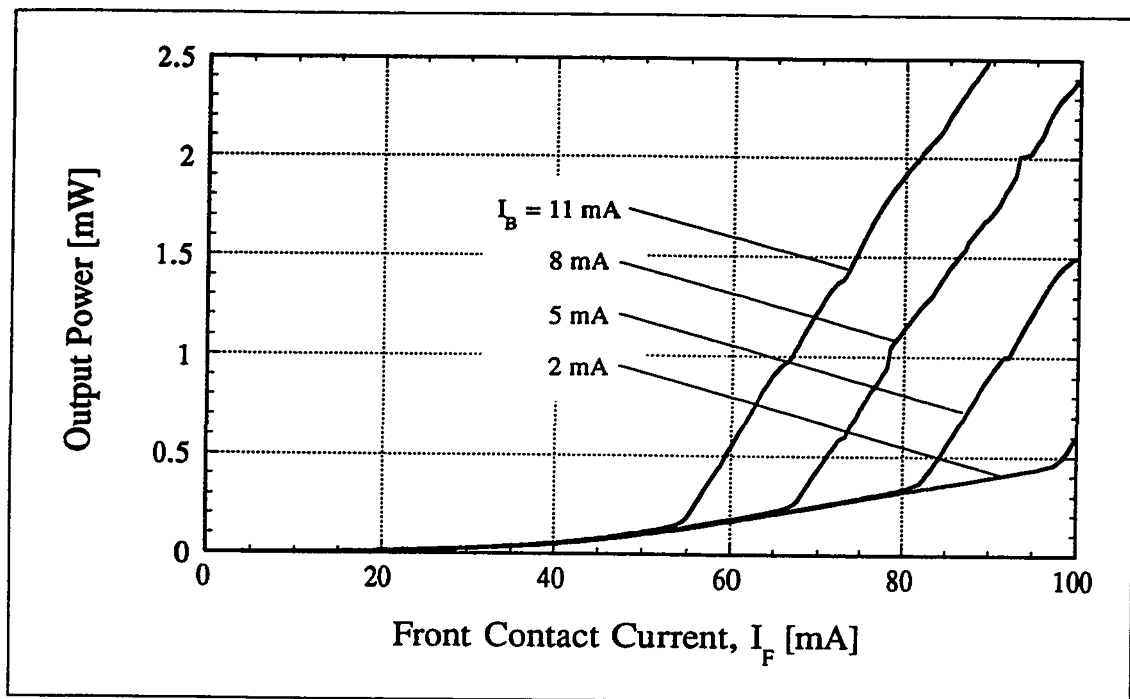

Figure 4.4.2: *L-I* Curves, Illustrating Superluminescent Behaviour
Several *L-I* curves are plotted, at constant values of the back contact current, I_B, and with the front contact current, I_F increasing. The front contact length is L_F = 300 µm, the back contact is L_B = 500 µm.

The effect that a constant value of I_B has on the *L-I* characteristics in Fig. 4.4.2 also supports our contention that the high output levels observed below threshold are a result of amplified spontaneous emission. Although the value of I_F at which threshold occurs decreases with larger values of I_B, the output levels below threshold are unaffected by the back contact current. This is what we would expect if the sub-threshold output is due to the amplified spontaneous emission under the front contact: increasing I_B decreases the threshold current because it lowers the absorption under the back contact, but it does not have any noticeable effect on the gain and spontaneous emission levels in the front section.

4.4.3: *L-I* Curves Demonstrating Bistability

In Fig. 4.4.3 we show an example of a family of L-I_F curves with I_B as the parametric variable, taken from a laser in Bar #2 that exhibits bistablity. To better illustrate the trends produced by the device, in this case we have plotted the output power as an elevation above the I_F-I_B plane. We see that the L-I_F at $I_B = 5$ mA is linear above threshold and continuous, as is commonly observed in uniformly pumped lasers. As I_B is decreased, a discontinuity appears at threshold, although there is at first no hysteresis in the L-I_F. The

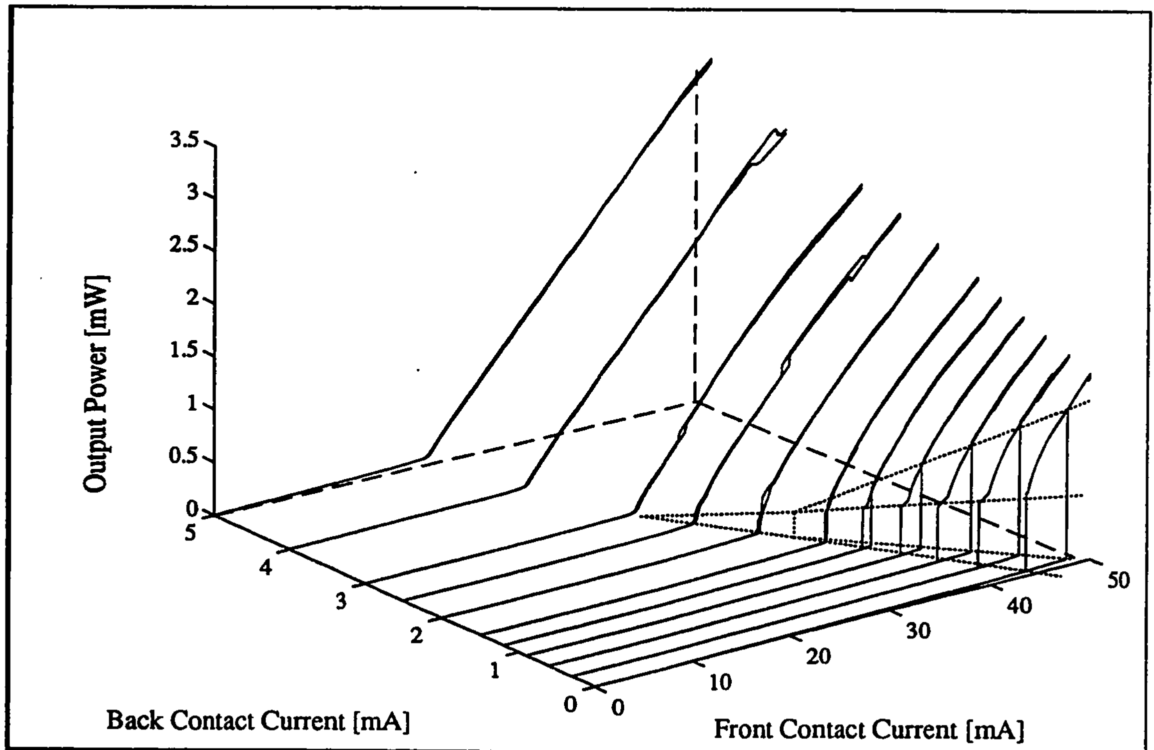

Figure 4.4.3: *L-I* Curves Illustrating Optical Bistability

Several L-I_F curves are plotted, at constant values of the back contact current, I_B, and with the front contact current, I_F, both rising and falling. The front contact length is $L_F = 290$ µm, the back is $L_B = 100$ µm. The surface of the hysteresis region defines a wedge-shaped volume, indicated by the broken lines in the lower right portion of the plot. Extending from the narrow end of this wedge is a vertical, triangular plane in which there is a discontinuity in the output power at threshold, but no bistability.

region covered by this discontinuity, which is approximately denoted by the dashed triangle sketched on the figure, extends from $I_B \sim 2.8$ mA to 1.6 mA. When I_B is decreased below 1.6 mA, the position of the discontinuity splits, and is dependent on the direction of the current sweep. For these biases hysteresis is observed in the *L-I* curves; this wedge-shaped region of bistability is roughly indicated by the dashed lines in Fig. 4.4.3.

Figure 4.4.3 indicates that the transition from continuous *L-I* curves to those with a discontinuity, and eventually to bistable characteristics, is a smooth one. The discontinuity begins with negligible height (at $I_B \sim 2.8$ mA), and then increases steadily in size as I_B decreases. Similarly, the transition to bistability begins with a small splitting of the discontinuity (at $I_B \sim 1.6$ mA), and the width and height of this region increase smoothly with decreasing I_B. Although Fig. 4.4.3 illustrates this for a specific device from Bar #2, it is a trend that we have generally observed in all lasers that exhibit discontinuities or bistability.

The observed changes in the discontinuity in Fig. 4.4.3 make sense in light of our previous discussion of the non-uniformly pumped laser simulations. When the current densities in the two sections of the laser are similar near threshold (the $I_B = 5$ mA curve in Fig. 4.4.3, for example), the device behaves like a uniformly pumped laser. As the difference between the current injection levels in the two sections increases, the carrier density in the two regions begins to differ by a greater extent, and the device starts to exhibit behaviour characteristic of non-uniform pumping. In Fig. 4.4.3, as I_B is decreased the difference between the bias current densities J_F and J_B at threshold increases. The saturable absorber effect first manifests itself as a small discontinuity at threshold, which increases in size as I_B decreases. Eventually this phenomenon becomes strong enough for the output to latch ON even after I_F is decreased below the turn-on discontinuity, and we reach the bistable regime. For the device in Fig. 4.4.3, the height and width of the

hysteresis loop continue to expand as I_B is decreased (at least until the voltage compliance is reached).

One other point about Fig. 4.4.3 that perhaps merits mention is the existence of jumps and hysteresis loops above threshold in some of the curves (for $I_B = 2.5$ and 4 mA, for example). As was observed in connection with Fig. 4.4.1, these small discontinuities are associated with mode hops in the spectral output of the laser. They tend to be present more commonly for strongly non-uniform pumping configurations, and can exhibit hysteresis in a manner similar to the larger discontinuity at threshold.

4.5: Output Power Dependencies

The *L-I* characteristics presented in the Section 4.4 are examples of particular bias conditions on individual devices. Although these are quite useful for demonstrating specific structural elements of the curves, as well as for comparison with our simulated *L-I*, it is difficult to get a general overview of the effects of contact length and bias on the laser output from them. In this section we therefore attempt to give a broader survey of the laser behaviour by presenting a series of contour plots in the I_F-I_B plane, extracted from the individual *L-I* curves measured from a number of devices.

4.5.1: L-I_F-I_B Contours

Figure 4.5.1 shows an example of a detailed L-I_F-I_B contour plot, for the same device as was used for the *L-I* plot in Fig. 4.4.3. This plot was constructed using the data from approximately one hundred distinct *L-I* curves; although we cannot easily observe the detailed structure of the hysteresis loops that were visible in Fig. 4.4.3, it does allow us to formulate an overall impression of the output power dependence on the two contact biases.

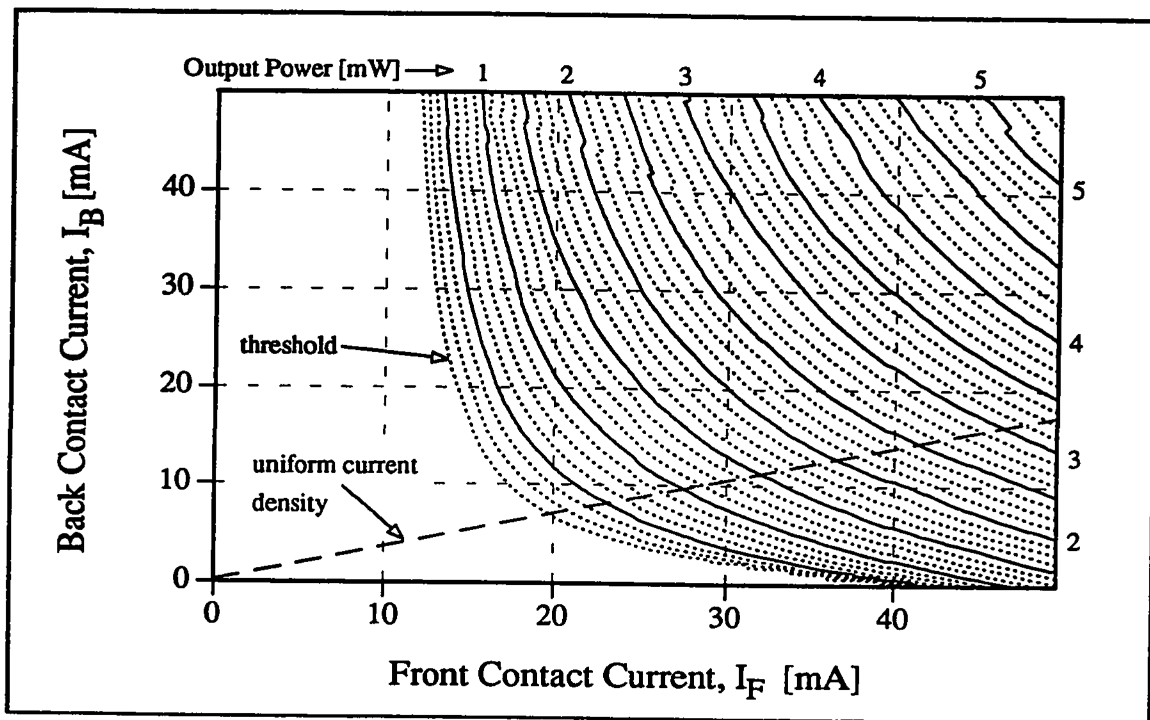

Figure 4.5.1: Contour Plot of the Output Power in the I_F-I_B Plane

Contours of constant laser output power are plotted in the bias current plane. The length of the front contact of the laser is $L_F = 290\ \mu m$, the back is $L_B = 100\ \mu m$. The left-most contour (i.e. the one for the lowest power) gives an approximate representation of the threshold condition. The line representing the bias points along which the injected current density is uniform is also indicated.

The pattern of the contours we observe in Fig. 4.5.1 is typical (at least qualitatively) of those measured for all of our devices. In general, the contour lines have a positive curvature and the "nested" form illustrated, although the specific position and spacing of the contours varies with the device geometry. If we track the output power along the line of uniform current density (i.e. the path that would be followed if the top contacts were electrically shorted together) the output appears to be typical of a uniformly

pumped laser: the light output is minimal at low biases, and rises approximately linearly with current above threshold.*

Of course, the advantage of a two-contact laser is that we are not constrained to operate along the uniform current density line. In general, we expect the saturable absorber effects to be most prominent when the biases on the two laser sections are substantially different, i.e. close to the axes in Fig. 4.5.1. An example of this is the discontinuities we saw in Fig. 4.4.3: this phenomenon can be observed in Fig. 4.5.1 in the region where $I_F > 30$ mA and $I_B < 5$ mA. The convergence of the contour lines in this area indicates an abrupt jump in the output power of the laser.

It is interesting that we do not see a similar effect for low values of I_F; indeed, it does not appear possible to achieve lasing in this structure for $I_F < 11$ mA. This is most likely due to heating of the laser, as discussed in connection with Fig. 3.4.6 in Section 3.4.2. In Fig. 4.5.1 we see that the threshold condition with the back contact open circuited (i.e. $I_B = 0$) is $I_F \sim 42$ mA. If we try to supply the same current through the back contact, however, the current density in the back section will be greater than it was in the front, by a factor of ~3 (the ratio of the contact lengths). This higher current density means that more power must be dissipated in a smaller volume, causing heating of the device and consequently increasing the lasing threshold.

4.5.2: Device Geometry Effects, Varying L_T

Although Fig. 4.5.1 gives a fair overall illustration of the output power of a split-contact laser under varying bias, it still does not tell us anything about how the output varies with the contact geometry. In order to design devices for specific applications, it

---

* This is indicated by the fact that the spacing of the contours along the uniform current density line is approximately equal.

would be particularly helpful if we could use our data to determine empirically how the laser output varies with the lengths of the contacts. We attempt to address this issue by plotting the threshold current contours in the bias plane for a series of devices with different contact geometries.

Figure 4.5.2a allows us to compare the threshold contours for two lasers with different total lengths (L_T = 390 and 800 μm), but with the same ratio of contact lengths (L_F/L_B ~ 3). As one might expect, for a given bias current on one of the contacts, the current required on the other to reach threshold is always greater for the longer laser (800 μm) than for the short one (390 μm). The details of the relationship between the two contours are quite complicated: they are separated neither by a constant multiplicative factor, as we might expect if the current densities were comparable, nor by a constant current difference. In addition, at biases where $I_B \leq 2$ mA we see that the 390 μm laser exhibits bistability (the threshold contour for the increasing bias is not identical with the one representing decreasing current). In the 800 μm device there was no evidence of bistability for any bias configuration.

Instead of fixing the ratio of the contact lengths, we have plotted the threshold current contours for devices with a constant front contact length constant (L_F ~ 300 μm) and different values of the total laser length, L_T, in Fig. 4.5.2b. In this case we observe a different pattern as we vary L_T: at high values of I_F the value of I_B at threshold increases with the device length, but the opposite is true at low I_F. In between lies a transition region in which all the device thresholds are similar, and the changes in threshold with L_T are not monotonic. This sort of behaviour is more complicated than the case of Fig. 4.5.2a, and is not something that was expected to occur. For example, at (I_F, I_B) = (13, 30) mA, the threshold contours for L_T = 800 and 400 μm intersect: here we have two devices with the same threshold condition, but for which the lengths differ by a factor of two. Although at

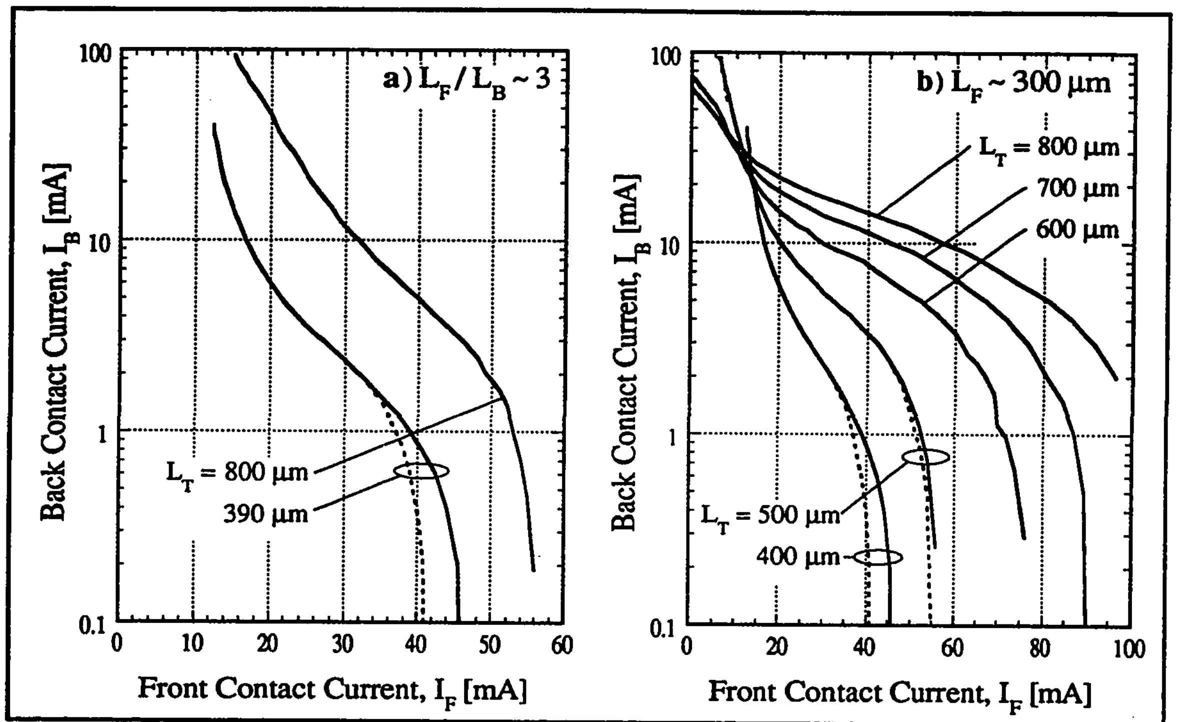

Figure 4.5.2: Threshold Contour Plots, Varying L_T

The threshold current contour is plotted for the cases where: **a)** the total laser length, L_T, is varied, and the ratio of the contact lengths is held constant at $L_F/L_B \sim 3$, **b)** L_T is varied and the length of the front contact is held constant at $L_F \sim 300$ µm. In all cases, solid lines indicate that the current is increasing, and broken lines represent decreasing bias.

first this may seem counter-intuitive, we speculate that the effect of the higher current density in the shorter device is offset by the greater resulting heating.

Another feature of interest in Fig. 4.5.2b is the evolution of the bistable region as L_T is increased. We see that optical hysteresis occurs most strongly for small values of I_B (≤ 3 mA) and L_T (≤ 500 µm). It is evident, then, that in this case the back contact is acting as the saturable absorber, so that keeping the bias on this section low enhances the range of the bistability. Additionally, it also seems that when this region becomes too long ($L_B > 200$ µm) the action of the saturable absorber is quenched. This trend is the opposite to that which we observed in our simulations (compare the $I_I = 0$ curves in Figs. 3.4.4

and 3.4.8, for example). We suggest that this discrepancy is due to heating effects at the higher current levels, which are not accounted for in our model.

Finally, it should be pointed out that the boundaries of the hysteresis regions in Fig. 4.5.2 are independent of which bias current is varied. If the device was previously OFF, it switches ON when either I_F or I_B is varied in such a way as to move the bias point across the solid line, in a direction away from zero bias. Similarly, varying either (or both) currents so that the broken line is crossed moving toward zero bias switches the laser from ON to OFF. The device state does not change if the bias point moves into the hysteresis region along any path exits that region across the same border (either solid or broken) that it entered.

4.5.3: Device Geometry Effects, Varying L_F

Figure 4.5.3a illustrates a slightly different situation. This is the same type of plot as Fig. 4.5.2, but in this case we hold the total length of the laser fixed at L_T = 650 μm and vary the length of the front contact. As in Fig. 4.5.2b, we see that the threshold contours for the different lasers intersect, although this is not quite as surprising in this case as the total laser length is the same for all the curves.

When we replot the data from Fig. 4.5.3a in terms of current density in Fig. 4.5.3b, we notice an interesting correlation: all the contour intersections lie within 0.01 mA/μm of each other. If we consider the threshold current density for a uniformly pumped device of the same length (indicated by the white circle), we see that this point is also within the same tolerance of the intersections. A similar relationship was found to hold between lasers in Bars #5a and 5b (with L_T = 800 μm); further study on devices with different structures would be helpful to clarify whether this is a general rule, or simply coincidental in the lasers we have examined. This relationship is a purely empirical

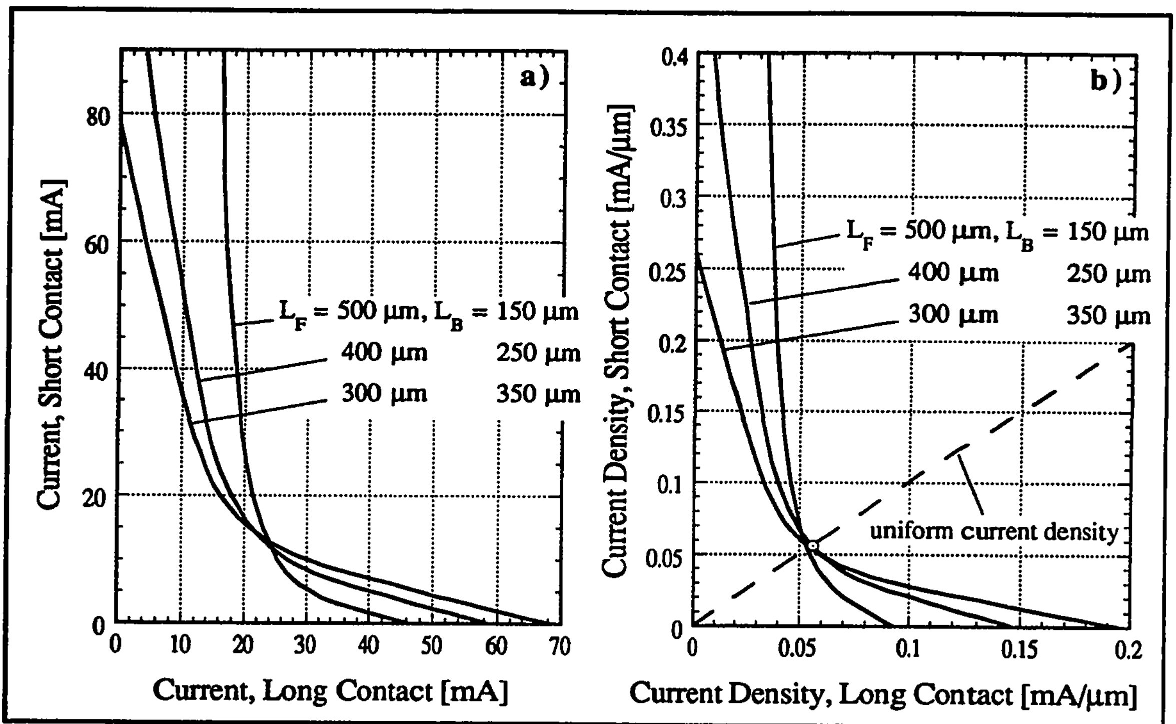

Figure 4.5.3: Threshold Contour Plots, Varying L_F

The threshold contours are plotted for the case where the total laser length is fixed at $L_T \sim 650$ µm, and the front contact length is varied. Part **a)** shows the contours in terms of the total currents, in part **b)** the axes have been normalized to the linear current density. The white circle in part **b)** represents the threshold condition for a uniformly pumped laser with a length of 650 µm, and the dashed line shows the bias points along which the current density is uniform.

observation, but it could prove useful in future attempts to predict device performance or to design split-contact lasers with specified threshold currents.

4.6: Results of Spectral Measurements

In Section 4.6.1 and 4.6.2 we present a series of examples that typify the measurements we have performed. Then, in Section 4.6.3 we attempt to summarize the results, to give an overview of the sort of spectral characteristics that can be expected above threshold from split-contact, Fabry-Perot lasers.

4.6.1: Examples of Superluminescent Spectra

Before we delve into the results of the detailed, above-threshold spectral measurements, we would like to present some data measured on a device biased below threshold. In particular, in relation to Fig. 4.4.2 we claimed that before threshold was reached, the device was operating in a superluminescent regime in which the large output power was a result of amplified spontaneous emission. Although this statement was supported by our modelling work (see Figs. 3.4.7 and 3.4.8), we now wish to verify it experimentally by plotting some examples of the output spectra in Fig. 4.6.1.

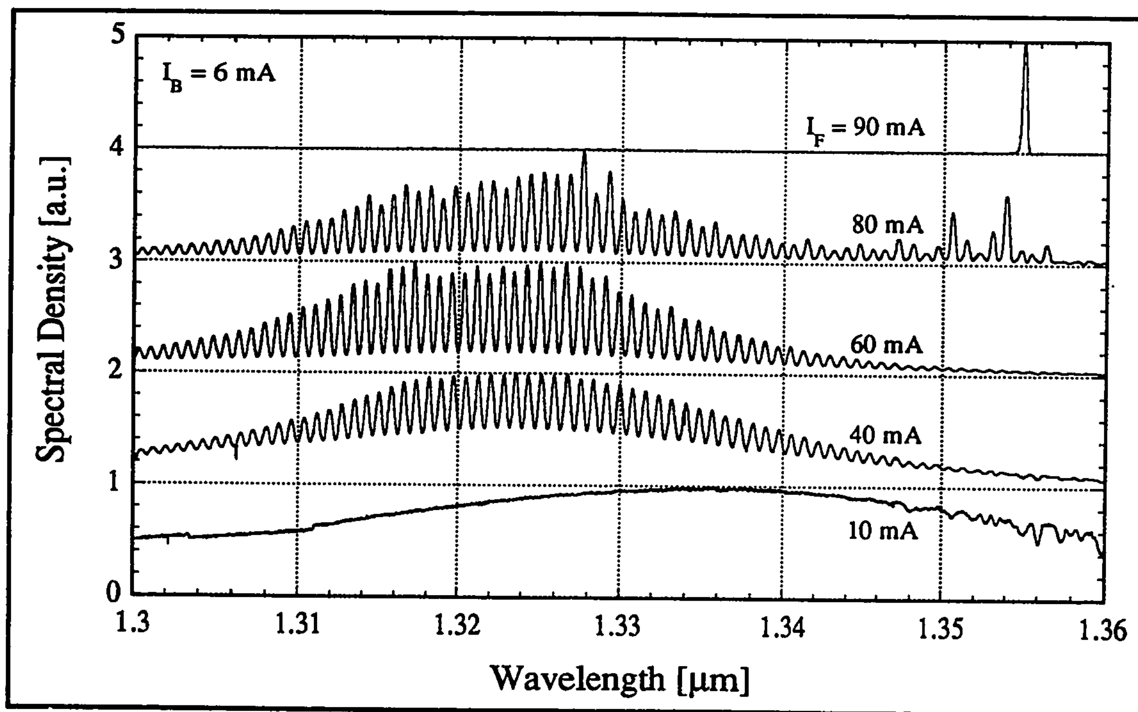

Figure 4.6.1: Spectra in the Superluminescent Regime
Several output spectra from a device with $L_F = 300\ \mu m$ and $L_B = 500\ \mu m$ are plotted. The spectral curves have been normallized to unity peak height, and vertically offset (for $I_F > 10$ mA) for clarity. From the device *L-I* curves (not shown) superluminescence commences at $I_F \sim 30$ mA, and lasing at $I_F \sim 80$ mA.

Figure 4.6.1 illustrates the spectral output of the laser from which the *L-I* in Fig. 4.4.2 are taken, at biases in the superluminescent regime ($I_F \leq 60$ mA), at threshold ($I_F = 80$ mA), and above threshold ($I_F > 80$ mA). We observe that a definite, qualitative change occurs at threshold: below 80 mA the output consists of a broad (>200 Å) spectral envelope peaking between 1.32 and 1.33 μm. Above 80 mA the laser power is concentrated in a single cavity mode at $\lambda \sim 1.355$ μm, and just at threshold we see a combination of the two competing effects. This is the sort of transition that our theoretical work would lead us to expect as operation switches from superluminescence to lasing. The superluminescent light has a much wider, blue-shifted spectrum because it is primarily determined by the spontaneous emission profile, which is considerably broader than the gain profile that governs the above-threshold output (see Figs. 2.3.1 and 2.4.1).

4.6.2: Examples of Lasing Spectra

Figure 4.6.2 shows the sample spectra from a laser from Bar #2 (see Table 4.2.2), in which the tuning of a single cavity mode is evident. Each individual spectrum represents the laser at a constant bias current: $I_B = 9$ mA in all cases, with the front contact current falling into the range 50 mA $\leq I_F \leq$ 98 mA.

The data presented in Fig. 4.6.2 represents the dominant laser mode throughout the range of biases plotted. We see that it is possible to vary the wavelength of this mode continuously by approximately 7.7 Å before the majority of the power switches to a different cavity mode. Since the cavity mode spacing for a laser of this length is ~6.5 Å, we have actually managed to tune the dominant mode over a greater range than one would expect from simple mode hopping considerations. This extended range can be accounted for by the correlation of different tuning mechanisms, as discussed in Section 3.8. We also note that the shift to longer wavelengths with increased bias is consistent both with a

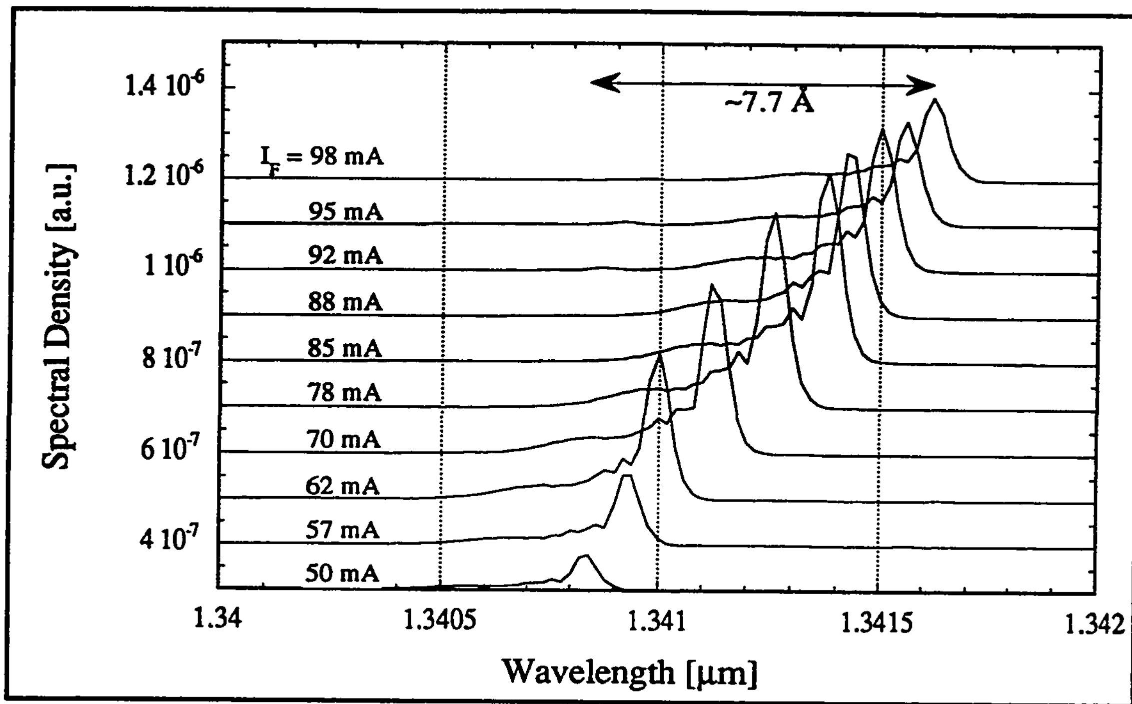

Figure 4.6.2: Tuning of an Individual Cavity Mode

The measured output spectra of the dominant mode from a split-contact laser from Bar #2 are plotted. In all cases $I_B = 9$ mA, the values of I_F are indicated on the plot. All spectra share the same background level; the plots for $I_F > 50$ mA have been offset for clarity. The continuous tuning range for this mode is indicated at the top of the figure.

decrease in the index of refraction (see Section 3.8) and with an increase in heating (because the band gap shrinks with increasing temperature). The specific example depicted in Fig. 4.6.2 represents the typical situation encountered in our spectral measurements: at best it was generally possible to continuously vary the lasing mode over a range approximately limited by the free spectral range of the specific laser (which, of course, is a function of its length).

In order to display the overall spectral output (instead of just focusing on the dominant mode), the spectra from the same device used for Fig. 4.6.2 is plotted over a greater range of wavelengths in Fig. 4.6.3. The range of biases in Fig. 4.6.3 includes

that used in the previous plot ($I_B = 9$ mA and 28 mA $\leq I_F \leq$ 98 mA), but the abscissa has been expanded to include all wavelengths at which there is a significant amount of output power.

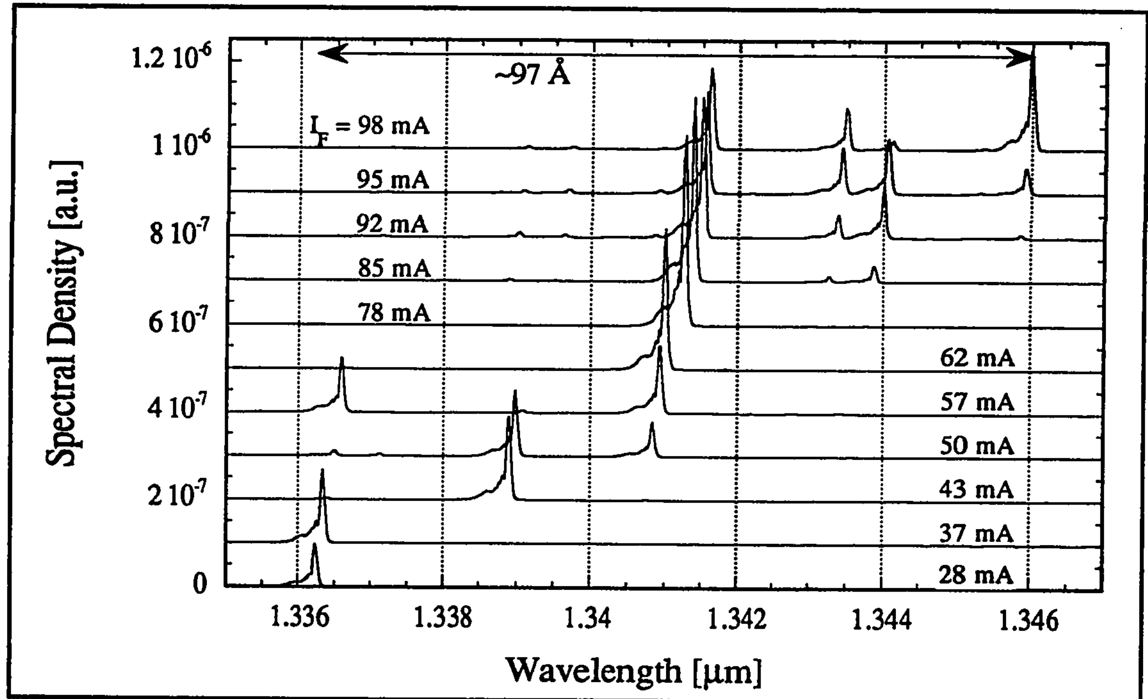

Figure 4.6.3: Laser Spectra at Increasing Values of I_F

The measured output spectra of a split-contact laser from Bar #2 are plotted. In all cases $I_B = 9$ mA; the values of I_F are indicated on the plot. All spectra share the same background level; the plots for $I_F > 28$ mA have been offset for clarity. The maximum variation in the peak output wavelength is indicated at the top of the plot.

A cursory examination of Fig. 4.6.3 reveals that the laser does not always lase at the same mode, nor is the output always single mode. The dominant mode plotted in Fig. 4.6.2 can be seen in Fig. 4.6.3 (between λ = 1.340 μm and 1.342 μm for biases greater than $I_F = 50$ mA). However, at the limits of this bias range we now see that the laser is operating multi-mode, and the bulk of the output power is shifting to a different

spectral position. The total variation in the peak wavelength, ~97 Å, is covered in a series of discontinuous mode hops, each of which spans an integer number of cavity mode spacings.

In terms of their variations with bias, we can divide the spectra in Fig. 4.6.3 into three general regions.[a] At biases near threshold ($25\ mA < I_F < 60\ mA$) the mode hopping behaviour is erratic, with the peak shifting back and forth between cavity modes in an unpredictable fashion. For I_F between about 60 mA and 85 mA we have single mode operation with a small amount of continuous tuning, and above 85 mA there is a consistent tendency for the peak to shift to longer wavelength modes.

The behaviour in the first two of these regions is easily interpreted in light of our simulations in Chapter 3. In Sections 3.4 and 3.8 we saw that tuning caused by both shifts in the gain peak[b] and the changing index of refraction are strongest just above threshold, and become less significant as the bias increases. This would explain the transition from mode hopping to continuous tuning that we observe in the neighbourhood of $I_F = 60\ mA$ in Fig. 4.6.3.

Although our simulated spectra do not reveal an area equivalent to the third region in Fig. 4.6.3 (where $I_F \geq 85\ mA$), we can explain this behaviour in terms of the device heating effects that our model does not consider. Despite the fact that the variations are not continuous, we note that the peak wavelength in this region consistently shifts toward higher wavelengths. This would be expected under conditions where active region heating is becoming significant, because the band gap of the material tends to decrease as the

---

[a] The spectra depicted in Fig. 4.6.3 portray typical results, but do not represent the entire set of biases investigated.

[b] As discussed in Section 4.3.3, this is not expected to make a strong contribution to wavelengths shifts in quatum well devices.

temperature rises.[a] Since we are considering the most strongly biased of the device spectra, in which the current densities are greatest, it is not surprising that heating is the dominant mechanism affecting the position of the spectral peak.

4.6.3: A Split-Contact Laser Spectral Map

In Section 4.6.2 we presented two examples of spectral measurements of a typical split-contact laser. In order to give a more general picture of the manner in which the peak wavelength of these devices shifts with bias, we have summarized the data from a number of spectra in Fig. 4.6.4. A series of ~100 spectra were recorded at bias points which cover the positive portion of the I_F-I_B bias plane, between threshold and 50 mA. When the peak output wavelength was extracted from these data files, it was found that variations in λ_{peak} between adjacent bias points fell into two categories. Either the change in the peak wavelength was small (generally less than 1 Å), indicating continuous tuning of a single mode, or there was a large step (from ~5 Å to > 45 Å). representing a mode hop. In Fig. 4.6.4 we have attempted to map out these peak wavelengths in the bias plane, specifying the regions of continuous tuning and the wavelength ranges over which they are observed.

Although Fig. 4.6.4 does not reveal the same amount of spectral detail seen in Figs. 4.6.1 through 4.6.3, it is intended to provide the same sort of general overview of the spectral output that Fig. 4.5.1 did for the output power. The first impression that we receive from Fig. 4.6.4 is that the output spectra from this device is quite complicated. There is no apparent pattern to the specific positions of the region boundaries, or to the

---

[a] As noted in Section 4.3.3, Adachi estimates this rate of change to be ~ 4 Å/°C. See reference[2].

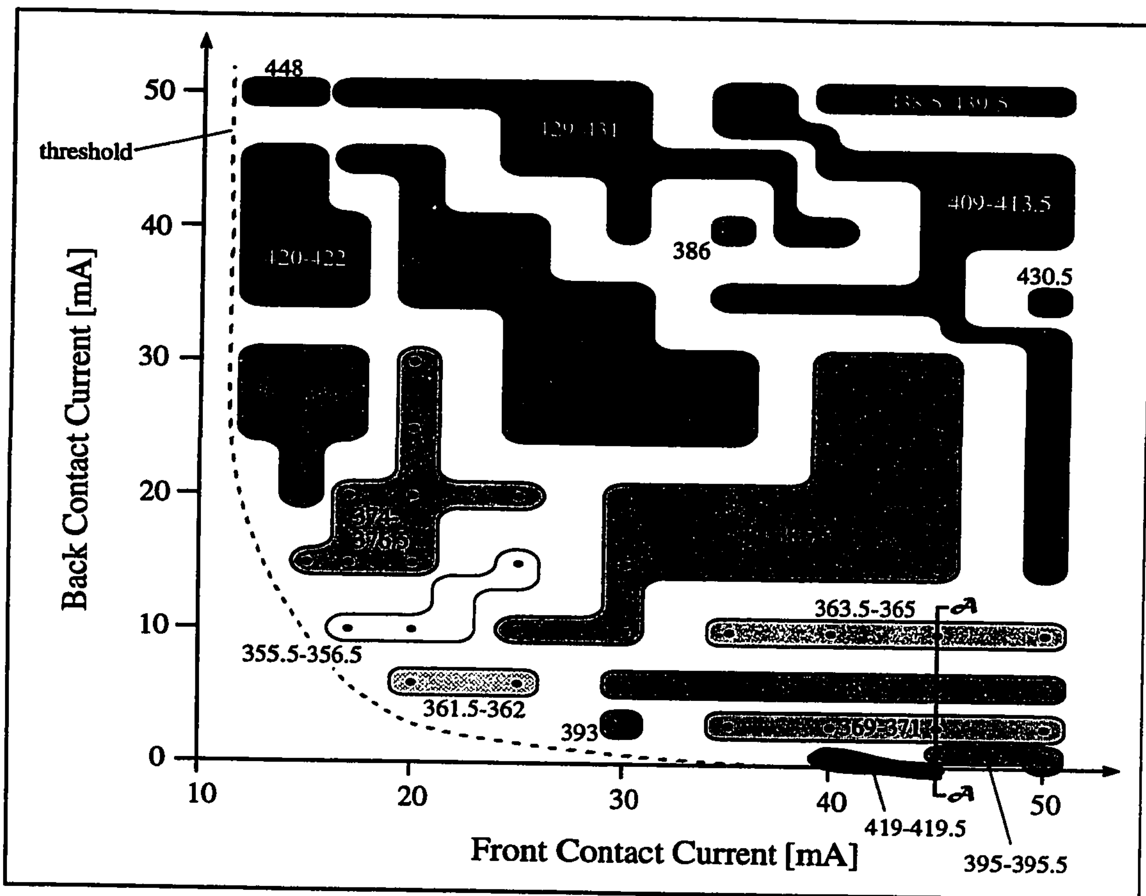

Figure 4.6.4: Peak Wavelength Map in the Bias Current Plane

Bias points at which spectra were taken are indicated by black dots, and threshold is shown (approximately) by the broken line. Contact lengths are L_F = 290 μm and L_B = 100 μm. Sets of spectra for which the peak wavelength varied continuously are grouped together, and denoted by regions of uniform shading. The range of wavelengths over which this continuous tuning was observed is indicated by the numbers on or beside each area: these numbers represent λ_{peak} - 13000 Å.

wavelengths of the dominant mode within each area. The mode hops between adjacent regions are not necessarily between adjacent modes.

However, a more holistic view of the map does reveal several trends that conform with our earlier discussions. Firstly, we note that the longest wavelength regions (those shaded more darkly) tend to occur in the strongly biased portions of the plane, especially

for large values of I_B. Since the back contact is the shorter of the two, this phenomenon is likely due to the heating caused by the high current densities.

Secondly, the biases at which the wavelength gradients are greatest are located near the axes, where non-uniform pumping effects are expected to be most pronounced (see Section 3.8). In particular the number of mode hops per mA of bias variation is greatest when I_B is varied between 0 and 10 mA, with I_F at a constant value between 40 and 50 mA (for example, along the line $\mathcal{A}$-$\mathcal{A}$ in Fig. 4.6.3). These biases are close to threshold and have a large ratio of $I_F : I_B$; in addition, because J_B is small the relative change in current density with bias current, $\frac{1}{J_B}\frac{dJ_B}{dI_{tot}}$, is large. As discussed in Section 3.8, these are exactly the sorts of changes in bias that we expect to result in the greatest tuning (primarily due to varying refractive index), because they represent highly non-uniform bias conditions.

Under close examination, Fig. 4.6.4 seems to imply that the maximum continuously tuneable wavelength range is ~4.5 Å (from 13381.0 Å to 13385.5 Å), and the total range of available wavelengths is 92.5 Å (from 13355.5 Å to 13448.0 Å). However, these numbers are likely conservative estimates, because the rather coarse distribution of bias points does not necessarily reveal the full detail of the spectral map. Although Fig. 4.6.4 is useful in summarizing the results, in order to learn the details of device behaviour under specific biases it is necessary to examine examples of the full spectra such as those shown in Fig. 4.6.3.

In principle the spectral map in Fig. 4.6.4 is most useful in combination with the power contours in Fig. 4.5.1, in situations where one needs to specify both the laser operating wavelength and output power. For a given device one would select the power contour that provides the desired output level, and then overlay this contour onto the spectral map. One could then read off the different operating wavelengths at this constant

power directly. The shapes of the specific power contour and its intersecting spectral regions will determine the range of wavelengths available at that power, and the amount of continuous tuning that can be achieved.

CHAPTER 4: REFERENCES

[1] Kant, Immanuel, Critique of Pure Reason, London, U.K.: The Guernsey Pres Co. Ltd., 1988, p. 166

[2] Adachi, S., "Material parameters of $In_{1-x}Ga_xAs_yP_{1-y}$ and related binaries", *J. Appl. Phys.* vol. 53, pp. 8775-8792, 1982

[3] Zory, Peter S. ed., Quantum Well Lasers, San Diego, CA: Academic Press, Inc., 1993, pp. 136-142

[4] Nishimura, T., Nakajima, Y., Kimura, T., Kokubo, Y., Isshiki, K., and Omura, E., "High-power and highly-reliable operatioin of all-MOCVD-grown 1.48 µm diode lasers", Laser Diode Techology and Applications IV, The International Society for Optical Engineering, Bellingham, Washington, 1994, pp. 142-151

[5] Gray, G.R. and Roy, R., "Bistability and mode hopping in a semiconductor laser", *J. Opt. Soc. Am. B*, vol. 8, pp. 632-638, 1991

CHAPTER 5: CONCLUSIONS

The Master said, "Yu, shall I tell you what it is to know. To say you know when you know, and to say you do not when you do not, that is knowledge.

K'ung Chung-ni, *Lun yü* II17[1]

5.1: INTRODUCTION

We have now completed our presentation of the results of our investigations regarding non-uniformly pumped semiconductor lasers. The theory, simulations, experimental techniques and measurements have been described: what remains is to put this information into perspective. In this chapter, we therefore attempt to distinguish the results of definite significance from those which may be more dubious, to recapitulate our particular contributions to the field, and to suggest ways in which future work might refine and expand our current knowledge of these devices.

5.2: SUMMARY OF ACHIEVEMENTS AND RESULTS

5.2.1: Theoretical Accomplishments

To begin with, perhaps the most significant objective we have achieved in the course of this work was the development of a mathematical model describing the physics of the operation of non-uniformly pumped semiconductor lasers. Our equations, which are based as accurately as possible on causal physical mechanisms, are capable of predicting many of the important phenomena associated with these devices. The model is quite general in terms of its input parameters: the basic framework could easily be adapted to simulate other types of semiconductor laser structures. We have attempted to address the issues with previous models discussed in Section 1.4.1, although we readily admit that

there are still aspects of our theory which could be further improved (some of these will be outlined in Section 5.3.1).

The simulations presented in Chapter 3 demonstrate that our model is able to reproduce both the more rudimentary device characteristics, such as the basic structure of uniformly pumped laser *L-I* and spectra, and also many of the more esoteric aspects of split-electrode laser behaviour. Superluminescence (with up to 4 mW of output power generated below threshold), optically bistable operation (with an extinction ratio of up to 98:1), and self-sustained pulsations (35 ps pulses at frequencies of 0.2 to >4 GHz) have all been simulated by the model.

The relatively detailed nature of the spectral simulations also allows us to investigate different tuning mechanisms in the lasers (gain peak shifts and refractive index changes) and estimate tuning ranges of split-contact lasers. Fabry-Perot cavity lasers are generally limited in their continuous tuning range by their free spectral range (typically a few Angstroms). However, our refractive index calculations indicate that if this limitation is relaxed (by reducing the cavity length or incorporating wavelength-sensitive Bragg reflectors) the range may be extended to greater than 30 Å while maintaining a constant output power.

In terms of non-uniform optical pumping, our simulations have shown transient response characteristics, injection locking of the output laser wavelength, optical switching in bistable configurations, and external, optical control of the self-pulsation phenomenon. Optical injection simulations show that the output wavelength of the laser can be locked over a range of seven cavity modes (~36 Å) with an input power of 1 mW. When the laser is electrically biased at an operating point inside the optical hysteresis loop, we have simulated both optical turn-ON (via the saturable absorber) and turn-OFF (via gain saturation) operations at the same pump wavelength.

One of the advantages of our laser model is the spatially and temporally detailed information it can generate. The spatial calculations have shown that even when a laser is uniformly biased, the carrier density can still vary with position in the active region. Although these variations are only on the order of 1%, they can still have a significant effect on the laser output above threshold.

Our model also allows the calculation of the detailed, large-signal time response of the laser. This is of particular importance in the self-pulsing regime, where the large fluctuations in the power (up to three orders of magnitude) at high frequencies would not be compatible with a small-signal analysis. The time-domain solutions that the model generates can simulate the structure of the self-sustaining pulse trains in considerable detail: this has allowed us to identify two distinct types of self-pulsations (continuously lasing above threshold modulation and repetitive Q-switching), as well as characterize their frequencies, pulse sizes, and operating bias regions.

5.2.2: Experimental Accomplishments

Experimentally, we have completed a survey of approximately eighty InGaAsP/InP ridge-waveguide split-electrode lasers with a range of different contact lengths. The measured light output vs. current characteristics of these devices are a reasonable match to the theoretical simulations, considering the approximations that were made during the modelling. Although the experimental *L-I* cannot be considered a quantitative match to the simulations, the trends observed when the biases and contact lengths are varied compare well. Similarly, although the measured spectral behaviour is more complicated than our model would suggest, we find a qualitative agreement.

By assembling the *L-I* measurements from a number of different lasers we have been able to construct threshold contour plots that illustrate the effects of geometry and bias

on the device output. These graphs indicate the dependence of threshold and the structure of the bistable region on the laser parameters. Hopefully, this information will be valuable for future device design because it can assist in the optimization of the laser geometry to achieve a specific desired effect.

5.3: Suggestions for Future Work

5.3.1: Possible Theoretical Improvements

There are several areas in which the theoretical treatment outlined in Chapter 2 could be improved. One of the most significant modifications would be to account for the phase of the optical energy in the laser cavity, which we currently model as a simple photon concentration. The changes necessary to incorporate this phase information into the optical equations (eqs. 2.5.10 and 2.5.11) should not be too overwhelming to achieve: the main problem lies in the added complexity of the numerical solutions. With the limited computer resources available when this project was begun it was not practical to carry out a full-scale analysis of the electric fields of the light in the laser, but this may not be as critical an issue in the near future. In the end, it will be necessary to extend the model in this manner to achieve an accurate model of the laser spectra, as well as to simulate such phenomena as mode locking.

Another improvement that should not be too difficult to implement would be to account for quantum effects in the laser. Although the majority of modern devices include quantum structures in their active regions, the present model assumes a bulk description of the active region. This was done in part to minimize the complexity of the problem, but also because at the beginning of the project the exact structure of our experimental devices had not yet been determined. Unfortunately, this discrepancy in the modelling of the band

structure of the active region material reduces the usefulness of the spectral simulations in Section 3.4, if they are to be compared with our measured data. In any event, to model quantum effects it should only be necessary to modify the form of the density of states used (in eqs. 2.3.5 and 2.3.10). The determination of the equilibrium absorption coefficient (see Section 2.3.3) may be somewhat more difficult than it was for the bulk case, however.

A third modification to the theory presented in this work that would have considerable value would be to include the effects of Bragg reflectors in the laser. In modern applications where wavelength tolerances are important, and particularly when the device is to be used as a tunable source, both DFB and DBR lasers are often used. One could, perhaps, simulate a DBR by converting the facet reflectivities (the values of R_1 and R_2 in eqs. 2.5.10 and 2.5.11) into functions of wavelength. However, this is a rather approximate approach, and does not inherently address the question of the exact functional form of $R(\lambda)$ that must be used. A more accurate method would be to explicitly simulate the multiple reflections that are distributed over the laser cavity. This would, however, increase the number of calculations that need to be performed for each simulations by a considerable factor.

5.3.2: Possible Experimental Improvements

There are several ways in which the experimental study we have presented here could be expanded. One of the principle shortcomings of our work was our inability to make high-speed measurements of our split-contact lasers. Both the self-pulsing phenomena and external modulation characteristics require the detection of signals at frequencies into the gigahertz range, but this was not possible with the equipment available at the time this project was carried out. Fortunately, there has been a considerable amount

of effort expended in this area by other groups (see Sections 1.3 and 3.5 for more detailed references), so that data is available from outside sources for comparison with our simulations.

Optical injection experiments would also be useful for comparisons with our theoretical predictions of device performance. The main problem in our case was caused by the laser mounting system: it was difficult to achieve reproducible optical coupling to both of the laser facets simultaneously. If this is achieved, it should be possible, with the use of the appropriate focusing system and optical isolators, to use two lasers in a pump-probe configuration. This would allow the specific details of the optical pumping simulations in Section 3.7 to be verified.

As Table 4.2.2 indicates, we have had a considerable number of device configurations to investigate in this work. However, it would also be worthwhile to examine other variations in order to broaden the data base that we have constructed, and to establish whether the trends that we have observed can be extended to other laser structures. For instance, additional structures with constant total length and varying position of the break in the top contact could be examined to further explore the threshold current density phenomenon we observed in Section 4.5.3. Investigations of other laser systems, with variations in parameters such as the number of quantum wells, lasing wavelength (possibly working at 1.55 μm), or using buried heterostructure devices, would allow us to determine whether the results presented here can truly be generalized to more arbitrary device structures.

Both our theoretical and experimental investigations have indicated that the continuous tuning range of Fabry-Perot semiconductor lasers is limited by the free spectral range of the cavity. Because there is considerable current interest in producing lasers with a large tuning range at constant output power, it would be profitable to continue the

research that began with this project by introducing DFB or DBR structures into future device iterations. Without some mechanism for increasing the spacing between the competing modes in the cavity, it will not be possible to realize the full range of spectral control that some applications require.

CHAPTER 5: REFERENCES

[1] Confucius, The Analects, Toronto, Ontario: Penguin Books Canada Ltd, 1971, p. 65

APPENDIX A: APPROXIMATION FOR THE FERMI FUNCTION

For convenience, we now re-write eq. (2.4.2), the relationship between the carrier concentration and the Fermi level, as

$$\frac{n}{N_c} = \frac{2}{\sqrt{\pi}} \int_0^\infty \frac{\sqrt{E}dE}{1+e^{(E-\Delta E_{Fc})}} \tag{A.1}$$

where $\Delta E_{Fc} = \frac{E_{Fc} - E_c}{kT}$ is the energy difference between the Fermi level and the band edge. Now, eq. (A.1) cannot be re-arranged into an analytical expression for the Fermi level as a function of carrier concentration. We can, however, solve it numerically at discrete values of ΔE_{Fc}, allowing us to define $\Delta E_{Fc}(n)$ by reference to a look-up table. The solid curve in Fig. A.1 illustrates the function $\Delta E_{Fc}(n)$ calculated in this manner.

Because there are approximately 500 data points in the look-up table defining the solid curve in Fig. A.1, an interpolating routine to calculate a particular value of $\Delta E_{Fc}(n)$ can be quite time-consuming. To expedite the numerical calculations that must be performed, we approximate the function by fitting it to a series of analytical functions over the range of carrier concentrations in question. For the non-degenerate case the simple Boltzman approximation has been used, and a least-squares technique was used to determine a polynomial fit to the data for the rest of the range. The resulting expression for $\Delta E_{Fc}(n)$ is

$$\Delta E_{Fc} = \ln\left(\frac{n}{N_c}\right) \quad , \quad n/N_c \leq 0\ 04858$$

$$= \sum_{j=0}^{5} a_j \left(\frac{n}{N_c}\right)^j \quad , \quad 0.048586 < n/N_c \leq 0.76146 \qquad \text{(A.2)}$$

$$= \sum_{j=0}^{5} b_j \left(\frac{n}{N_c}\right)^j \quad , \quad 0.76146 < n/N_c \leq 8.8368$$

$$= c_0 \left(\frac{n}{N_c}\right)^{c_1} \quad , \quad 8.8368 < n/N_c$$

The values of the constants a_j, b_j, and c_j are given in Table A.1, below.

j	a_j	b_j	c_j
0	-3.9323	-1.5095	1.1913
1	23.214	2.3663	0.66829
2	-81.702	-0.63933	
3	159.03	0.11059	
4	-147.7	-0.0093852	
5	51.055	0.00030491	

Table A.1: Coefficients Used In Equation (A.2) to Fit $\Delta E_{Fc}(n)$

The function defined by eq. (A.2) has also been plotted in Fig. A.1 (the broken curve). As we can see, the match between the numerically calculated curve and the analytical fit is quite good. In fact, the correlation coefficient, R, is greater than 0.9998 over the entire range shown. Because eq. (A.2) can be solve considerably more quickly than the method of interpolating values from points in a large look-up table, this fitted function has been used for all calculations of $\Delta E_{Fc}(n)$ in this thesis.

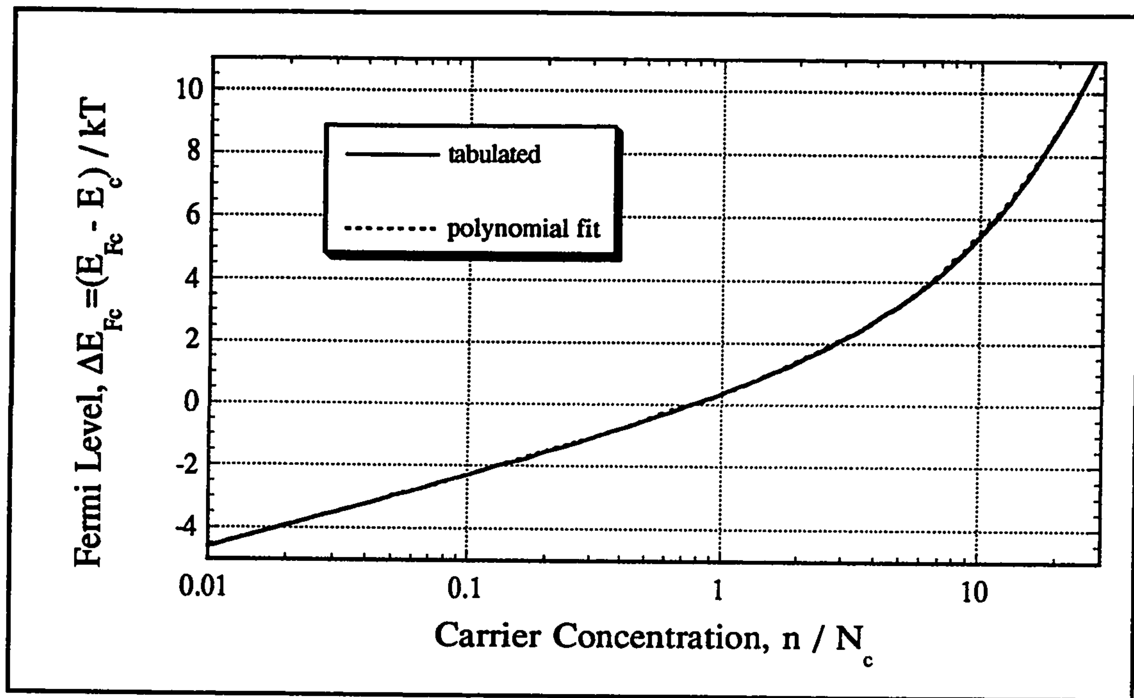

Figure A.1: Fermi Level vs. Carrier Concentration

This figure shows position of the Fermi level as a function of the carrier concentration. The solid curve was calculated by solving eq. (A.1) numerically, generating a look-up table to define the function. The broken curve represents the polynomial fit to this data, described by eq. (A.2).

APPENDIX B: CALCULATING THE REFRACTIVE INDEX

B.1: THE KRAMER-KRONIG RELATION

The model developed in Chapter 2 allows us to calculate the material gain in the active region of a laser as a function of the carrier concentration and optical wavelength. This gain is related to the imaginary part of the material's index of refraction, n_i, by the expression[1]

$$n_i(\omega) = \frac{cG_m}{2\omega} \tag{B.1}$$

where G_m is the material gain[a] in the mth cavity mode, and c and ω are the speed and angular frequency of the light in that mode. The complex index of refraction is defined as $n_c = n_r + \mathrm{i}n_i$, where n_r is the real part of the index of refraction, and $\mathrm{i} = \sqrt{-1}$.

Now, since $n_i(\omega)$ is a "well behaved" function (it vanishes as $\omega \rightarrow \infty$,[b] and is a physically measurable quantity), the real and complex parts of $n_c(\omega)$ must obey the Kramer-Kronig relations. We can therefore use the expression[2]

$$n_r(\omega_0) = -\frac{2}{\pi}\int_0^\infty \frac{\omega\, n_i(\omega)}{\omega^2 - \omega_0^2}\, d\omega \tag{B.2}$$

---

[a] Equation (2.4.1), derived in Chapter 2, is used to model G_m.

[b] Actually, $n_i(\omega) \rightarrow 1$ as $\omega \rightarrow \infty$, but this term can easily be subtracted off in the numerical calculation. In any event, it will not affect the relative changes in the real refractive index, which are the values in which we are interested.

to calculate n_r from the values of G_m generated in Chapter 2.

B.2: THE NUMERICAL SOLUTION

In practice, eq. (B.2) must be solved numerically, both because of the nature of the integral and because of the fact that our function G_m is defined by a discrete array of previously calculated data points. Even though the total integral in eq. (B.2) is finite, because of the $\omega^2 - \omega_0^2$ term in the denominator numerical techniques may prove difficult for an arbitrary function $n_i(\omega)$. However, in any physically realistic situation it will be possible to approximate $n_i(\omega)$ as a linear function within some small range of frequencies near ω_0, so that

$$n_i(\omega) \approx n_i(\omega_0) + \left[\frac{dn_i}{d\omega}\right]_{\omega_0} (\omega - \omega_0), \qquad |\omega - \omega_0| \le \Delta\omega_0 \tag{B.3}$$

This approximation can be made as accurate as desired by reducing the magnitude of $\Delta\omega_0$.

If we apply the approximation of eq. (B.3) to (B.2), the integral can be broken up into two sections to be solved numerically (in the regions where eq. (B.3) is not valid) and one term that can be solve analytically:

$$n_r(\omega_0) = -\frac{2}{\pi}\left\{\int_0^{\omega_0-\Delta\omega_0} \frac{\omega\, n_i(\omega)}{\omega^2 - \omega_0^2} d\omega + P + \int_{\omega_0+\Delta\omega_0}^{\infty} \frac{\omega\, n_i(\omega)}{\omega^2 - \omega_0^2} d\omega\right\} \tag{B.4}$$

where $P = \int_{\omega_0-\Delta\omega_0}^{\omega_0+\Delta\omega_0} \frac{\omega\, n_i(\omega)}{\omega^2 - \omega_0^2} d\omega$.

Using the approximation in eq. (B.3), this integration for P can be simplified to

$$P = 2\Delta\omega_0 \left[\frac{dn_i}{d\omega}\right]_{\omega_0} - \left\{\frac{n_i(\omega_0)}{2} + \omega_0 \left[\frac{dn_i}{d\omega}\right]_{\omega_0} \ln\left(\frac{2\omega_0 + \Delta\omega_0}{2\omega_0 - \Delta\omega_0}\right)\right\} \tag{B.5}$$

For the calculations of n_r in this work we make use of eq. (B.4): by choosing $\Delta\omega_0$ judiciously the first and third terms can be accurately evaluated numerically, and our approximation in eq. (B.3) allows us to solve for the second term, P, analytically. Thus, given the gain function G_m calculated Chapter 2 we can determine the corresponding real part of the refractive index.

It should be noted that this calculation accounts only for contributions to n_r caused by the variable carrier density in conduction and valence bands. Since effects such as non-parabolic, non-isotropic bands and optically active defects are not modelled we cannot expect results that are accurate in an absolute sense. However, for our purposes we are primarily interested in the *change* in the real part of the refractive index (in order to calculate shifts in the laser cavity modes). Since the bulk of these injected carriers are expected to reside in the conduction and valence bands (indeed, the entire validity of our model is based on this assumption), the relative changes in the refractive index that occur when the laser bias is varied should be reasonably well described by eq. (B.4).

APPENDIX B: REFERENCES

[1] Hecht, Eugene, Optics, Second Edition, Don Mills, Ont.: Addison-Wesley Publishing Company Inc., 1987, page 110

[2] Verdeyen, Joseph Thomas, Laser Electronics, Second Edition, Englewood Cliffs, New Jersey: Prentice Hall, 1989, page 607, eq. (II.10)

APPENDIX C: SIMULATED LASER STRUCTURES

In order to give a comprehensive list of the simulated laser structures used in Chapter 3, the parameters that are not common to all the simulations are listed in the table below.

Structure	L_1 [µm]	L_2 [µm]	R_1 [%]	R_2 [%]
B1	850	150	28.3	28.3
M1	350	150	28.3	28.3
M2	433	67	28.3	28.3
M3	350	150	90	28.3
M4	350	150	28.3	90
S1	250	50	28.3	28.3

APPENDIX D: GLOSSARY

Symbol	Value	Description
A	10^{8} s^{-1}	unimolecular recombination coefficient[a]
B_r		strength of the coupling between transition states
C	$1.6\text{x}10^{-29}$ cm^6/s	Auger recombination coefficient[a]
c	$3\text{x}10^{10}$ cm/s	speed of light (in vacuum)
D	1 μm	active region depth (simulations)
$E_{Fc/v}$		conduction/valence band Fermi energy
E_c		lowest conduction band energy
E_g	0.9556 eV	active region energy band-gap
$E_{u,l}$		upper/lower energies of the states in a radiative transition
E_v		highest valence band energy
$f_{c,v}$		conduction/valence band occupancy functions
f_o		equilibrium occupancy function
G_m		gain/absorption of the mth cavity mode
h	$4.141\text{x}10^{-15}$ eV.s	Plank's constant
$\hbar$	$1.318\text{x}10^{-15}$ eV.s	$h/2\pi$
$I_{1,2}$		current into contacts #1 and 2
$I_{F,B}$		current into front and back contacts
$I^{\pm}_{sat}$		bias current at absorber saturation (± refers to increasing/decreasing current)

[a] Paradisi, A. and Montrosset, I., "Numerical modeling of bistable laser diodes with saturable absorbers", *IEEE J. Quantum Electron.*, vol. 27, pp. 817-823, 1991

Symbol	Value	Description
$I_{th}^{\pm}$		bias current at threshold (± refers to increasing/ decreasing current)
I_{tot}		total bias current (sum into all contacts)
J		current density
$J_{1,2}$		current densities into contacts #1 and 2
$J_{F,B}$		current densities into the front and back contacts
K	61450 $cm^{-1}eV^{-0.5}$	constant of proportionality for absorption coefficient
k	8.62×10^{-5} eV/K	Boltzman's constant
$L_{1,2}$		lengths of contacts #1 and 2
$L_{F,B}$		lengths of the front and back contacts
L_T		total laser length
M	14	total number of cavity modes considered in the model
m		cavity mode #
$m_{e,h}$	$0.051m_o$, $0.511m_o$	electron/hole effective masses
m_o	9.1×10^{-30} kg	free electron mass
$N_{c,v}$	2.853×10^{17} cm^{-3}, 9.063×19^{18} cm^{-3}	conduction/valence band effective density of states
n		carrier concentration
$\bar{n}$		carrier concentration, averaged over the length of the active region
n_c		complex refractive index
$n_{i,r}$	3.271, 3.085[a]	real/imaginary part of the refractive index
n_o	1.343×10^{10} cm^{-3}	intrinsic carrier concentration

[a] These values represent the real part of the index of refraction in the active region and cladding, respectively, for an unbiased sample.

Symbol	Value	Description
$P_{1,2}$		optical power output, facet #1 and 2
Q_m		# of spontaneous emission events per unit length per second coupled into the mth cavity mode
q	1.602×10^{-19} C	electron charge
R_o		equilibrium radiative recombination rate
$R_{1,2,i}$	0.283, 0.283, 0.0283	reflectivities at facet #1, facet #2, and the contact interface, respectively
R_r		carrier recombination rate, due to spontaneous emission and all non-radiative mechanisms
R_{sp}		carrier recombination rate, due to spontaneous emission
$S_m^{\pm}$		photon density in the mth cavity mode, moving in the $\pm x$ direction
$S_{me}^{\pm}$		external photon density coupled into the mth cavity mode through facets #1 ($^{+}$) and #2 ($^{-}$)
T	300K	absolute temperature
T_i	0.9717	transmittivity at the contact interface
t		time
v_m	9.17×10^{9} cm/s	speed of photons in the mth cavity mode
W	2 μm	active region width (simulations)
x		position in active region
α_o		equilibrium material absorption per unit length
β_m	0.02836	fraction of the spontaneous emission coupled into the mth cavity mode
$\Delta E_{c/v}$		normallized energy difference between conduction/ valence band edge and Fermi level
$\Delta\lambda_m$		spectral width of the mth cavity mode
$\delta\lambda_m$		wavelength shift of the mth cavity mode

Symbol	Value	Description
Δt	~5.5×10^{-13} s	temporal increment for numerical solution (value is typical)
Δx	~50 µm	spatial increment for numerical solution (value is typical)
Γ_m	0.5	optical confinement factor of the mth cavity mode
λ		wavelength
λ_m		wavelength at the centre of the mth cavity mode
λ_{peak}		wavelength of the maximum in the output spectrum
μ	2000 $cm^2V^{-1}s^{-1}$	carrier mobility
ν		frequency
ω		angular frequency, $\nu/2\pi$
ρ		power density of the blackbody spectrum
ρ_{red}		reduced density of states
θ_c	19.4°	critical angle for total internal reflection at the active region/cladding interface

Note: values are only given in cases where they are constant throughout this work. In other cases, specific values are included in the body of the text.

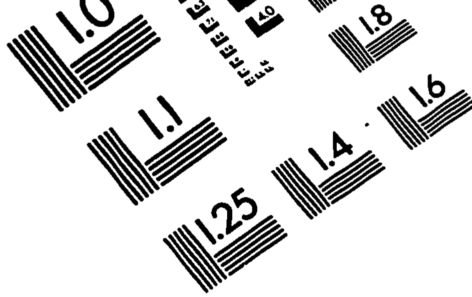

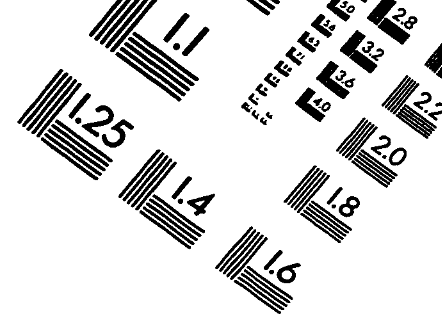

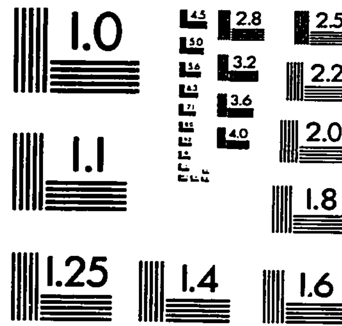

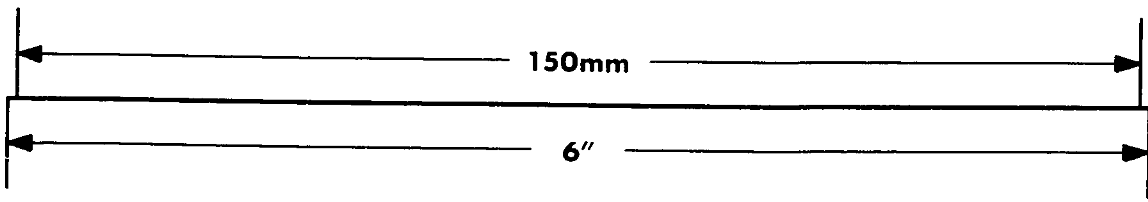

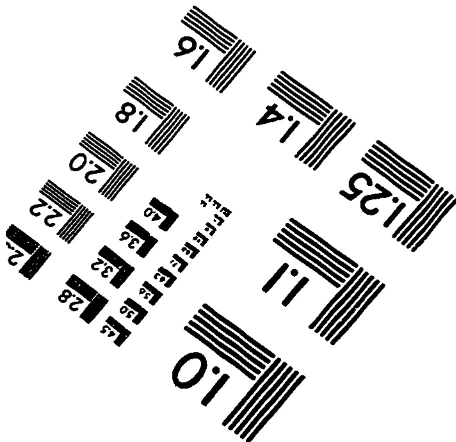

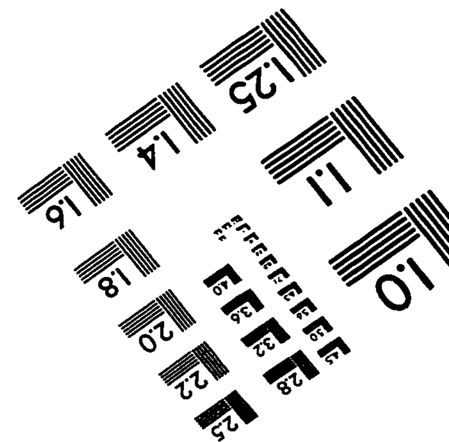

APPLIED IMAGE . Inc
1653 East Main Street
Rochester, NY 14609 USA
Phone: 716/482-0300
Fax: 716/288-5989

© 1993, Applied Image, Inc., All Rights Reserved